

## **Thermal stability and wear behaviour of AISI S2 tool steel processed by Laser Powder Bed Fusion**

**Auteur :** Segatto, Alessandra

**Promoteur(s) :** Mertens, Anne

**Faculté :** Faculté des Sciences appliquées

**Diplôme :** Cours supplémentaires destinés aux étudiants d'échange (Erasmus, ...)

**Année académique :** 2023-2024

**URI/URL :** <http://hdl.handle.net/2268.2/20824>

---

### *Avertissement à l'attention des usagers :*

*Tous les documents placés en accès ouvert sur le site le site MatheO sont protégés par le droit d'auteur. Conformément aux principes énoncés par la "Budapest Open Access Initiative"(BOAI, 2002), l'utilisateur du site peut lire, télécharger, copier, transmettre, imprimer, chercher ou faire un lien vers le texte intégral de ces documents, les disséquer pour les indexer, s'en servir de données pour un logiciel, ou s'en servir à toute autre fin légale (ou prévue par la réglementation relative au droit d'auteur). Toute utilisation du document à des fins commerciales est strictement interdite.*

*Par ailleurs, l'utilisateur s'engage à respecter les droits moraux de l'auteur, principalement le droit à l'intégrité de l'oeuvre et le droit de paternité et ce dans toute utilisation que l'utilisateur entreprend. Ainsi, à titre d'exemple, lorsqu'il reproduira un document par extrait ou dans son intégralité, l'utilisateur citera de manière complète les sources telles que mentionnées ci-dessus. Toute utilisation non explicitement autorisée ci-avant (telle que par exemple, la modification du document ou son résumé) nécessite l'autorisation préalable et expresse des auteurs ou de leurs ayants droit.*

---



UNIVERSITÀ  
DEGLI STUDI  
DI PADOVA

**Université de Liège – Università degli Studi di Padova**

Faculté des Sciences Appliquées – Dipartimento di Ingegneria Industriale  
DII

***Thermal stability and wear behaviour of AISI S2 tool steel  
processed by Laser Powder Bed Fusion***

Master's Thesis in order to obtain the degree  
of Master of Science in Materials Engineering by

Segatto Alessandra

*Supervisor: Prof. Anne Mertens (Université de Liège)*

*Co-supervisor: Prof. Irene Calliari (Università di Padova)*

Academic year: 2023/2024



# ABSTRACT

This study investigates the thermal stability and wear behaviour of AISI S2 tool steel processed by Laser Powder Bed Fusion. The processability of this material was previously examined in a separate study conducted by the same team. Isothermal treatments up to 10 hours were performed on as-built samples at three different temperatures (200 °C, 300 °C, and 400 °C), in order to investigate the thermal stability. The alloy is thermally stable at 200 °C and 300 °C, whereas its microstructure and properties change at 400 °C. Pin-on-disc campaigns were conducted at room and high temperatures. The wear sequence of the material at room temperature was elucidated, following the approach of interrupted wear tests. High-temperature wear tests were conducted at the same temperatures as those of the isothermal treatments. The wear behaviour at 200°C and 300°C were found to be similar to that at room temperature, while the wear behaviour at 400 °C was markedly different, including the formation of a thick oxide layer and of a tribolayer that protect the surface from further wear. The results showed an increased wear rate at high temperatures compared to that at room temperature. These analyses were conducted using optical and scanning electron microscopy, DSC, pin-on-disc, profilometer, and macro and nano-indentation techniques.





# ACKNOWLEDGEMENTS

First, I would like to extend my deepest gratitude to Prof. Anne Mertens and Dr. Jérôme Tchoufang Tchuindjang for their supervision and guidance throughout my research and the writing of this thesis. I am also sincerely thankful to Prof. Irene Calliari for providing me with the opportunity to pursue my studies at this Erasmus destination, and to the University of Liège for their warm welcome from the very first day.

I am grateful to the entire MMS team, particularly to PhD Enrico Saggionetto, for his help, patience, and constant guidance over these months. He has made this journey as enjoyable as possible and has continuously provided me with valuable advice. I would also like to thank all the friends I met in Liège, for making me feel at home and for all the unforgettable moments we shared. Additionally, I extend my heartfelt thanks to my friends in Italy, for never letting me feel alone and for always being ready to listen to my lengthy worries.

None of this would have been possible without the continuous support of my family—my mother Riccarda, my father Angelo, and my sister Agnese. I am deeply grateful to them for all the experiences they have enabled me to have and for the love they have given me. Last but not least, I thank Fede, who has supported me for over six years and stood by my side throughout my entire university journey.



# Table of contents

1.	Introduction.....	1
2.	State of the art .....	3
2.1	Additive Manufacturing (AM).....	3
2.1.1	LPBF process mechanism.....	4
2.1.2	Tool steel for LPBF .....	6
2.2	Thermal stability of tool steel .....	8
2.3	Tribology.....	9
2.3.1	Types of wear .....	9
2.3.2	Wear testing methods .....	16
2.3.3	Wear behaviour of tool steel by LPBF .....	18
3.	Materials and experimental methods .....	21
3.1	Samples fabrication by LPBF .....	21
3.1.1	Powders.....	21
3.1.2	Printing parameters .....	21
3.2	DSC.....	22
3.3	Microstructure characterization .....	23
3.3.1	Sample preparation .....	23
3.3.2	Optical microscope (OM) and Stream Analysis Software .....	24
3.3.3	Scanning electron microscope (SEM).....	24
3.4	Wear tests .....	25
3.4.1	Pin-on-disc tribometer.....	25
3.4.2	Profilometer .....	28
3.5	Hardness.....	29
3.5.1	Macro-hardness.....	29
3.5.2	Nano-hardness.....	29
4.	Results.....	31
4.0	As-built microstructure and DTA thermal treatments .....	31
4.1	Microstructure after thermal treatment .....	35
4.1.1	DSC analyses .....	35
4.1.2	Microscope observations.....	36
4.1.3	Macro-hardness .....	37
4.2	Wear tests .....	38

4.2.1	Room Temperature.....	38
4.2.2	High Temperature.....	47
5.	Discussion .....	57
5.1	Thermal stability .....	57
5.2	Elucidation of wear sequence at room temperature .....	59
5.3	Effect of Temperature on wear behaviour .....	63
6.	Conclusion .....	67
7.	Perspectives.....	69
8.	References .....	71
9.	Annex .....	83

# List of Figures

<i>Figure 1: Schematic illustration of the LPBF process[18].....</i>	<i>4</i>
<i>Figure 2: a) sketch of LPBF process showing melt pools and re-melting of the previous layer; b) overlap of the melt pools horizontally and vertically.....</i>	<i>5</i>
<i>Figure 3: a) Micrograph of the melt pool; b) example of numerical simulation of dendritic solidification in LPBF.[26] .....</i>	<i>6</i>
<i>Figure 4: Schematic illustration of epitaxial growth. [4] .....</i>	<i>7</i>
<i>Figure 5: Microstructure of a LPBF steel characterized by tempered and untempered martensite and bainite.[24] .....</i>	<i>8</i>
<i>Figure 6: SEM micrographs of martensitic LPBF steel showing cellular structure at a) 50 <math>\mu\text{m}</math> and b) 10 <math>\mu\text{m}</math>.[30].....</i>	<i>8</i>
<i>Figure 7: Mechanism of abrasive wear; a) micro- cutting; b) fracture; c) fatigue; d) grain pull-out.[56] .....</i>	<i>10</i>
<i>Figure 8: a) two-bodies abrasive mode; b) three-bodies abrasive mode.[56] .....</i>	<i>10</i>
<i>Figure 9: Schematic representation of adhesive wear.[57] .....</i>	<i>11</i>
<i>Figure 10: Schematic illustration of adhesive wear steps.[57] .....</i>	<i>11</i>
<i>Figure 11: Schematic possible illustration of corrosive wear.[58].....</i>	<i>12</i>
<i>Figure 12: Schematic representation of oxidative wear steps.[60] .....</i>	<i>13</i>
<i>Figure 13: Schematic representation of an example of a mechanism of erosive wear: a) abrasion at low impact angles; b) crack formation due to high-angle impact at low speed; c) plastic deformation or brittle fracture due to high-angle impact at considerable speed; d) melting of the surface due to high-speed impacts; e) effect of a large particle in an erosive impact; f) effect of a tiny particle in an erosive impact (atomic-scale impact), leading to atomic erosion. ....</i>	<i>14</i>
<i>Figure 14: a) schematic illustration of the release of wear particles and plastic strain deformation of the subsurface; b) schematic illustration of crack formation in fatigue wear mechanism.[61] .....</i>	<i>15</i>
<i>Figure 15: Mechanism of bubble collapsing in cavitation wear.[56].....</i>	<i>15</i>
<i>Figure 16: Pin-on-disc machine.[64] .....</i>	<i>16</i>
<i>Figure 17: Schematic illustration of four ball tester.[65].....</i>	<i>17</i>
<i>Figure 18: Reciprocating sliding friction scheme.[66] .....</i>	<i>17</i>
<i>Figure 19: Fretting wear tester scheme.[67] .....</i>	<i>18</i>
<i>Figure 20: wear track of the same steel a) LPBF printed and b) conventional steel [69] .....</i>	<i>19</i>
<i>Figure 21: wear track of tool steel; a) grooves and b) plastic deformation of grooves. ....</i>	<i>19</i>
<i>Figure 22: wear track with some deformed zone and smooth sliding.[70] .....</i>	<i>20</i>
<i>Figure 23: SEM micrographs of the S2 powders. ....</i>	<i>21</i>
<i>Figure 24: AconityMINI machine. [72] .....</i>	<i>22</i>
<i>Figure 25: Printed samples. The black arrows indicate the samples for the wear test, and the orange arrows indicate the samples for the heat treatment. ....</i>	<i>22</i>
<i>Figure 26: DSC Jupiter -404C from NETZSCH [73]. ....</i>	<i>23</i>

Figure 27: Schematic illustration of the thermal treatments. Isothermal segments are 5 or 10 hours.	23
Figure 28: Olympus BX60 [74].	24
Figure 29: Tescan Clara Ultra-High Resolution SEM machine [75].	25
Figure 30: Sample cut for the wear test. The white line is the cutting, for each printed sample four faces will result.	25
Figure 31: Schematic illustration of wear sample designation from one cut printed sample.	25
Figure 32: High Temperature Tribometer [77].	27
Figure 33: Schematic illustration of a) cutting of a piece to see the cross-section under the track; b) piece after cutting before bakelite incorporation and polishing; in green is highlighted the direction where the cross-section will be seen (xz plane).	28
Figure 34: Alicona InfiniteFocusG5 [78].	28
Figure 35: EMCO MIC 010 hardness machine [79].	29
Figure 36: TI 950 Tribometer nanoindenter [80].	30
Figure 37: Sketch of the process of melt pool solidification. (a) Melt pool with molten powders after the laser travels by; (b) primary nucleated grains following the orientation of the building direction within the melt pool border (c) epitaxial growth with side-branching phenomenon of the nucleated grains (d) addition of a new powder layer (e) the process new step, which affects the microstructure of the layers below [5].	32
Figure 38: SEM micrograph. Segregation, laths of martensite, and precipitations are highlighted.	33
Figure 39: (a) Heat-affected zones and (b, c) their nano-hardness. Higher magnification of the (d) austenization zone, (e, h) bainite, and (f, i) tempered martensite. (g) Austenization zone revealed by scanning the surface with the scan mode of the nano-indenter.	34
Figure 40: DTA curves of S2; a) shows the complete curve with the red rectangle that highlights the zone of interest; b) is a zoom of the curve a) with the selected temperatures highlighted by red circles and arrows.	35
Figure 41: DSC curves for isothermal maintenance with Heat flow plotted on time.	36
Figure 42: OM micrograph samples post-etching. a) sample treated at 200°C for 10 hours; b) sample treated at 300°C for 10 hours; c) sample treated at 400°C for 10 hours.	36
Figure 43: SEM micrographs of 10-hour isothermal treated samples at a magnification of 20 $\mu\text{m}$ and 2 $\mu\text{m}$ in scale from left to right. a) and b) samples treated at 200°C; c) and d) sample treated at 300°C; e) and f) sample treated at 400°C.	37
Figure 44: Hardness vs. Temperature and time graphs. The hardness is in HV5.	38
Figure 45: Graphs of Coefficient of Friction test at Room Temperature. a) entire CoF of RT1500; b) zoom of the CoF of RT1500 Test, red lines indicate where was chosen to interrupt subsequent tests; c) graph of CoF of RT18 Test; d) graph of CoF RT65 Test; e) a zoom of the comparison of the CoF of the three tests.	39
Figure 46: Wear rate (blue) and worn volume (orange) comparison for the three RT tests.	40
Figure 47: Profilometer photos of the wear tracks. On the left, the height scale at which the photos were taken is reported. a) wear track RT18 test; b) wear track RT65; c) wear track RT1500 test.	40
Figure 48: Alumina counter-body photo and size of worn. The range was maintained constant for every examination.	41

Figure 49: OM (a, c) and SEM (b, d) micrographs of the RT18 test. a) and b) are taken in the same position on the track, as well as c) and d). The red arrows indicate the sliding direction during the wear test; e) and f) show an example of the crack along the wear track; g) and h) show plastic flow and fracture surface where delamination occurs.....	42
Figure 50: Green arrows indicate the sliding direction during the test. a) and b) OM micrographs of the RT65 test. Compacted debris is highlighted; c) debris accumulation along the rectification lines and outside the track; d) detachment zone and plastic deformation of the surface of the track; e) and f) show debris compacted by the counter-body passage.....	43
Figure 51: Micrographs of wear tracks of RT1500 test; a) and b) OM micrographs of Track RT1500, c) SEM micrograph, and d) a zoom from the yellow rectangle of c) micrograph. The red arrows indicate the sliding direction of the wear tests.....	44
Figure 52: Debris overview of a) RT18; b) RT65 and c) RT1500. ....	44
Figure 53: a) big platelets outside the track in the RT18 test; b) compacted debris along the track, RT65; c) crushed debris outside the track, RT1500; d) different sizes of the debris with respect to the distance from the track.....	45
Figure 54: Crushed debris of the RT1500 wear test. The micrograph is taken in the same position as Figure 52.c one. ....	46
Figure 55: a) and b) subsurface micrographs of the RT1500 test. The green arrows indicate the sliding direction of the wear test. Mechanically mixed layer (MML) and plastic deformed layer (PDL) are highlighted; c) nano hardness grid of subsurface sample (RT1500). The blue part is the resin (Bakelite). The reported scale is in GPa. ....	47
Figure 56: a) wear test at 200°C, showed yellow; b) wear test at 300°C, showed blue; c) wear test at 400°C showed grey; d) tempering steel chart is reported with a highlight on the three temperatures of the wear tests that are consistent with the results[81].....	48
Figure 57: Comparison between Coefficient of Friction of RT and HT tests. ....	48
Figure 58: Profilometer photos taken at the same range, reported on the left. a) HT200 test; b) HT300 test and c) HT400 test. ....	49
Figure 59: a) Worn volume and b) wear rate comparison of the four long tests.....	49
Figure 60: Profilometer photo and data of sizes of HT tests with the range on the left, the same as RT measurement. a) HT200 test; b) HT300 test and c) HT400 test. ....	50
Figure 61: Micrographs wear track HT200 test. a) and b) OM micrographs show the pale yellow surface and the debris along the track; c) SEM photo taken in the same place of a) shows the surface; d) SEM zoom on the detachment along the track.....	51
Figure 62: Micrographs of HT300 test with red arrows indicating sliding direction. a) OM micrograph shows the pink-blue-purple colour of the sample; b) OM micrograph shows platelets detachment; c) SEM micrograph shows the clean track; d) SEM micrograph of platelets detachment; e) SEM micrograph shows the accumulation of the debris at the start of groove.....	52
Figure 63: Micrographs HT400 test, red arrows indicate the sliding direction. a) and b) show a different part of the track where the tribolayer is present. c) SEM micrograph of tribolayer and d) zoom of c) where detachment from tribolayer is highlighted.....	53
Figure 64: OM micrographs of the subsurface of wear tests. a) 200°C; b) 300°C; c) 400°C. ....	54
Figure 65: SEM micrograph of the subsurface of the wear track. Green arrows indicate the sliding direction of the wear tests. a) and b) HT200 test; c) and d) HT300 test; e) and f) HT400 test. ....	55
Figure 66: Macro-hardness comparison between HT wear tests and 10-hour thermal treatments. .	56



<i>Figure 67: Nano-hardness grid from nano-indentation data. The blue part is bakelite resin. a) 200HT test; b) 300HT test; c) 400HT test.....</i>	<i>56</i>
<i>Figure 68: Sketch of the platelet formation in the run-in period.....</i>	<i>60</i>
<i>Figure 69: Sketch of MML formation. Platelets were detached, ground, and then formed the MML over the PDL. ....</i>	<i>62</i>
<i>Figure 70: Sketch of the microstructure evolution during the RT test. ....</i>	<i>63</i>

# List of Tables

<i>Table 1: Chemical composition analysis of S2 powder.</i>	21
<i>Table 2: Parameters of printing.</i>	22
<i>Table 3: Isothermal tests performed. Three tests were performed for 5 hours, the other three for 10 hours.</i>	23
<i>Table 4: All printed samples after cutting. The green highlights are the ones chosen for continuing the experiments.</i>	26
<i>Table 5: Wear test resume.</i>	27
<i>Table 6: Summary of the peaks with relative temperature range and associated reaction/phase transformation.</i>	35
<i>Table 7: Macro hardness value in HV and their standard deviation of the isothermal treated samples.</i>	38
<i>Table 8: Worn volume and width collected by profilometer measurement. Wear rate is the ratio between worn volume and total distance of the test.</i>	40
<i>Table 9: Atomic composition of platelets and debris from RT18.</i>	46
<i>Table 10: Atomic composition of platelets and debris, RT65.</i>	46
<i>Table 11: Atomic composition of debris, RT1500.</i>	46
<i>Table 12: Depth, worn volume, and width from profilometer analysis. Wear rate is calculated as the ratio between worn volume and total distance.</i>	49
<i>Table 13: Atomic composition of the debris of HT wear tests.</i>	53
<i>Table 14: Average macro-hardness unworn surface.</i>	56



# 1. Introduction

Over the centuries, metallurgy has played a pivotal role in various fields of innovation and industry. Additive Manufacturing (AM) has garnered increasing attention in recent decades due to its advantages over conventional manufacturing techniques. Traditional metallurgical processes often encounter limitations in terms of shape complexity and tolerances [1]. In contrast, AM exhibits superior mechanical and homogeneous chemical properties. Furthermore, AM has the potential to positively impact sustainable manufacturing and the environment by reducing energy consumption and carbon footprint [2, 3]. Metallic additive manufacturing is one of the most impactful AM categories. In the last decades, the significant progress in metallic AM's constituent techniques has boosted it to become a mature and prevalent digital processing technology [2].

Among AM technologies, Laser Powder Bed Fusion (LPBF) is a suitable technique to produce metallic components. LPBF involves heating and melting powder material with a laser beam, followed by the rapid solidification of the melted material to form the desired shape [3]. The most used steels for LPBF are stainless steels, such as AISI 316L, AISI 304L, and maraging steels. However, these steels are often unsuitable for certain applications due to their poor wear resistance. Tool steels with a medium to high carbon content ( $>0.4$  wt%) may be more appropriate for such applications. Nonetheless, there is a lack of knowledge regarding tool steel for LPBF, due to their difficult processability. For this reason, over the recent years, there has been increasing attention on the development of tool steels by LPBF and the understanding of their microstructural and mechanical properties.

This Master's Thesis is part of a broader PhD research project that aims to fabricate innovative new alloys LPBF, specifically focused on the achievement of enhanced tribological properties. The basis of this work lies in the development and processability of AISI S2 tool steel by LPBF, previously investigated in other works of the Metallic Materials Science (MMS) team [5, 6]. The main goals of this study are the understanding of the thermal stability of the AISI S2 tool steel and its wear properties, ranging from room temperature until 400 °C. DSC analyses, pin-on-disc campaigns, macro- and nano- hardness, optical and scanning electron microscopy are combined for such purposes.



## 2. State of the art

This chapter provides a comprehensive review of the current state of knowledge on subjects pertinent to the discussion of the results. The primary subjects of relevance are: (1) Additive Manufacturing (AM) technology, with an emphasis on the Laser Powder Bed Fusion (LPBF) technology and tool steel for LPBF; (2) the thermal stability of tool steels, essential for understanding heat treatments and high-temperature wear tests; and (3) wear mechanisms and wear testing methods.

### 2.1 Additive Manufacturing (AM)

AM, also known as 3D printing [6], is recognized as a significant and rapidly evolving manufacturing technology [1] that has been researched and developed for over two decades [7]. In the past ten years, it has garnered substantial attention due to its immanent advantages, such as unrivalled design freedom and reduced lead times [8]. Furthermore, AM holds the potential to revolutionize global parts manufacturing and logistics [1], and obtain parts with geometrical and material complexities that cannot be produced by subtractive manufacturing processes [7], near net final shape, high-performance metallic parts [4, 5], good production velocity with consequently less costs. Additionally, AM is projected to positively impact the environment by reducing energy consumption and carbon footprint [1]. These benefits position AM as a desirable complementary approach to traditional manufacturing methods, making it a cornerstone of Manufacturing 4.0. AM is widely applied in many advanced sectors, such as aerospace, marine, defense [10], automotive, healthcare, energy [11], and biomedical [7] such as dental prostheses [12].

The ASTM F42 Technical Committee defines AM as the “process of joining materials to make objects from three-dimensional (3D) model data, usually layer upon layer, as opposed to subtractive manufacturing methodologies” [9]. Starting from a CAD model, AM enables the creation of parts in a final net shape, minimizing waste and material usage [7], without the need for molds, fixtures, or tooling, which can increase production times [10]. ASTM’s definition applies to all classes of materials, including metals, ceramics, polymers, composites, and biological systems [1]. In the context of metallic materials, ASTM indicated four categories of AM: Powder Bed Fusion (PBF), Direct Energy Deposition (DED), Binder Jetting (BJ), and Sheet Lamination (SL) [2].

As the field of additive manufacturing (AM) continues to advance, it becomes increasingly evident that the development of new alloys is essential to fully leverage the benefits offered by AM technologies [1].

### 2.1.1 LPBF process mechanism

Over the past few decades, Laser Powder Bed Fusion (LPBF), previously known as Selective Laser Melting (SLM) [13], has emerged as a particularly suitable technique among AM methods for producing near-net shape parts from powder. This technique involves the selective fusion of a powder-bed using a high-powered laser source [11, 12]. The LPBF process is currently regarded as the most versatile metal AM process [3]. It begins with the creation of a 3D CAD model, which is sliced into thin layers with selected scan paths [15]. If necessary, the initial step of printing involves preheating the platform to ensure a constant and controlled temperature [14]. The preheating step can improve the processability, mitigate the lack fusion and cold cracking defects, and reduce the residual stresses [13, 15]. The LPBF operates within an inert gas-protected chamber to prevent oxidation and contamination [17]. The powder feeding system distributes a thin, uniform layer of powder over the platform. Then the laser selectively melts this 2D layer of powder, which solidifies assembled. This process is characterized by the interaction between the laser and the powder, which includes a numerous physical phenomenon such as absorptivity of powder to laser radiation, balling phenomenon, and thermal fluctuation [11]. Once a layer is completed, the platform is lowered by a distance equal to the layer thickness, a new layer of powder is spread on top of the previous one, and the process is repeated. This cycle is repeated until the 3D solid object is built [3]. Figure 1 shows a schematic illustration of the process.

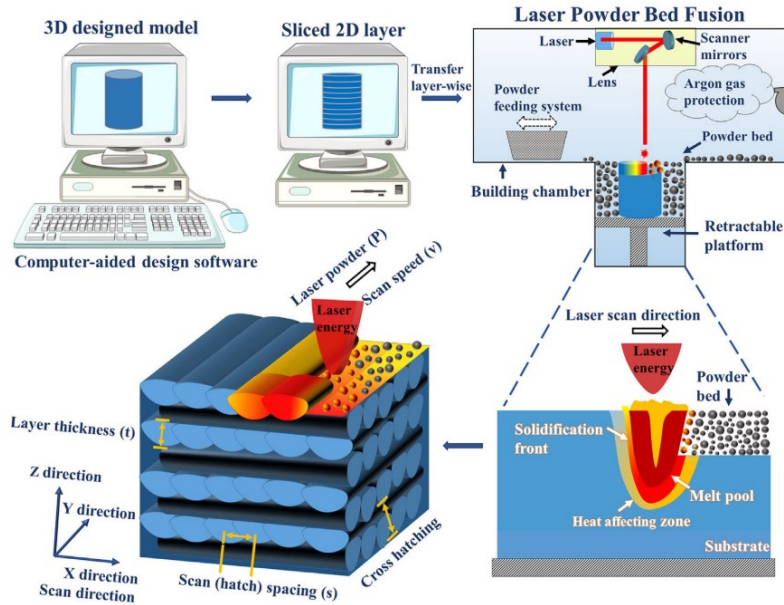


Figure 1: Schematic illustration of the LPBF process[18].

The cooling rate is significantly higher compared to the conventional casting process, approximately  $10^3$ - $10^6$  C/s [19]. Therefore, solidification occurs in out-of-equilibrium conditions [20]. The

continuous passage of the laser causes a re-melting of the top portion of the previous layer to ensure proper attachment of each successive layer (Figure 2). This re-melting process results in a complex thermal history for the microstructure [1]. The area affected by the passage of the laser is called the Heat Affected Zone (HAZ) [21]. The final microstructure of the LPBF is extremely related to the process parameter and the in-situ heat treatments. In general, the microstructure reveals melt pools generated by the laser beam with orientation based on the chosen scanning strategy [22].

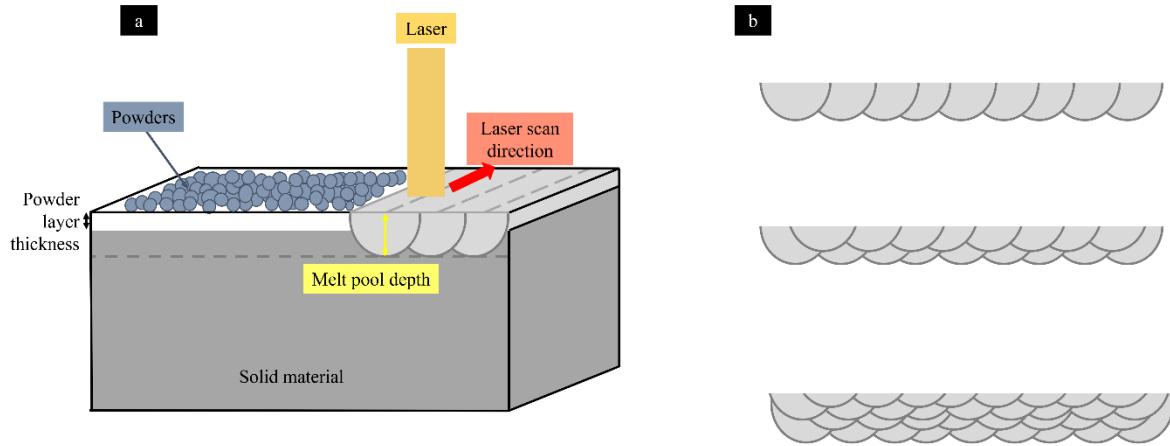


Figure 2: a) sketch of LPBF process showing melt pools and re-melting of the previous layer; b) overlap of the melt pools horizontally and vertically.

The microstructures of LPBF alloys are typically characterized by columnar dendritic grain structures due to the epitaxial grain growth mechanism prevalent in AM processes [19, 20] (Figure 3). The laser effect combined with the high cooling rate led to a cellular dendritic microstructure, which may cause high dislocation density [24]. Different primary solidification modes may be formed. Dendrites are created by rapid solidification [25], while equiaxed structures may be caused by a locally reduced temperature gradient [16].



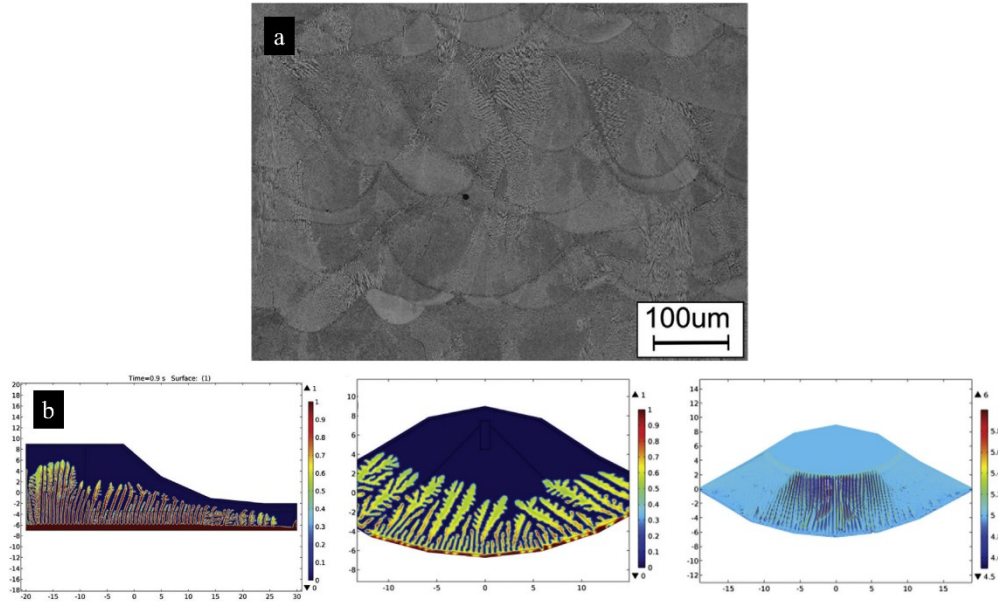


Figure 3: a) Micrograph of the melt pool; b) example of numerical simulation of dendritic solidification in LPBF.[26]

### 2.1.2 Tool steel for LPBF

Tool steels are a category of iron-based alloys characterized by the presence of alloying elements, such as molybdenum, vanadium, tungsten, and chromium. These steels exhibit superior strength, hardness, and wear resistance relative to other types of steel [27]. Additionally, many tool steels exhibit significant microstructural stability at elevated temperatures. Tool steels are extensively utilized in industrial applications, including dies, molds, cutting tools, and others. In designing tool steel, the selection of its composition and heat treatment parameters aims to achieve a hardened and tempered martensitic matrix with a uniform distribution of carbides. This configuration ensures that the matrix possesses an optimal combination of hardness and toughness [27].

Developing a technique for printing tool steels using LPBF is challenging due to the material's excellent mechanical properties and relatively low cost [23, 28]. In the literature, examples of tool steel manufactured using SLM/LPBF already exist [21, 23, 28, 29, 30, 31, 32, 33, 34]. However, the results of these various studies have demonstrated the necessity of conducting specific investigations for each material type to understand the process map, as issues such as inhomogeneity, porosity, or lower-than-desired mechanical properties may arise. Therefore, while existing literature provides valuable insights, a tailored examination is indispensable to optimize the fabrication process and ensure the desired material characteristics. Inappropriate parameters can lead to incomplete fusion of powders and subsequent defects, such as lack-of-fusion due to insufficient molten track penetration into the substrate [29], or balling when laser power and scan speed are excessively high [21, 28]. Other examples include porosity or insufficient overlap of the scan track [31] and microcracks caused

by excessively high residual stresses [34]. These defects not only diminish mechanical properties but also alter the microstructure. For example, lack-of-fusion defects can result in untempered martensite formation due to the absence of subsequent heat transfer [33].

Martensitic low alloy steels, in particular, are of growing interest for AM as they provide high strength, wear resistance, toughness, and hardness while maintaining relatively low cost [14]. Moreover, 3D printing of tools can save resources, shorten manufacturing times, and improve part quality [35]. Additionally, AM of tool steel has demonstrated superior surface wear properties and higher hardness compared to conventionally cast materials [28]. The microstructure of LPBF-printed martensite steel is in a non-equilibrium state: the molten region after solidification is austenitic and, upon rapid cooling, it transforms into martensite. The martensite then undergoes multiple intrinsic thermal cycles inherent to the LPBF process [18, 28]. At the end of the printing, the microstructure exhibits the typical hierarchical structure of LPBF-manufactured tool steel [36], characterized by epitaxial growth, comparable to conventional welding [3]. This hierarchical structure is formed through the layer-by-layer deposition of molten metal, which solidifies rapidly and undergoes repeated thermal cycling, promoting distinct melt pool boundaries (Figure 3). Melt pool structures with tempered and untempered martensite regions are observed in these steels [23]. Occasionally, bainite or austenitized zones may be also detected (Figure 5) [4], but generally in AM-produced tool steel martensite, martensite is the predominant microstructure due to the high cooling rate [37].

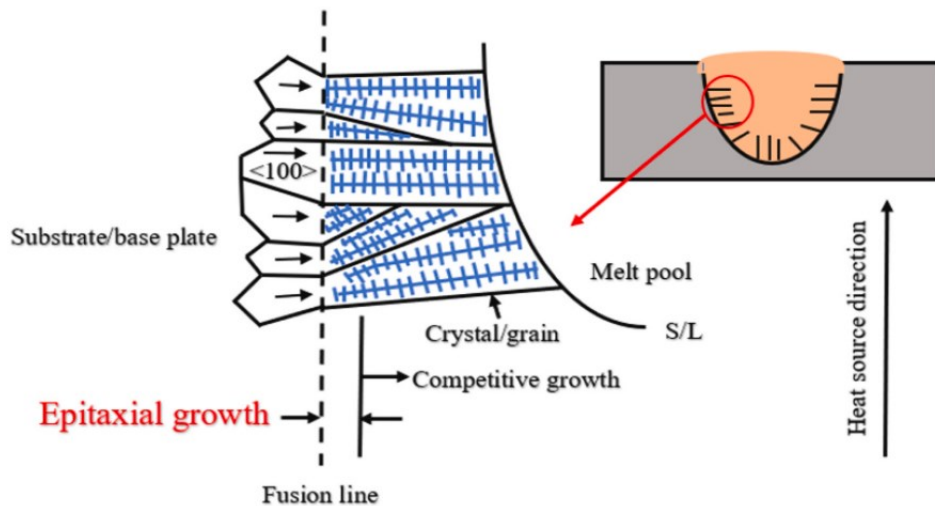


Figure 4: Schematic illustration of epitaxial growth. [3]

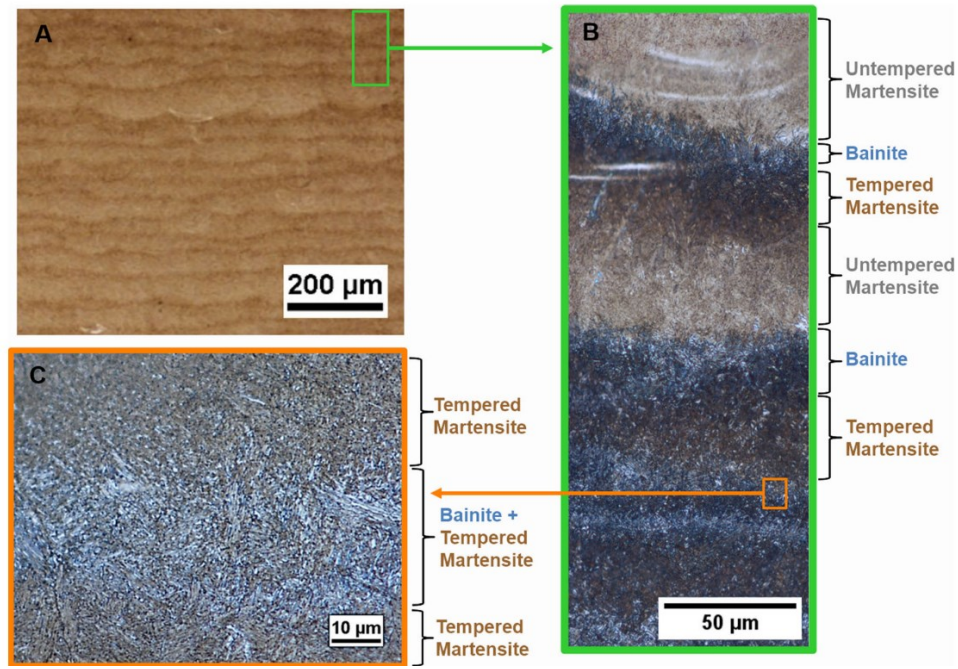


Figure 5: Microstructure of LPBF steel characterized by tempered and untempered martensite and bainite.[24]

LPBF microstructures are further characterized by the presence of cellular segregation structures [20, 29, 32] (Figure 6), which can increase the material's strength and dislocation density [24]. This combination of rapid solidification, high thermal gradients, and repeated thermal cycles results in a complex, fine-scale microstructure [3, 33, 34].

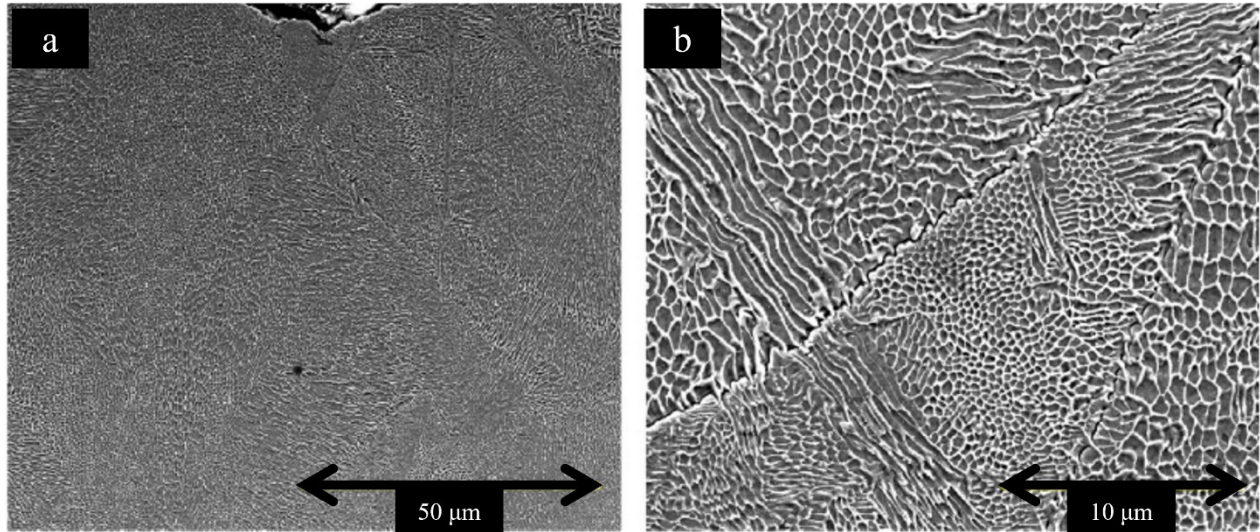


Figure 6: SEM micrographs of martensitic LPBF steel showing cellular structure at a) 50  $\mu\text{m}$  and b) 10  $\mu\text{m}$ . [30]

## 2.2 Thermal stability of tool steel

Since tool steels are utilized in numerous high-temperature applications [39], investigating the thermal stability of the AM-produced tool steel is imperative since conventional tool steels are stable up to 550°C [40]. This is further warranted by findings in the literature indicating that LPBF-produced tool steels exhibit properties distinct from those manufactured using conventional methods [41].

Additionally, the need for high-performance tool steel has grown because of the demand to achieve excellent mechanical properties at low cost [42].

One of the primary effects of heat treatments is oxidation, which occurs across the entire surface and can penetrate deeper depending on the duration of the treatment [43] and consequently can affect the mechanical properties of the steel.

LPBF tool steels exhibit a tempering resistance tool steels exhibit greater tempering resistance compared to those produced by conventional methods [44], due to their distinct microstructure. The initial step, in fact, is the homogenization of the microstructure, which begins with significant anisotropy in both phases and properties [45]. Many literature sources report the disappearance of the cellular structure and columnar dendrites as a primary consequence of heat treatment [44, 45, 46, 47]. This disappearance into the matrix leads to an increase in hardness and retardation of softening [48]. This disappearance of the hierarchical structure, combined with the typical precipitation of carbides due to tempering [44, 49], leads to an initial secondary hardening effect [44, 50] before a subsequent drop in hardness due to tempering sensitivity. In general, all mechanical properties undergo changes after thermal treatment. Bergmueller's study reported that the mechanical properties of heat-treated LPBF samples are generally superior to those of conventionally produced samples [45]. In particular, the Ultimate Tensile Strength (UTS) exhibits a good correlation with the hardness in the LPBF samples [51], as well as the wear resistance [52, 54], a topic of interest for this study. Other mechanical properties examined in various studies include thermal fatigue, which is reduced due to improved thermal conductivity after heat treatment [44], and fracture toughness, which is comparable to that of conventionally produced products [54].

## 2.3 Tribology

### 2.3.1 Types of wear

Wear is the process that occurs at the interfaces between interacting bodies, and it is often concealed by wearing components [55]. However, wear is not a material property but a response by a system of two or more components [41]. Seven different types of wear are explained in this section.

#### *Abrasive wear*

Abrasion is one of the most rapid and severe forms of wear with erosion. It is a type of wear caused by contact between a particle and a solid material [56]. Moreover, abrasive occurs when a solid object is loaded against particles of materials with equivalent or higher hardness. Abrasive wear can occur



with different mechanisms, as shown in Figure 7. These mechanisms depend on the properties of the material they interact with. Cutting or ploughing actions are common in ductile materials, while brittle materials tend to break or have grains pulled out. Consequently, these mechanisms can be categorized as causing plastic deformation in ductile materials and minimal deformation in brittle ones. However, exceptions exist, as some ductile materials may show brittle characteristics in certain areas of their surfaces [56].

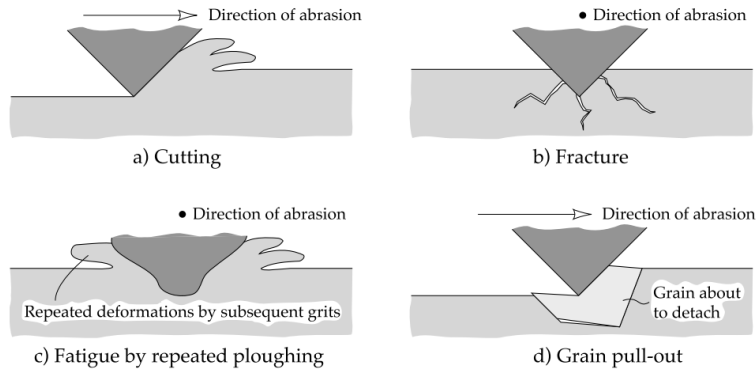


Figure 7: Mechanism of abrasive wear; a) micro-cutting; b) fracture; c) fatigue; d) grain pull-out.[56]

Additionally, abrasive wear can manifest in either two-body (Figure 8.a) or three-body modes (Figure 8.b). In the three-body mode, abrasive wear may contend with adhesive wear, emerging after the initial stages of abrasion, during which wear debris plays a contributory role in the process.

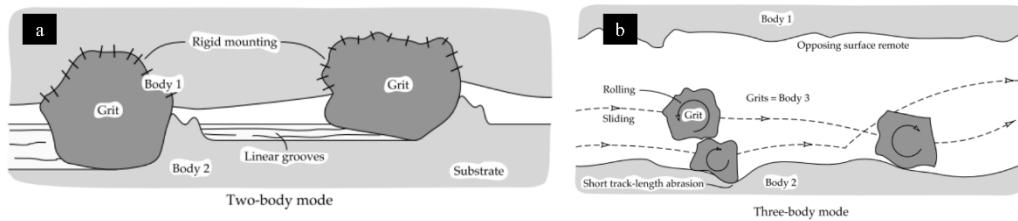


Figure 8: a) two-bodies abrasive mode; b) three-bodies abrasive mode.[56]

### Adhesive wear

Adhesive wear is a severe form of wear characterized by a high wear rate and unstable Coefficient of Friction [57]. This mode is due to the removal of material due to high adhesive force with high plastic deformation due to the removal (Figure 9).

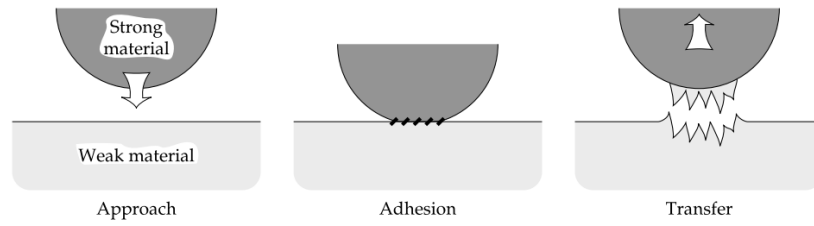


Figure 9: Schematic representation of adhesive wear.[57]

Adhesive wear progresses through several stages: initially, the establishment of bonding between two surfaces; followed by substantial plastic deformation, which hardens both materials; subsequently, the removal of the initial materials through crack propagation; and finally, the transfer of material (Figure 10). Throughout this sequence, the softer or sharper asperity material deforms in a succession of shear bands to accommodate the relative movement.

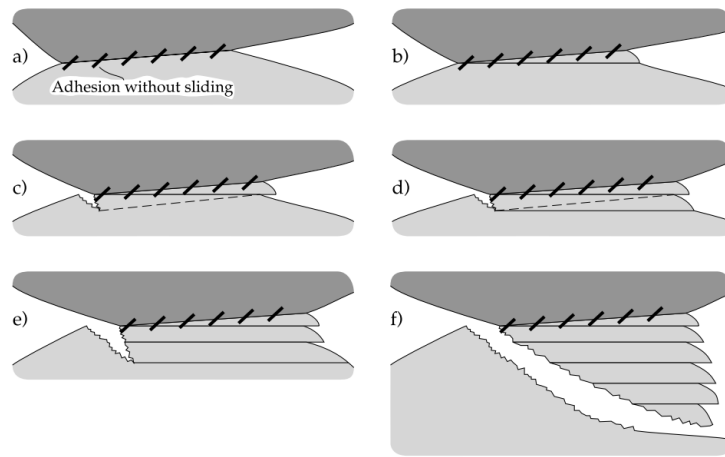


Figure 10: Schematic illustration of adhesive wear steps.[57]

### *Corrosive wear*

Corrosive wear involves various types of mechanical wear coupled with a chemical or corrosive process [58]. Sometimes instead of “corrosive wear” the term "tribocorrosion" is employed, particularly when electrochemical corrosion interacts with mechanical damage. Tribocorrosion issues are pervasive across mineral, nuclear, transportation, manufacturing, and food and drug production industries. Figure 11 illustrates four potential behaviours of corrosive wear: 1) a protective layer inhibits wear and corrosion formation, often due to lubricants or contaminants that act as a barrier, impeding the occurrence of the mechanism; this process is dominated by the formation of durable corrosion product layer which can acts as lubricating film; 2) the lubricant layer deteriorates due to its vulnerability, leading to increased wear as the substrate and contacting pin come into direct contact. In this scenario, the wear debris comprises both the protective layer and the substrate. Subsequently, a film grows in areas where material has been removed; this is the most common form of corrosive wear; 3) this scenario is related to wear in highly corrosive media, for example, galvanic or pitting

phenomenon; the protective layer experiences intermediate wear, resulting in coupling between the remaining layers and the substrate, leading to highly corroded zones with elevated wear rates; 4) corrosive and mechanical wear processes operate independently, resulting in a combined effect; this situation is limited to extremely corrosive environment. Wear rates are maximal among the four situations.

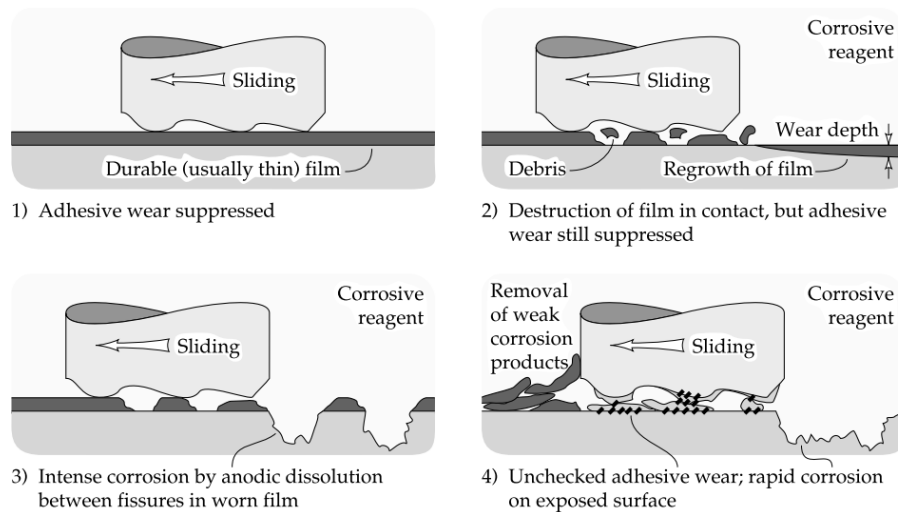


Figure 11: Schematic possible illustration of corrosive wear:[58]

### *Oxidative wear*

Oxidative wear should not be confused with corrosive wear. Oxidative wear involves a wear reaction where the material interacts specifically with oxygen. In contrast, corrosive wear encompasses any type of mechanical wear combined with a corrosive reaction. More generally, oxidative wear is typically defined as the wear of dry, unlubricated metals in the presence of air or oxygen gas.

In the initial stages of oxidative wear, surfaces come into contact and slide against each other, resulting in severe wear and forming a bond. This contact is not uniform across the entire surface, due to inherent surface roughness. Some areas experience higher contact while others do not contact at all. During this early interaction, plateaus begin to form, and oxide starts to develop in these zones due to the dry-sliding contact and the metal's reaction with oxygen. This initial phase of oxidative wear functions as a mild wear mechanism, characterized by a growing but stationary stage marked by the formation of an oxide film. As sliding continues, the oxide layer thickens and spreads, eventually reaching a critical film thickness. If the oxide layer continues to grow beyond this thickness due to ongoing contact and sliding, it fractures, with a rapidly increasing wear volume. Additionally, secondary hard phases may appear within the metallic substrate, further altering wear properties during subsequent passes and affecting future contact. In this final stage, contact is established in new areas of the surface, making the process repetitive [32, 36, 37].

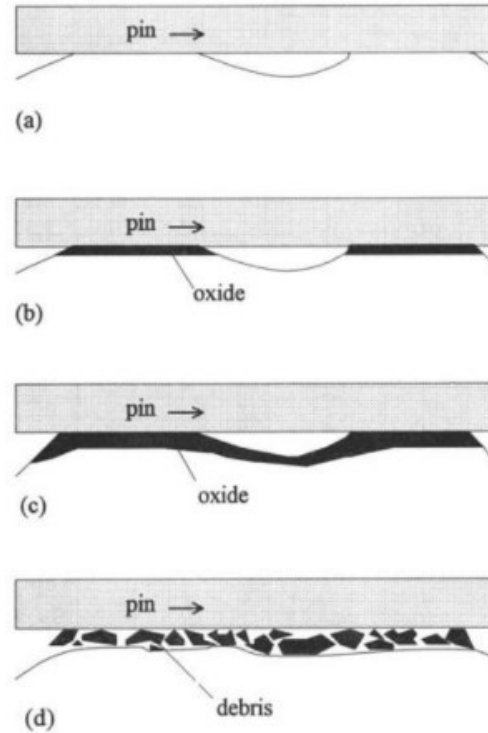


Figure 12: Schematic representation of oxidative wear steps.[60]

### *Erosive wear*

Erosive wear results from the impact of solid or liquid particles against the surface of an object. Mechanical strength alone does not ensure wear resistance, like in other forms of wear, necessitating a comprehensive study of material characteristics to minimize wear. Additionally, the properties of the eroding particles are increasingly recognized as a significant factor in controlling this type of wear [56]. The defining feature of erosive wear is "impact," which includes any type of wear involving particles striking surfaces and not fitting into other wear categories. In Figure 13, different types of erosive wear mechanisms are shown. The angle and speed of the particles, along with their size, determine the wear mechanisms that will occur. Low impact angles lead to abrasive wear, as the trajectory is nearly parallel to the surface. High impact angles result in more direct impacts, and depending on the speed and particle size, this can cause plastic deformation, brittle fracture, or even melting and embedding of the particle [56].



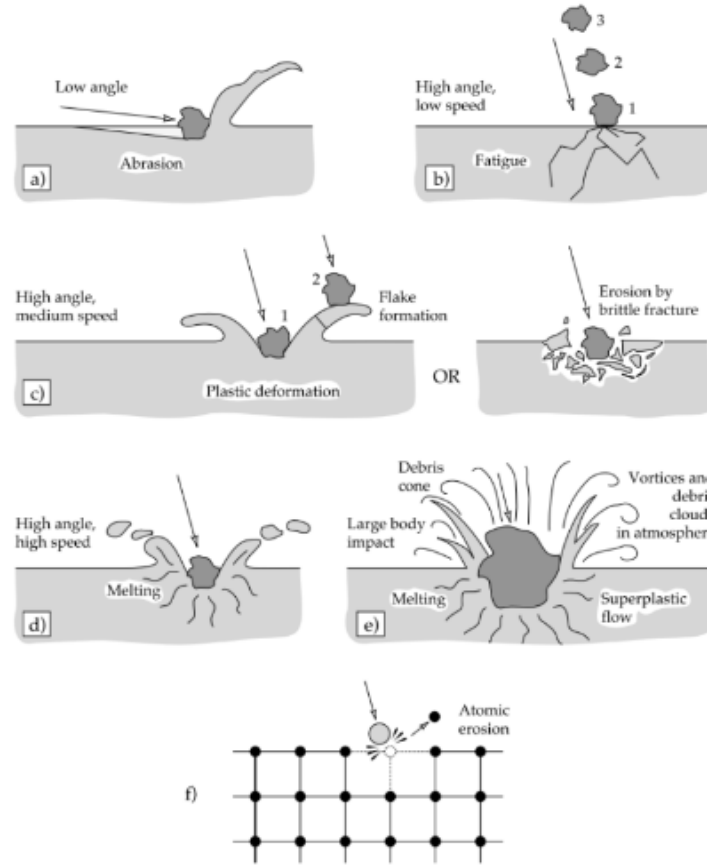


Figure 13: Schematic representation of an example of the mechanism of erosive wear. a) abrasion at low impact angles; b) crack formation due to high-angle impact at low speed; c) plastic deformation or brittle fracture due to high-angle impact at considerable speed; d) melting of the surface due to high-speed impacts; e) effect of a large particle in an erosive impact; f) effect of a tiny particle in an erosive impact (atomic-scale impact), leading to atomic erosion.

### Fatigue wear

Fatigue wear occurs in well-lubricated contacts despite minimal adhesion between surfaces, resulting from repeated high-stress contact between asperities. This process leads to the generation of wear particles (Figure 14.a) through fatigue-propagated cracks, driven by the mechanics of crack initiation, growth, and fracture. Worn surfaces exhibit high levels of plastic strain, altering the material's microstructure and affecting wear processes (Figure 14.a). “Contact fatigue” or “surface fatigue” refers to damage from repeated rolling contact, particularly in rolling bearings, which require smooth surfaces for reliable operation. Defects form after numerous rolling cycles, leading to excessive vibration and sudden bearing failure[61]. In Figure 14.b is schematically shown the mechanism of crack formation in fatigue wear. A primary crack initiates at the surface from a weak area and progresses downward along weak planes, such as slip planes or dislocation cell boundaries. Subsequently, a secondary crack may form from the primary crack, or the primary crack may intersect with an existing subsurface crack. Upon reaching the surface, the developing crack releases a wear particle.

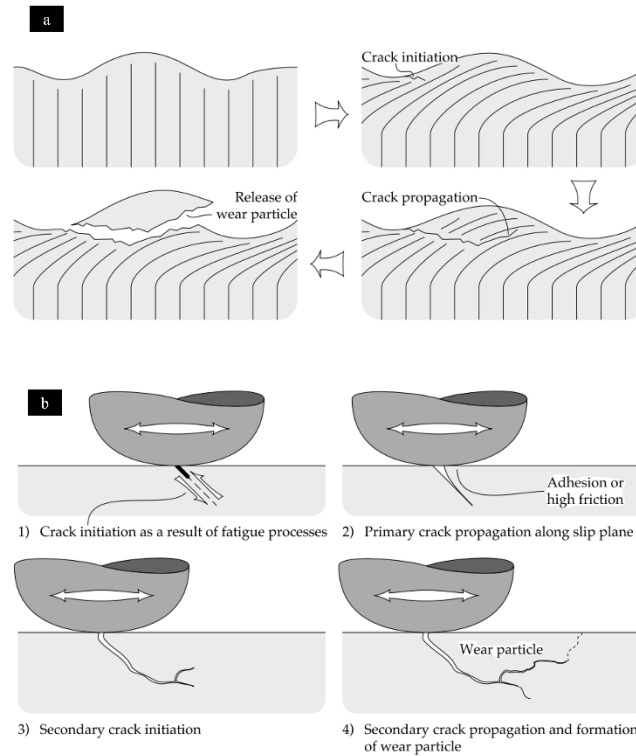


Figure 14: a) schematic illustration of the release of wear particles and plastic strain deformation of the subsurface; b) schematic illustration of crack formation in fatigue wear mechanism.[61]

### Cavitation wear

Cavitation refers to the swift transformation from liquid to gas due to a decrease in pressure. This process generates cavitation bubbles within the liquid, characterized by a significant implosive force [62]. This wear mechanism leads to the development of holes or pits in the surface exposed to cavitation, potentially destroying the machine component [56]. Therefore, when a bubble collapses on a surface the liquid adjacent to the bubble is at first accelerated and then sharply decelerated as it collides with the surface. The collision between liquid and solid generates large stresses which can damage the solid [56]. The mechanism of bubble collapsing is schematically shown in Figure 15.

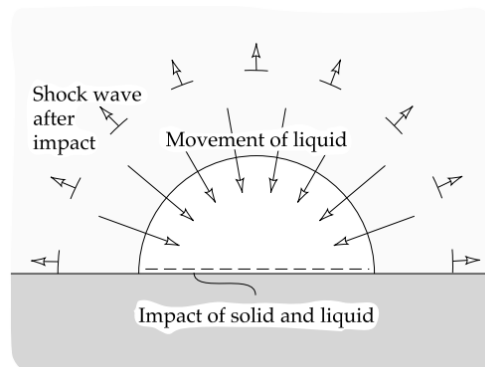


Figure 15: Mechanism of bubble collapsing in cavitation wear.[56]

### 2.3.2 Wear testing methods

Standard wear test methods have been developed under various ASTM technical committees [63]. The primary benefits of utilizing ASTM standard wear test methodologies include rigorous evaluation and meticulous documentation of the procedures, better-documented repeatability and reproducibility of results compared to specialized or unique wear testing apparatuses, availability of extensive prior data, facilitating convenient comparison with new results, and established documentation and reporting standards ensuring comprehensive and organized presentation of all relevant variables and outcomes. In this section, the principal wear test methods are explained.

#### *Pin-on-disc*

This thesis relies on the widely used pin-on-disc testing method, which is the most popular choice in the market. In this method, the sample rotates and acts as the disk, wearing down due to contact with a stationary ball or pin, creating a wear track. There's a variety of materials available for the balls. The choice of ball material usually depends on the tested sample, materials expected to wear less than the sample itself are used.

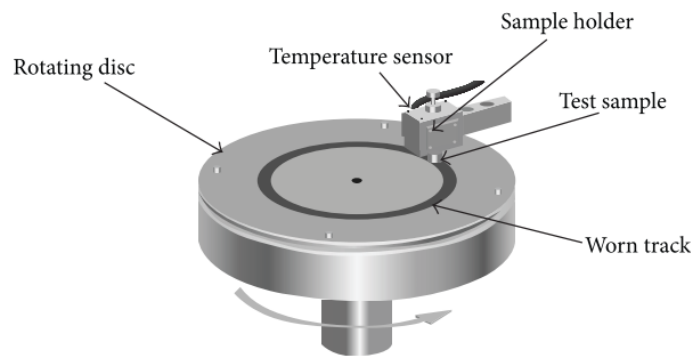


Figure 16: Pin-on-disc machine.[64]

#### *Four-ball test*

In this test setup, a load is applied to the top ball as it rotates, while the remaining three balls are stationary and immersed in lubricant. The primary objective of this test is to assess the anti-wear characteristics of the lubricant, rather than to examine the wear behaviour of the ball material.

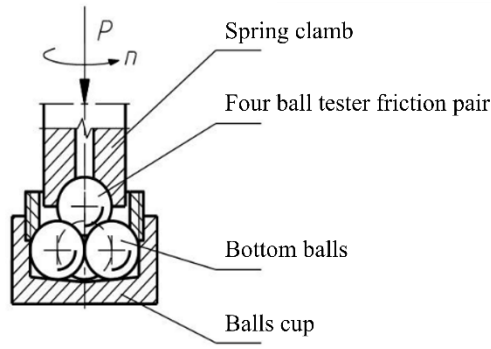


Figure 17: Schematic illustration of four ball tester.[65]

### *Reciprocating sliding friction*

The test utilizes a concept similar to the pin-on-disk method: the ball undergoes reciprocal sliding in one longitudinal direction and then reverses, resulting in a reciprocating motion that induces wear on the material. In the reciprocating sliding friction test, the specimen experiences reciprocal sliding in one longitudinal direction, followed by a reversal in motion. This back-and-forth movement generates frictional forces, leading to wear on the specimen's surface and allowing for the evaluation of its tribological properties.

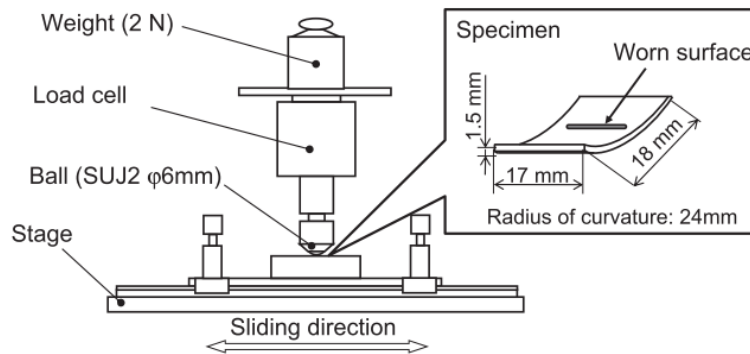


Figure 18: Reciprocating sliding friction scheme.[66]

### *Fretting wear testing machine*

Fretting wear arises from slight displacements between two surfaces under sustained load, often prompted by low-amplitude vibrations. Therefore, the apparatus requires high precision to ensure accurate and minute displacements. A fretting wear tester replicates these small, repetitive motions between surfaces under load. By measuring wear, offers valuable insights into material behaviour under fretting conditions, facilitating the advancement of durable materials and coatings.

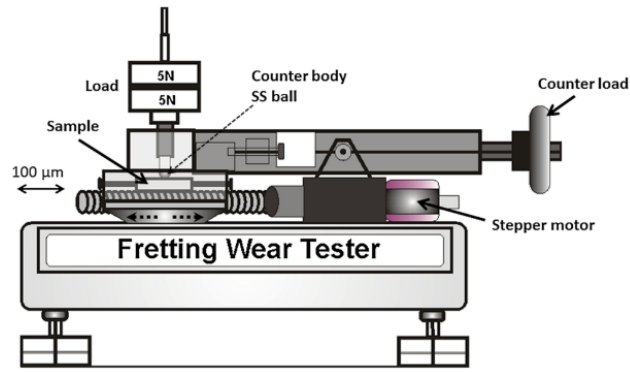


Figure 19: Fretting wear tester scheme.[67]

### 2.3.3 Wear behaviour of tool steel by LPBF

Wear resistance is a critical property for tool steels, as it directly impacts their performance and longevity in demanding industrial applications where tools are subject to high friction, abrasion, and mechanical stress. Residual stresses resulting from the LPBF process can influence mechanical properties, particularly wear resistance. The primary factor influencing wear resistance is the microstructure. In fact, Podgornik's work highlights the mitigation of anisotropy through pre-treatments before testing, underscoring the importance of microstructural control in optimizing wear resistance [68]. In numerous literature sources, greater wear resistance for LPBF tools and stainless steel compared to conventional counterparts is consistently reported [69, 70, 71]. Particularly, Kosiba's work [69] discusses methods to mitigate residual stress resulting from martensitic transformations induced by high cooling rates. One approach involves preheating before the printing process or altering the composition of elements to minimize residual austenite. Another strategy is the design of specific alloys for LPBF. Wear tests have demonstrated an improved resistance of LPBF-produced steel compared to conventionally manufactured steel (Figure 20.a). In the figure, the red point highlights the formation of grooves, which will subsequently extend across the entire track. Grooves and plastic deformation of them due to abrasive wear (Figure 21).

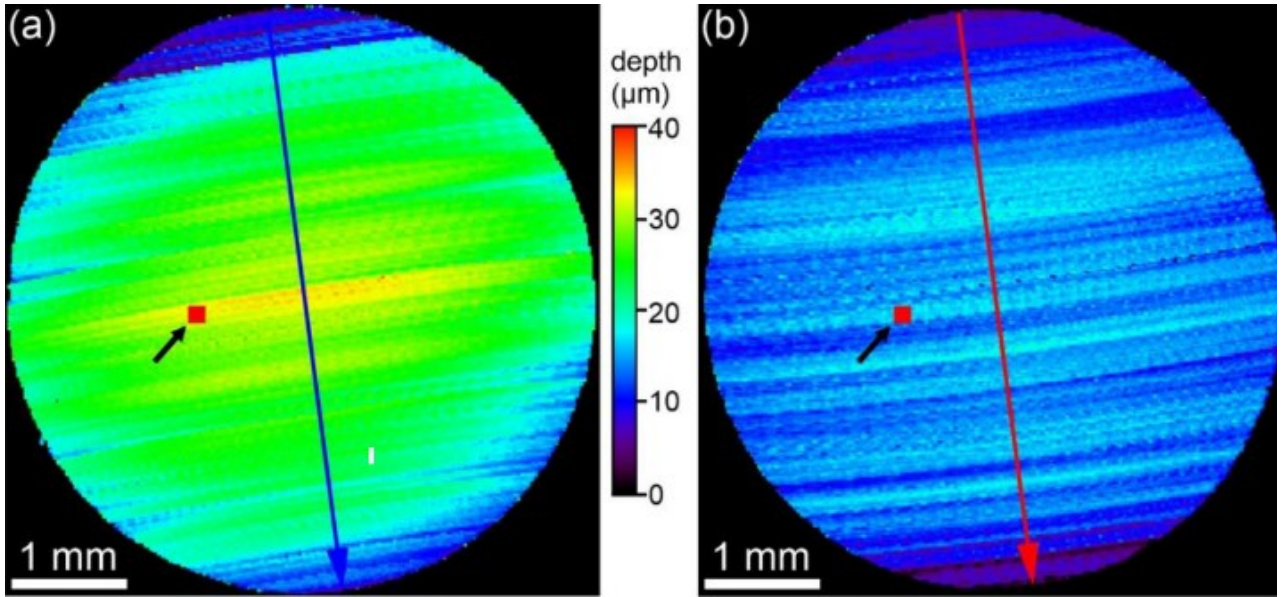


Figure 20: wear track of the same steel a) LPBF printed and b) conventional steel [69]

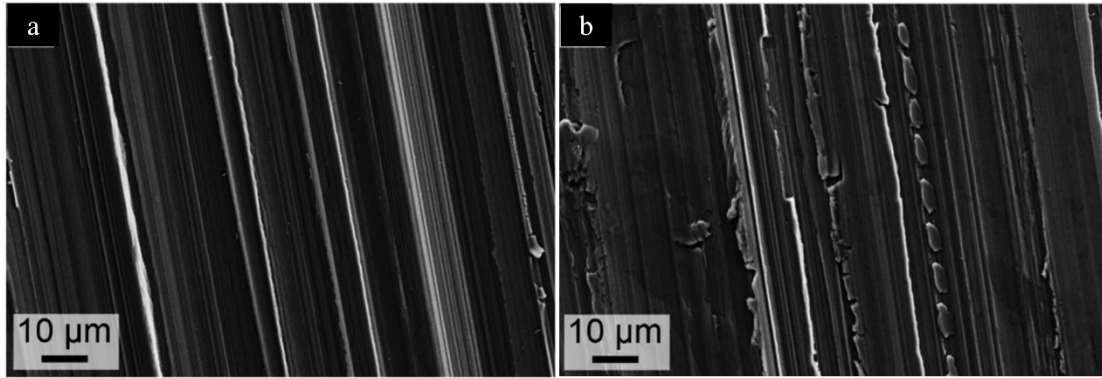


Figure 21: wear track of tool steel; a) grooves and b) plastic deformation of grooves.

In the work of Upadhyay and Kumar [70], a protective film that reduces friction and wear on the track was observed after several cycles. The authors determined that the formation of this tribo-layer is associated with the carbon content on the surface of the samples. The formation of the tribo-layer results in reduced microstructural deformation, as illustrated in Figure 22, where one part is labeled as the deformed layer and the other as smooth sliding. This particular layer formation allows LPBF-printed steel to exhibit superior wear properties compared to conventionally produced steel.

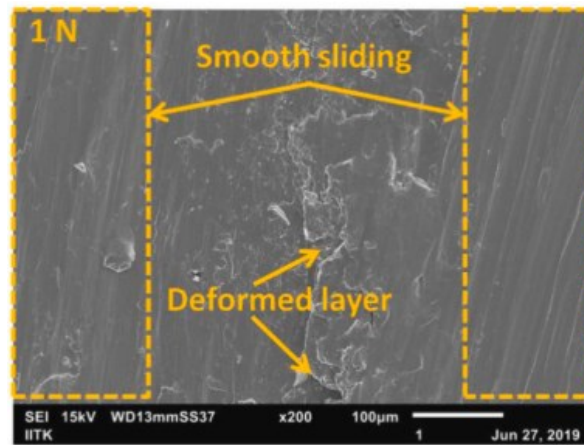


Figure 22: wear track with some deformed zone and smooth sliding.[70]

### 3. Materials and experimental methods

#### 3.1 Samples fabrication by LPBF

##### 3.1.1 Powders

The powder used to produce the samples is gas-atomized AISI S2 powder, supplied by Sandvik Osprey Ltd. Figure 23 shows the morphology of the powder. The chemical composition is listed in Table 1. Further details are available in Annex A.

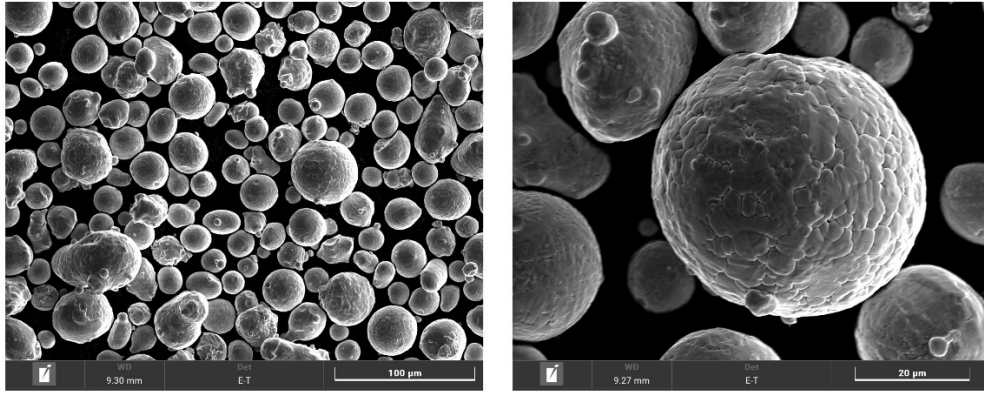


Figure 23: SEM micrographs of the S2 powders.

<i>Element</i>	<i>C</i>	<i>Si</i>	<i>Mo</i>	<i>Mn</i>	<i>Fe</i>
<i>% wt.</i>	0.49	1.2	0.6	0.6	Balance

Table 1: chemical composition analysis of S2 powder.

##### 3.1.2 Printing parameters

The samples were printed using an AconityMINI LPBF device, as shown in Figure 24. The processability of S2 powder was studied in previous works of the MMS team [1, 2]. Samples produced in this work were processed with the parameters that allow to achieve fully dense and defect-free parts (Table 2). Two types of samples were produced. One type will be used for the wear test. These samples have a parallelepiped geometry, with a height of 10 mm, a depth and width of 35 mm. According to the dimension of the substrate (140 mm in diameter), four samples were processed during one job (Figure 25). Sample 4 was not considered for further investigation, as it has many spatters on its surface. The second type of samples have a cylindrical geometry, and they will be used for thermal analysis.





Figure 24: AconityMINI machine. [72]

Preheating	No
Laser spot size	80 $\mu\text{m}$
Hatch Distance	80 $\mu\text{m}$
Layer Thickness	30 $\mu\text{m}$
Scan Strategy	90-90 Unidirectional
Contour	No
Supports	No
Power	200 W
Laser Scan Speed	1000 mm/s

Table 2: Parameters of printing

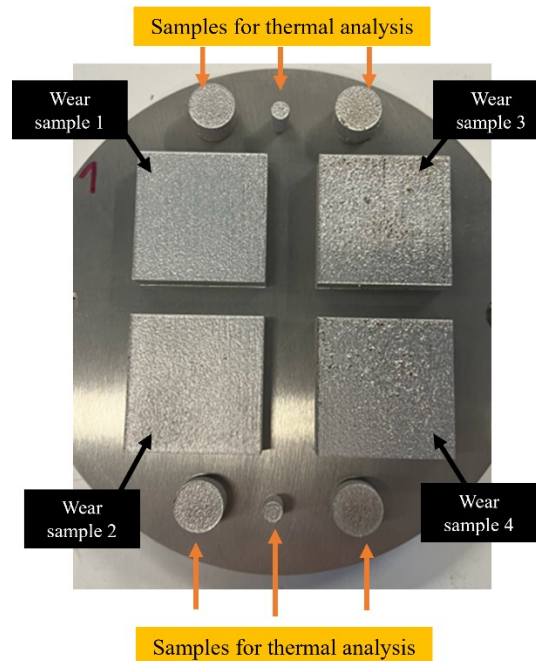


Figure 25: Printed samples. The black arrows indicate the samples for the wear test, and the orange arrows indicate the samples for the heat treatment.

### 3.2 DSC

After production, samples were cut from the substrate by electron-discharge machining. Pieces with a diameter of 5 mm and a height of 2 mm were obtained from the cylinders (Figure 25), in order to fit within the alumina crucible of the DSC. The DSC was a Jupiter - 404C (Figure 26). Based on the results of a previous work of the MMS team [5], three isothermal treatments were carried out at

200°C, 300°C, and 400°C. Further information about the choice is given later in section 4.0. The heat treatments consisted of heating at a rate of 5°C/min until the target temperature, followed by an isothermal segment for 5 or 10 hours and finally cooling at 20°C/min until room temperature. The goal of these tests was to identify possible changes in microstructure due to different thermal treatments. Table 3 lists all the tests performed and Figure 27 illustrates the treatments schematically.



Figure 26: DSC Jupiter -404C from NETZSCH [73].

Time	Temperatures		
5 hours	200°C	300°C	400°C
10 hours	200°C	300°C	400°C

Table 3: Isothermal tests performed. Three tests were performed for 5 hours, the other three for 10 hours.

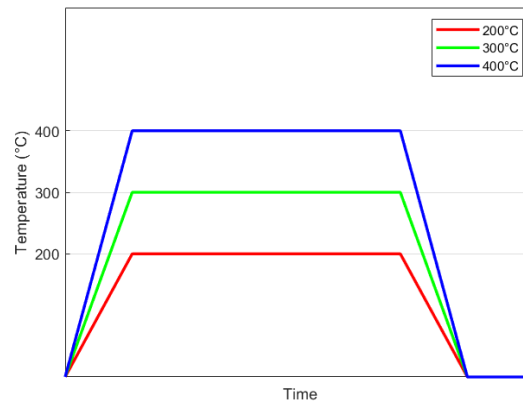


Figure 27: Schematic illustration of the thermal treatments. Isothermal segments are 5 or 10 hours.

### 3.3 Microstructure characterization

#### 3.3.1 Sample preparation

Samples were embedded within a cylindrical bakelite using a STRUERS Citopress-1. The cylindrical sample was then polished down to 1µm in multiple steps using the STRUERS Tegramin-30, in order

to obtain a sample with very low roughness and a clean and plane surface. After polishing, the samples were etched with Nital 3% to highlight the microstructure.

This entire procedure was carried out on both the heat-treated samples and the cross-section of the wear track, with the aim of observing the evolution of the microstructure.

### 3.3.2 Optical Microscope (OM) and Stream Analysis Software

Microstructure observations were conducted using an Olympus BX60 microscope (Figure 28) with magnifications of 2.5x, 5x, and 10x. The observations were performed on the microstructure after thermal treatments and on the entire wear tracks. The focus of microstructural observation was to determine the different dimensions and geometry of the melt pool and analyze the wear tracks. The Stream Analysis Software was used to analyze the pictures taken with OM. Stream is an advanced software that permits image acquisition, processing, and measurement.



*Figure 28: Olympus BX60 [74].*

### 3.3.3 Scanning electron microscope (SEM)

A Tescan Clara Ultra-High Resolution (UHR) SEM (Figure 29) was used to investigate microstructure at high magnification. Samples after heat treatments, wear tracks, and cross-sections of the wear tracks were investigated. Moreover, Energy Dispersive Spectroscopy (EDS) was used to recognize the element composition in different zones, either at single points or a line, to understand the possible formation of oxides during wear tests and the composition of the debris.



Figure 29: Tescan Clara Ultra-High Resolution SEM machine [75].

### 3.4 Wear tests

#### 3.4.1 Pin-on-disc tribometer

Samples for wear tests were obtained by horizontally cutting the original printed parts (Figure 25) to obtain two wear samples and four faces for every printed sample (Figure 30). The designation of the wear samples includes the number of the sample given by its position in printing and the name of the face. From up to bottom: T (top surface), M2 (middle surface opposite to top), M1 (middle surface opposite to bottom), B (bottom surface) as illustrated in Figure 31.

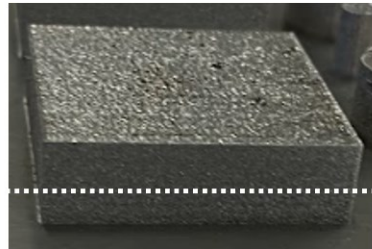


Figure 30: Sample cut for the wear test. The white line is the cutting, for each printed sample four faces will result.

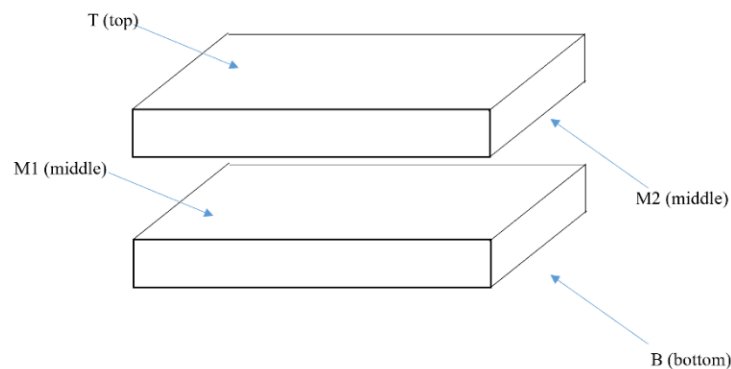


Figure 31: Schematic illustration of wear sample designation from one cut printed sample.

After cutting and polishing, spatters and defects were detected in some samples, thus allowing for the removal of those unsuitable for the application. In Table 4 all the obtained wear samples are shown, the samples highlighted in green are the ones chosen for continuing the experiments.

Sample 1	Sample 2	Sample 3	Sample 4
1T	2T	3T	4T
1M2	2M2	3M2	4M2
1M1	2M1	3M1	4M1
1B	2B	3B	4B

Table 4: All printed samples after cutting. The green highlights are the ones chosen for continuing the experiments.

Wear tests were performed with the High Temperature Tribometer 01-04611 by the “CSM Instruments SA” company (Figure 32). Both room and high-temperature tests were performed using different samples. The test samples were cut and polished. All the tests were performed using a 6 mm diameter Alumina ( $\text{Al}_2\text{O}_3$ ) ball as the counter-body, with a consistent velocity (10 cm/s) and load (10N) maintained throughout. When possible, two tests were performed on the same face by adjusting the test radius. The Tribometer software collected data and graphs of the Coefficient of Friction (CoF), penetration depth, sample and oven temperature, and friction force during tests. At room temperature, an initial long test of 1500 m (Test RT1500) was conducted. Subsequently, to analyze the evolution of the CoF and the wear sequence, two interrupted tests (RT18 and RT65) were carried out based on the CoF graph of the RT1500 Test, halted at 18,05 m and 65,04 m respectively. This experimental approach of interrupted tests had been previously developed in other experiments of MMS teams [76]. Once the performance of the CoF at room temperature was investigated, high-temperature long-distance wear tests were performed. The temperatures (200°C, 300°C, and 400°C) were consistent with those used in the thermal treatments (section 3.2), allowing for comparison of microstructure changes between thermal treatments and during wear tests. Each of the four long-duration tests (RT1500, HT200, HT300, and HT400) had a duration of over four and a half hours. Specifically, the high-temperature tests proceeded in three steps: first, the entire chamber was brought to the set temperature, then the test was conducted, followed by the final step involving cooling to room temperature.



Figure 32: High Temperature Tribometer [77].

At the end of the experiments, a total of six wear tests were conducted: three at room temperature and three at high temperature (200°C, 300°C, and 400°C). A summary of these tests is shown in Table 5.

Name of Test	Face used	Distance [m]	Track radius [mm]	Temperature
RT1500	3M2	1500	11	Room
RT65	1M2	65,04	11	Room
RT18	3M2	18,05	8	Room
HT200	2B	1520	11	200°C
HT300	1T	1520	11	300°C
HT400	1M1	1520	11	400°C

Table 5: Wear test resume.

Following the wear test, an electro-discharge machine was used to obtain transversal sections parallel to the sliding direction. This was done to observe the subsurface microstructure of the wear tracks as shown in Figure 33. The subsurface sample was hot mounted using a conductive resin then ground and polished down to 1  $\mu\text{m}$ . The procedure is similar to the one explained in section 3.1.2.

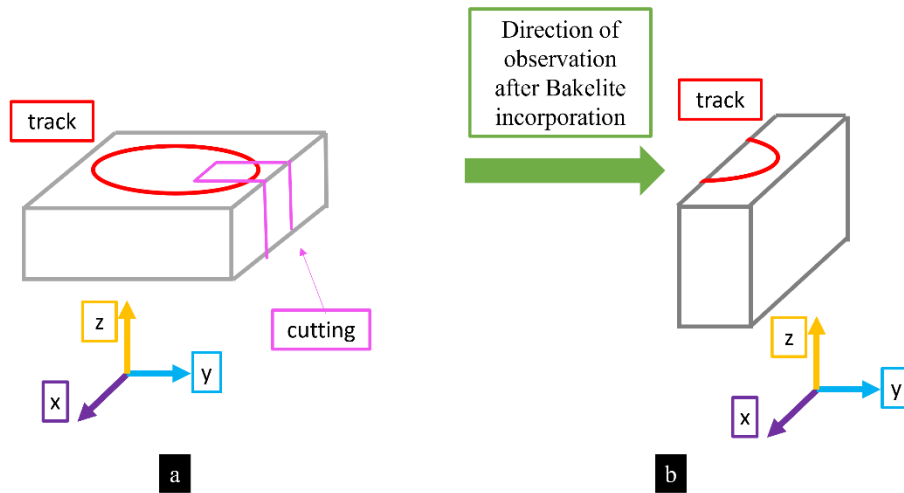


Figure 33: Schematic illustration of a) cutting of a piece to see the cross-section under the track; b) piece after cutting before bakelite incorporation and polishing; in green highlight the direction where the cross-section will be seen (xz plane).

### 3.4.2 Profilometer

The Alicona InfiniteFocusG5 (Figure 34) was used to analyze the wear tracks and the surface of the  $\text{Al}_2\text{O}_3$  counter-body after each test. This machine employs a non-contact, optical, three-dimensional measurement principle based on Focus-Variation. The primary component of the system is precision optics containing various lens systems that can be equipped with different objectives, enabling measurements [78]. The instrument's objective magnification is up to 100x.



Figure 34: Alicona InfiniteFocusG5 [78].

This instrument was utilized after each wear test to assess the worn volume and the width of the track, as well as to capture micrographs displaying wear variations in different colours. Additionally, the counter-bodies were analyzed to understand their wear.

## 3.5 Hardness

### 3.5.1 Macro hardness

Hardness indentations were performed on the samples after the 5- and 10-hour isothermal treatments, as well as on the unworn surface of the wear tests. The machine used for this experiment was an EMCO M1C 010 (Figure 35). The position of every indentation was manually set, and the load remained consistent for every test (HV5). The purpose of these tests was to compare the results to better understand the microstructural changes after thermal treatment.



*Figure 35: EMCO M1C 010 hardness machine [79].*

### 3.5.2 Nano-hardness

Nano-indentations were performed in the cross-section of the wear tracks using a TI 950 Triboindenter nanoindenter supplied by the “Hysitron” company (Figure 36).





*Figure 36: TI 950 Tribometer nanoindenter [80].*

Nano-hardness indentation grids were conducted within the subsurface regions of the wear tests to elucidate the evolution of nano-hardness across various sections beneath the worn track and to discern potential microstructural alterations resulting from the interaction with the counter body. These grids spanned dimensions of  $36 \times 36 \mu\text{m}$ , comprising  $25 \times 25$  points. The spacing between individual points was consistently maintained at  $1.5 \mu\text{m}$ , with a displacement of  $100 \text{ nm}$ .

## 4. Results

### 4.0 As-built microstructure and DTA thermal treatments

The as-built microstructure was previously investigated in another Master's thesis that was developed by the MMS team [5]. In that thesis, printing parameters, processability map of AISI S2 tool steel, and microstructure after printing (as-built) were examined. The microstructure exhibited the characteristic melt-pool structure typical of LPBF-printed steels. In Figure 37.a is reported the schematic passage of the laser and the creation of the melt pool. In Figure 37.b the building direction is highlighted. The primary phenomenon at play is referred to as "epitaxial grain growth", where grains persist in growing from a previous melt pool to a new one. The selected scanning strategy for this material suggests a preference for columnar growth, with epitaxial growth being predominant alongside a cellular dendritic structure [5]. As the solidification process takes place, the grains exhibit a tendency to expand towards the center of the melt pool in the travel path of the laser beam, aligning with the direction of the highest temperature gradient. Consequently, this results in the occurrence of a side-branching phenomenon, as the growth progresses with varying orientations in accordance with the building direction (Figure 37.c and Figure 37.d). The formation of a new layer that merges the uppermost part of the previously formed layer is shown in Figure 37.e.

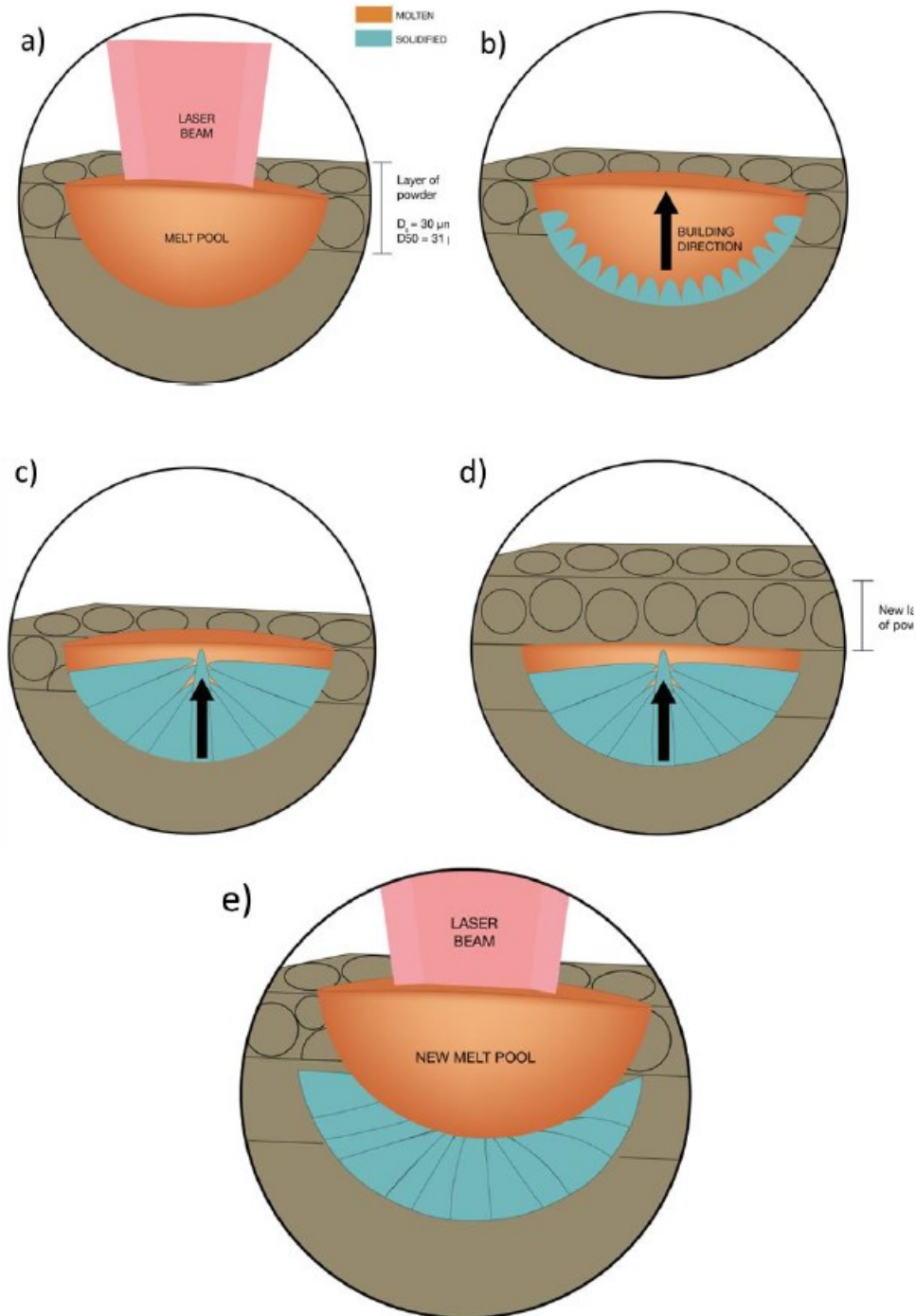


Figure 37: Sketch of the process of melt pool solidification. (a) Melt pool with molten powders after the laser travels by; (b) primary nucleated grains following the orientation of the building direction within the melt pool border (c) epitaxial growth with side-branching phenomenon of the nucleated grains (d) addition of a new powder layer (e) the process new step, which affects the microstructure of the layers below [5].

Within each grain, the primary solidification mode is cellular. Cells growth follows the orientation of the thermal gradient, as in the case of the parent grains. Cellular growth is highlighted by intercellular segregations, which appear bright under SEM (Figure 38).

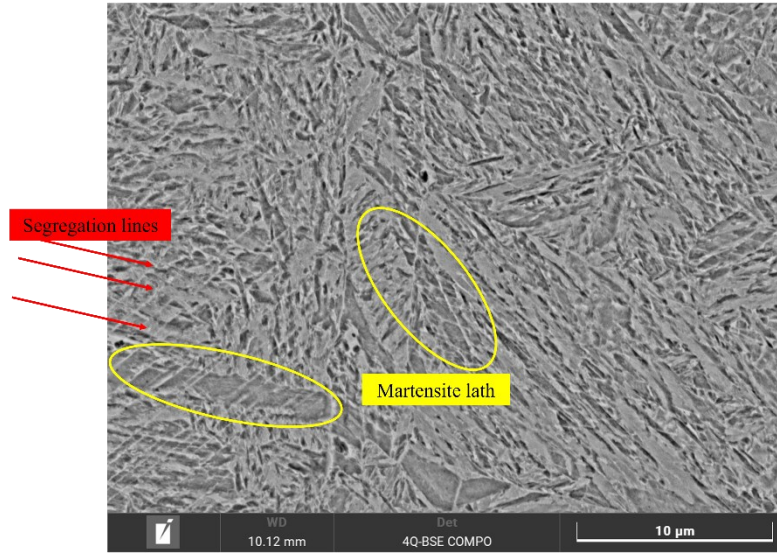


Figure 38: SEM micrograph. Segregation, laths of martensite, and precipitations are highlighted.

The continuous passage of the laser during printing caused in situ heat treatment on the previously formed layer (Figure 37.e), as indicated by the presence of Heat Affected Zones (HAZs). The top layer, which was not heat affected, consists of untempered martensite (Figure 39.a). The latter was formed due to rapid cooling. Below the melt pool boundary, untempered martensite was still formed, in view of the high temperature reached in this area. In the current study, the top layer was discarded by operating a rectification on the surface of the as-built sample. Below the top layer, austenization zone (Figure 39.d and Figure 39.g), bainite (Figure 39.e and Figure 39.h), and tempered martensite (Figure 39.f and Figure 39.i) were formed increasing the distance from the melt pool. Without considering the untempered martensite within the top layer, the microstructure revealed homogeneous macro-hardness, with an average value of  $556,66 \pm 15,17$  HV5.



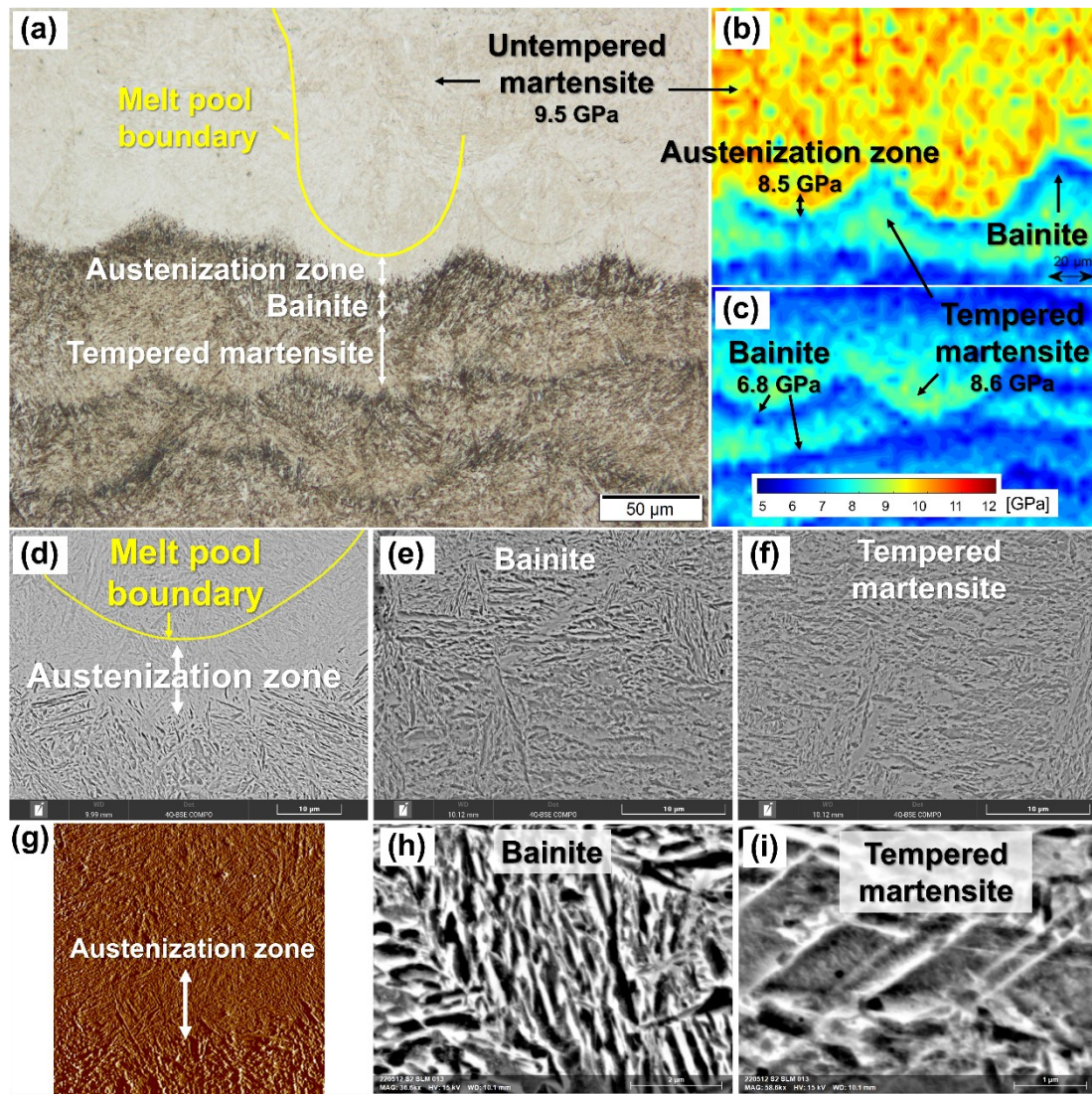


Figure 39: (a) Heat-affected zones and (b, c) their nano-hardness. Higher magnification of the (d) austenization zone, (e, h) bainite, and (f, i) tempered martensite. (g) Austenization zone revealed by scanning the surface with the scan mode of the nano-indenter.

In the same Master's thesis [5], DTA analyses were carried out up to 1550°C to achieve complete melting of the S2 steel (Figure 40.a). The first endothermic peak (H1 = 760°C) corresponds to the transformation of martensite into austenite. At temperatures ranging from 1400° to 1500°C, two additional peaks (H2 and H3) correspond to the reverse peritectic transformation, during which austenite is converted into  $\delta$  ferrite and liquid (Table 6). The red rectangle in Figure 40.a represents the selected zone of interest in this work, which precedes the austenitic transformation. From these zones, three temperatures were selected for the investigation of the thermal stability and the high temperatures wear tests: 200°C, 300°C, and 400°C. In Figure 40.b, a zoom of the DTA curves is shown, with the chosen temperatures highlighted by red circles and arrows.

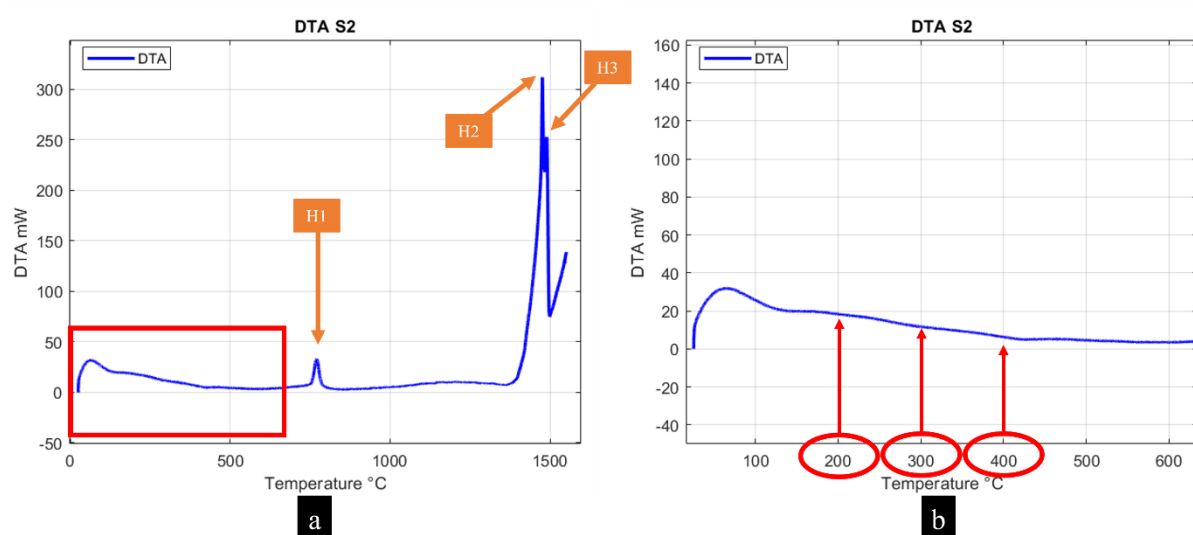


Figure 40: DTA curves of S2; a) shows the complete curve with the red rectangle that highlights the zone of interest; b) is a zoom of the curve a) with the selected temperatures highlighted by red circles and arrows.

Peak	Start Temperature	End Temperature	Reaction/phase transformation
H1	760°C	820°C	Martensite → Austenite
H2	1450°C	1490°C	Austenite → $\delta$ Ferrite
H3	1500°C	1530°C	$\delta$ Ferrite → liquid

Table 6: Summary of the peaks with relative temperature range and associated reaction/phase transformation

## 4.1 Microstructure after thermal treatment

### 4.1.1 DSC analyses

Isothermal heat treatments of 5- and 10- hours duration were conducted with a DSC machine under a controlled atmosphere. This test aimed to monitor for any peaks during the extended maintenance period. In Figure 41, DSC maintenance curves of 10-hour treatments are reported, and no significant peaks were observed at the end of the tests.

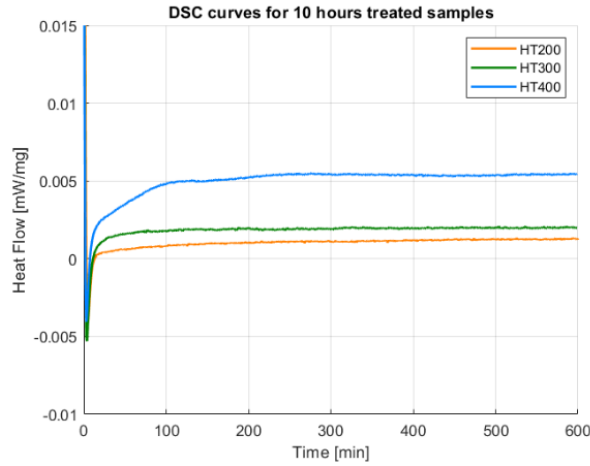


Figure 41: DSC curves for isothermal maintenance with Heat flow plotted on time.

#### 4.1.2 Microscope observations

OM and SEM observations of the microstructures after DSC heat treatment for 5 and 10 hours appeared similar. For ease of description, in what follows, only samples obtained with 10 hours of heat treatment are reported.

Micrographs of the heat-treated samples are shown in Figure 42. The samples treated at 200°C and 300°C (Figure 42.a and Figure 42.b) exhibited typical LPBF patterns, melt pool morphology and HAZs. Instead, the sample treated for 10 hours at 400°C appeared more homogeneous in microstructure (Figure 42.c), since the HAZs are less visible.

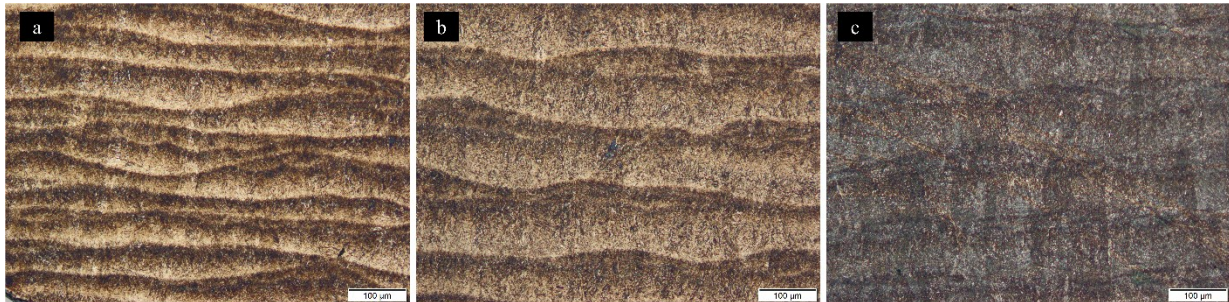


Figure 42: OM micrograph samples post-etching. a) sample treated at 200°C for 10 hours; b) sample treated at 300°C for 10 hours; c) sample treated at 400°C for 10 hours.

Microstructure was examined at high magnifications with SEM (Figure 43). The samples treated at 200°C and 300°C (Figure 43.a and Figure 43.c) exhibited intercellular segregations thinner compared to those within the as-built sample (Figure 39). Additionally, protrusions are visible in Figure 43.b and Figure 43.d for these two samples. Instead, the sample treated at 400°C showed defined intercellular segregations and carbide precipitation in the martensitic laths (Figure 43.e and Figure 43.f).



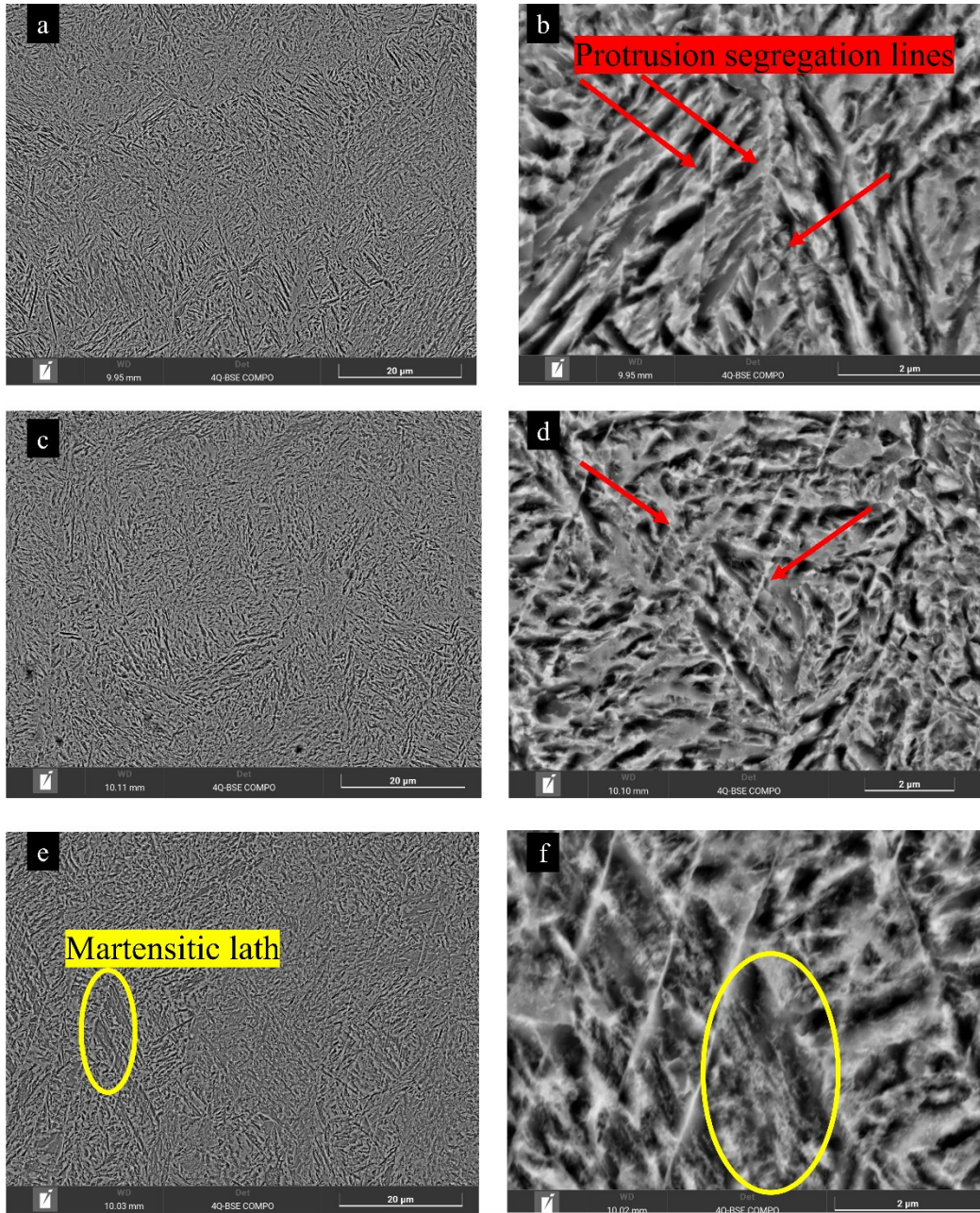


Figure 43: SEM micrographs of 10 hours isothermal treated samples at magnification of 20  $\mu\text{m}$  and 2  $\mu\text{m}$  in scale from left to right. a) and b) samples treated at 200°C; c) and d) sample treated at 300°C; e) and f) sample treated at 400°C.

#### 4.1.3 Macro-hardness

Macro hardness tests were conducted on the heat-treated samples, including those treated for both 5- and 10- hours treated ones. Each test produced results with minimal standard deviation, suggesting macro-homogeneity in terms of hardness across the microstructure. Table 7 reports average macro hardness values and their standard deviation for each sample. Samples treated at 200°C and 300°C displayed comparable hardness, while those treated at 400°C exhibited a decrease. In Figure 44, the



graph compares the results of the as-built and heat-treated samples. samples treated at 200°C and 300°C exhibited higher hardness compared to the as-built one.

Temperature treatment	5 hours treatment (HV5)	10 hours treatments (HV5)
200°C	581,3 ± 9,2	586,33 ± 7,76
300°C	577,8 ± 3,0	584,33 ± 4,13
400°C	509,7 ± 5,6	506,67 ± 7,66

Table 7: Macro hardness value in HV and their standard deviation of the isothermal treated samples.

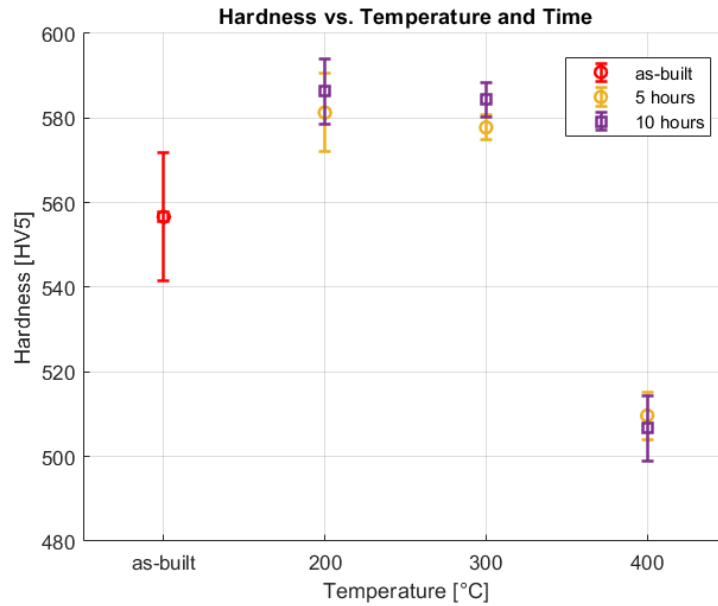


Figure 44: Hardness vs. Temperature and time graphs. The hardness is in HV5.

## 4.2 Wear tests

### 4.2.1 Room Temperature

#### 4.2.1.1 Pin-on-disc tests

The CoF recorded during the test at room temperature (RT1500) shows an overall steady-state regime, as no cyclical stages are present (Figure 45.a) The average CoF is 0,832. Figure 45.b shows a zoom of the first 100 m. During this initial stage, the CoF increased rapidly up to a value of 0.8, followed by a drop until 0,6. Then, it increases again up to a value close to 0.7 and subsequently it decreases smoothly to stabilize at a value of about 0,58.

According to the analysis of the CoF from RT1500, two interrupted tests were conducted: one after the first drop (RT18) and one before the final stabilization (RT65) as indicated by the red arrows in Figure 45.b. The CoF graphs of the two interrupted tests are respectively presented in Figure 45.c and Figure 45.d, showing a similar trend to that of the RT1500 test (Figure 45.e).

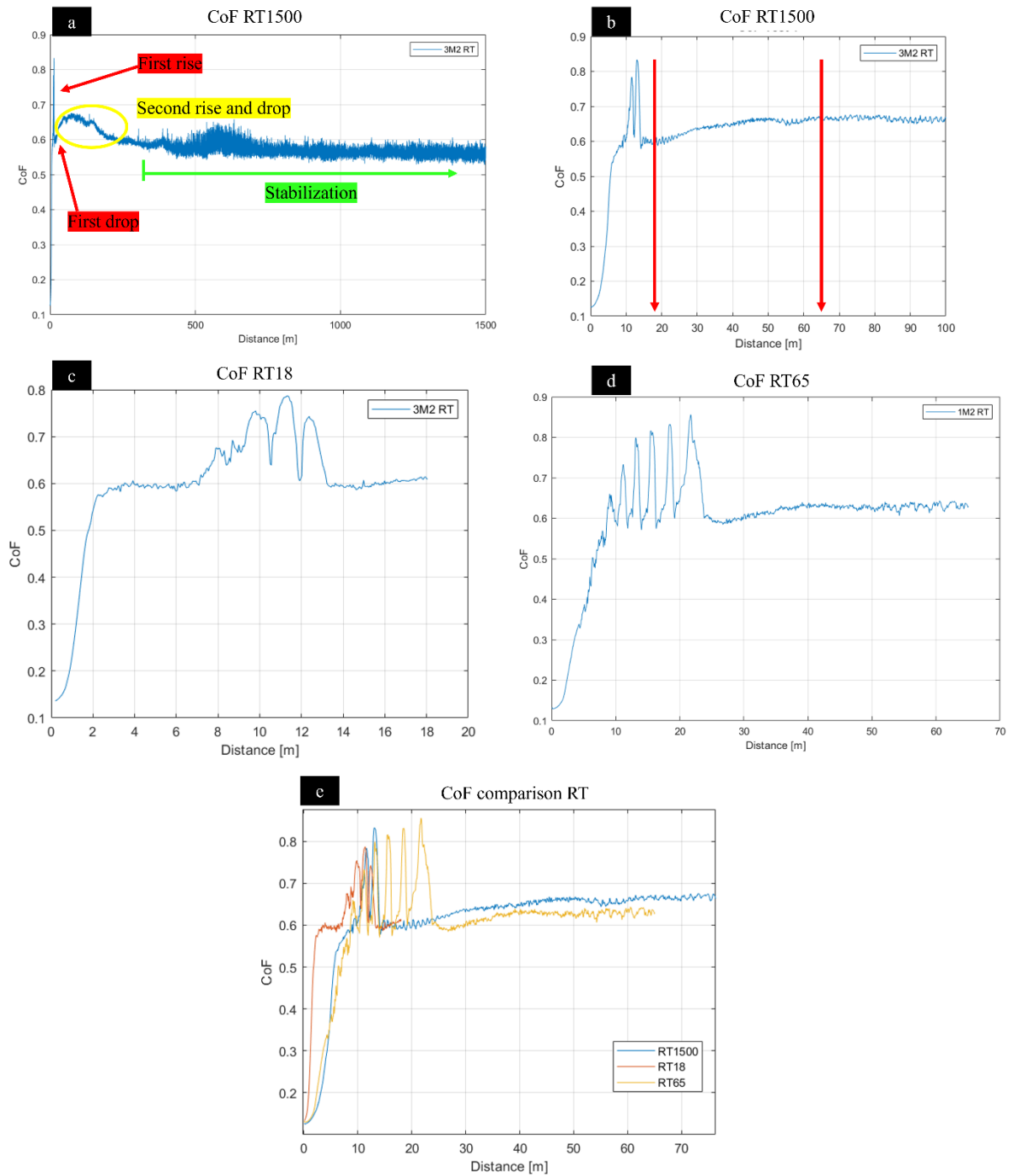


Figure 45: Graphs of Coefficient of Friction test at Room Temperature. a) entire CoF of RT1500; b) zoom of the CoF of RT1500 Test, red lines indicate where was to interrupt subsequent tests; c) graph of CoF of RT18 Test; d) graph of CoF RT65 Test; e) a zoom of the comparison of the CoF of the three tests.

#### 4.2.1.2 Profilometer measurement

Using the profilometer (Figure 34), measurements of the width of the worn tracks and the worn volume were conducted (Table 8). The wear rate was obtained by dividing the worn volume by the sliding distance. The worn volume increases with the increase of the sliding distance, due to the

increase of both the depth and width of the worn track. It is evident that as the distance increases, the wear rate decreases (Figure 46).

	Distance [m]	Worn volume [mm <sup>3</sup> ]	Wear rate [mm <sup>3</sup> /mm]	Width [μm]
RT18	18,05	0,073	$4,040 \cdot 10^{-3}$	145,87
RT65	65,04	0,102	$1,157 \cdot 10^{-3}$	257,42
RT1500	1500	0,44	$0,293 \cdot 10^{-3}$	487,88

Table 8: Worn volume and width collected by profilometer measurement. Wear rate is the ratio between worn volume and total distance of the test.

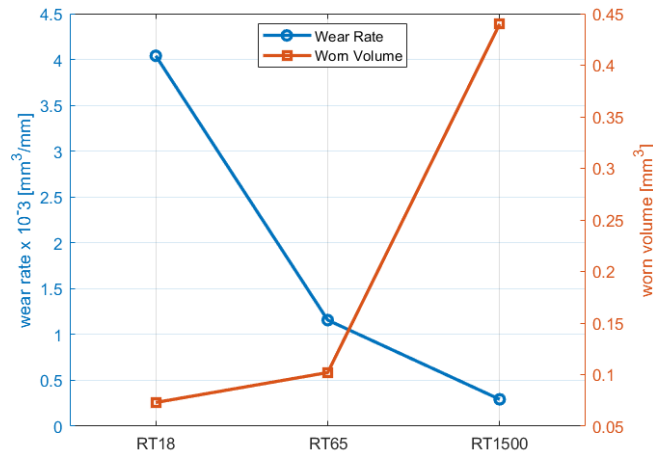


Figure 46: Wear rate (blue) and worn volume (orange) comparison for the three RT tests.

The increase in depth is visible in the profilometer of the track, taken using the same range settings (Figure 47).

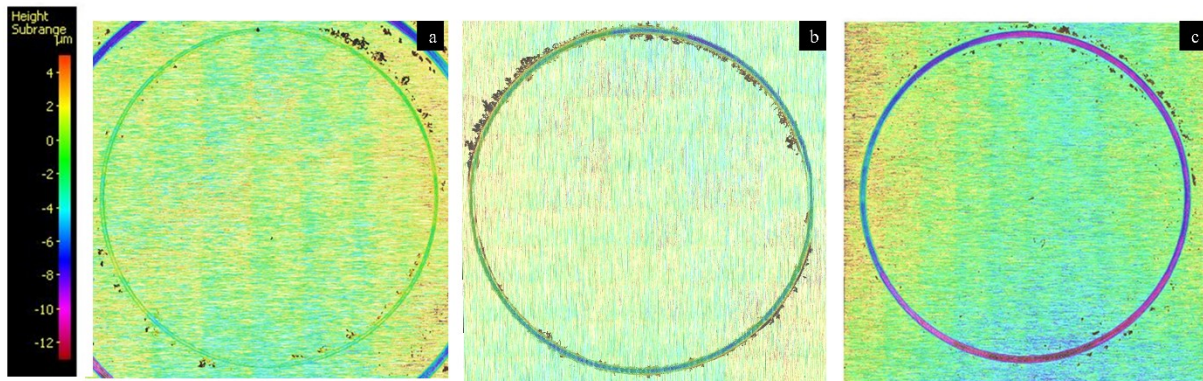


Figure 47: Profilometer photos of the wear tracks. On the left, the height scale at which the photos were done is reported. a) wear track RT18 test; b) wear track RT65; c) wear track RT1500 test.

The worn volume of the counter-body after each test was also examined. After the two interrupted tests, the worn volume is negligible. In contrast, after the RT1500, the worn distance was 10,5μm. The dimensions of the worn area were 585,5 μm x 453,6 μm (Figure 48), considering L1 the wear length perpendicular to the sliding direction while L2 the parallel one.

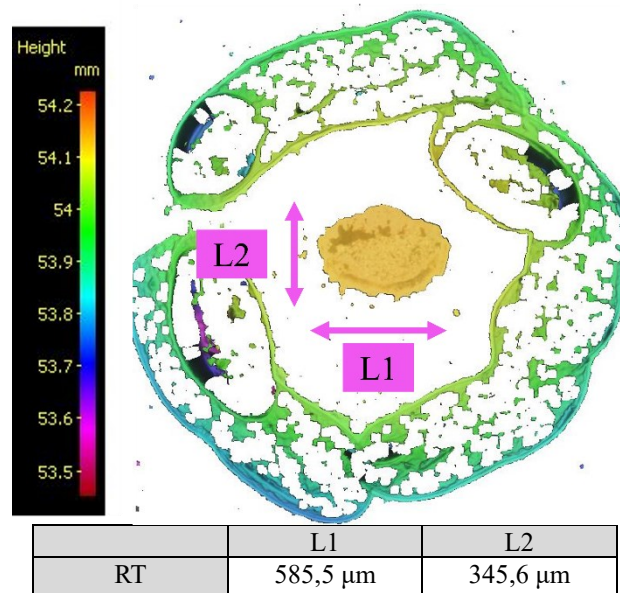


Figure 48: Alumina counter-body photo and size of worn. The range was maintained constant for every examination.

#### 4.2.1.3 Microscope Observation of Worn Track

Worn tracks were investigated both using SEM and OM, and the results are reported in this section in the following order: RT18, RT65, and RT1500.

Micrographs of the RT18 test are displayed in Figure 49 with the red arrows indicating the sliding direction during the test. OM and SEM micrographs of the same position of the track are compared. Rectification lines are still visible, they are not completely worn. Moreover, the track does not appear uniform. Some cracks and zones with different colours are visible, as evident in Figure 49.e and Figure 49.f. Non-uniform grooves are visible in Figure 49.g and Figure 49.h, where plastic deformation of the track occurs, leading to delamination and subsequent creation of grooves and platelets. Grooves are less defined and continuous than the one reported later in RT1500 (Figure 51).

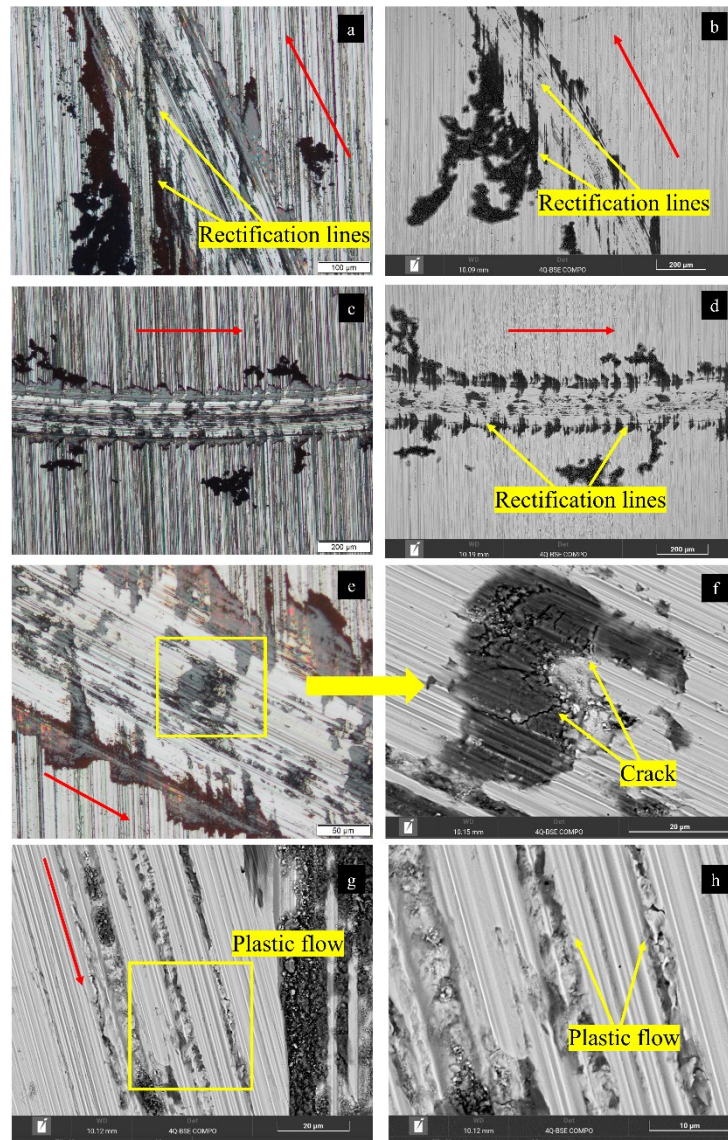


Figure 49: OM (a, c) and SEM (b, d) micrographs of the RT18 test. a) and b) are taken in the same position on the track, as well as c) and d). The red arrows indicate the sliding direction during the wear test; e) and f) show an example of the crack along the wear track; g) and h) show plastic flow and fracture surface where delamination occurs.

The micrographs of the RT65 test are shown in Figure 50 with the red arrows that indicate the sliding direction during the wear test. Rectification lines are still present, they are not completely worn. Debris accumulates preferentially along the rectification lines or are pushed outside the track. debris along the track is compacted by the passage of the counter body. Figure 50.d highlights a zone of detachment from where platelets are created and plastic deformation of the surface of the track.



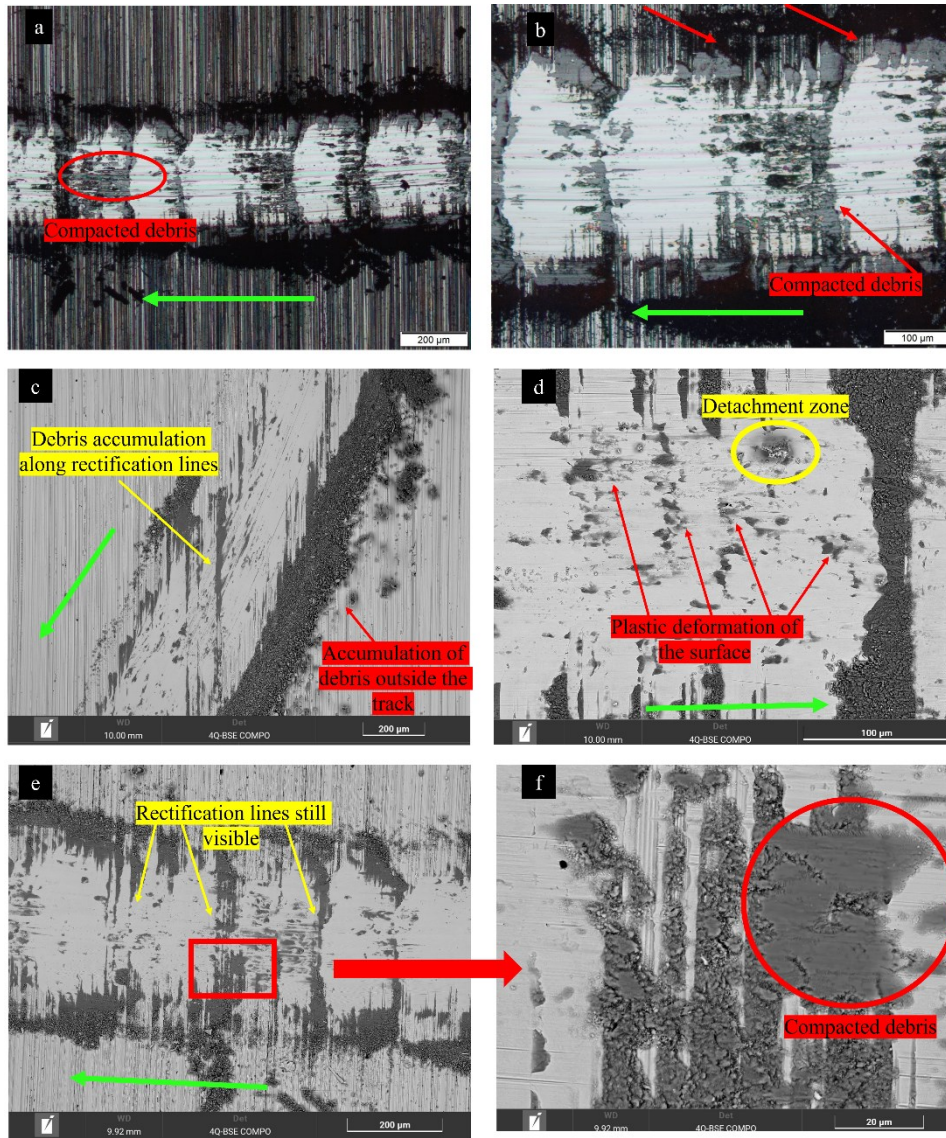


Figure 50: Green arrows indicate the sliding direction during the test. a) and b) OM micrographs of the RT65 test. Compacted debris are highlighted; c) debris accumulation along the rectification lines and outside the track; d) detachment zone and plastic deformation of the surface of the track; e) and f) show debris compacted by the counter-body passage.

The worn surface after the RT1500 test revealed an overall smooth appearance (Figure 51). OM micrographs showed debris accumulation outside the wear track (Figure 51.a and Figure 51.b). However, no significantly big debris or platelets were observed within the track, and the grooves appeared clear and continued along the track. Figure 51.d provided a zoomed-in view of Figure 51.c, where it is evident that only minimal debris was present in the track and preferentially accumulated along the grooves.

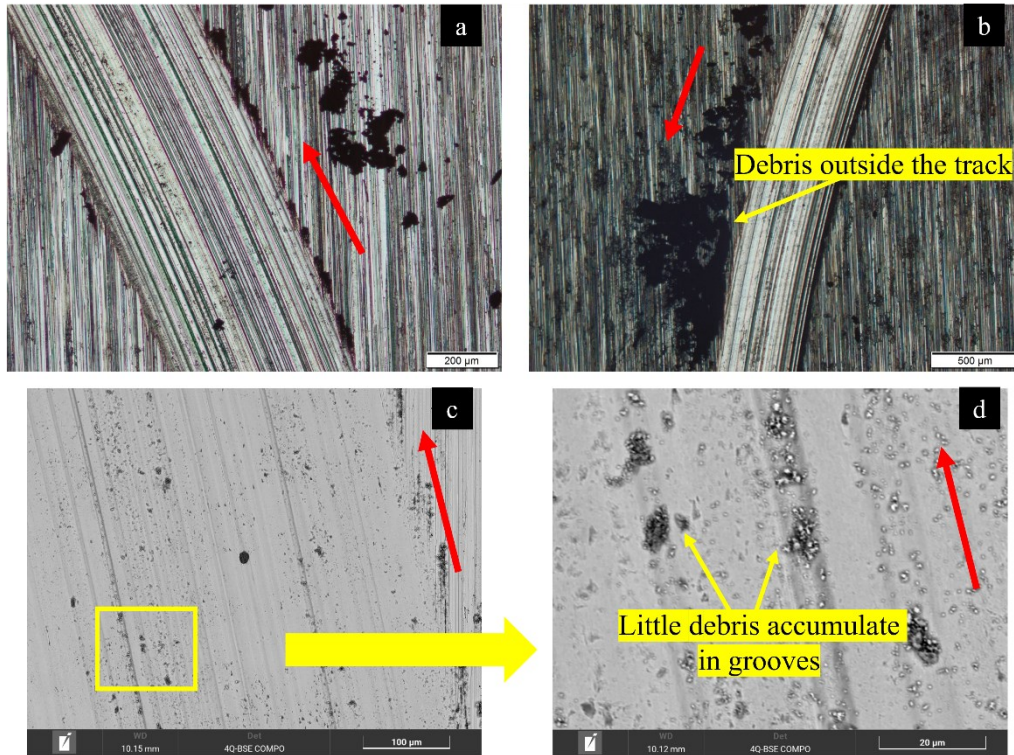


Figure 51: Micrographs of wear tracks of RT1500 test; a) and b) OM micrographs of Track RT1500, c) SEM micrograph and d) a zoom from the yellow rectangle of c) micrograph. The red arrows indicate the sliding direction of the wear tests.

#### 4.2.1.4 Debris characterization

Debris showed different colour for the three RT test. RT18 and RT65 showed black debris (Figure 52.a and Figure 52.b), with more crushed grey debris in RT65. Instead RT1500 showed completely red debris (Figure 52.c).

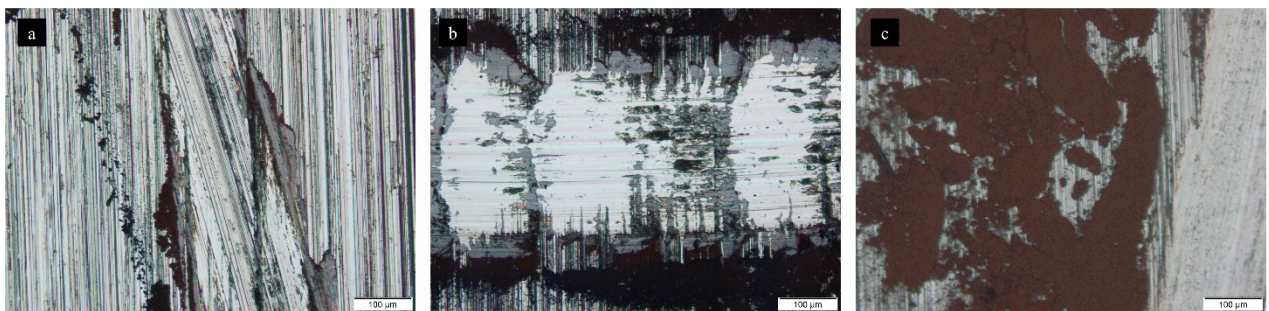


Figure 52: Debris overview of a) RT18; b) RT65 and c) RT1500.

Moreover, each test revealed different types and sizes of debris, suggesting an evolutionary process in their formation. In the RT18 test, some large platelets were detected (Figure 53.a) that were not present in the other. In the other tests, debris was found either crushed and compacted along the track (Figure 53.b) or as large, crushed fragments-debris far from the track (Figure 53.c). This analysis suggests an evolution of the platelet debris evolves over time. Initially, platelets form from detachment zones (Figure 50.d). They then have two possible paths: they can either be pushed away



from the track or remain along it. If they are pushed away, they stay large, between 6  $\mu\text{m}$  and 15  $\mu\text{m}$  (Figure 53.c and purple part of Figure 53.d). If they remain in the track, they are crushed by the passage of the counter-body, reducing in size (less than 2  $\mu\text{m}$ ) and becoming powder-like debris (Figure 53.b and light-blue part Figure 53.d).

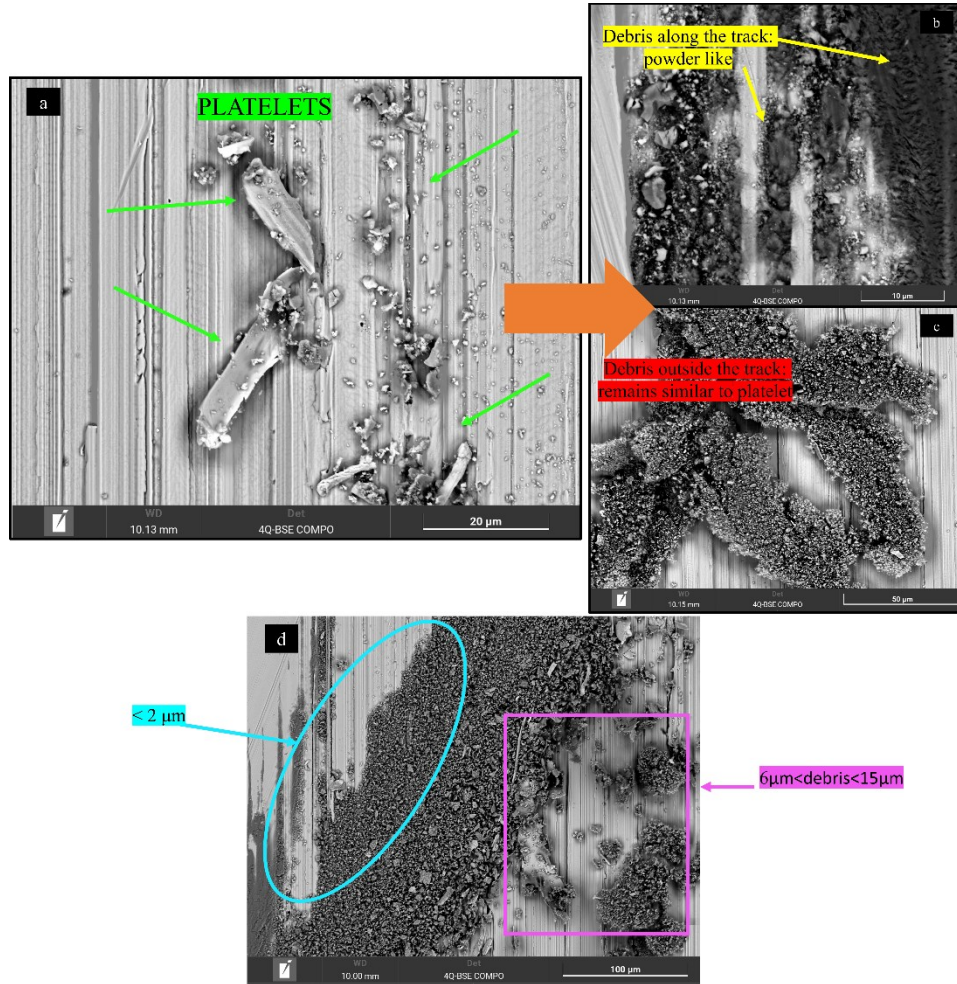


Figure 53: a) big platelets outside the track in the RT18 test; b) compacted debris along the track, RT65; c) crushed debris outside the track, RT1500; d) different sizes of the debris with respect to the distance from the track.

In the extended RT1500 test, SEM analysis showed that the debris is entirely crushed (Figure 54, taken in the same position of Figure 52.c).



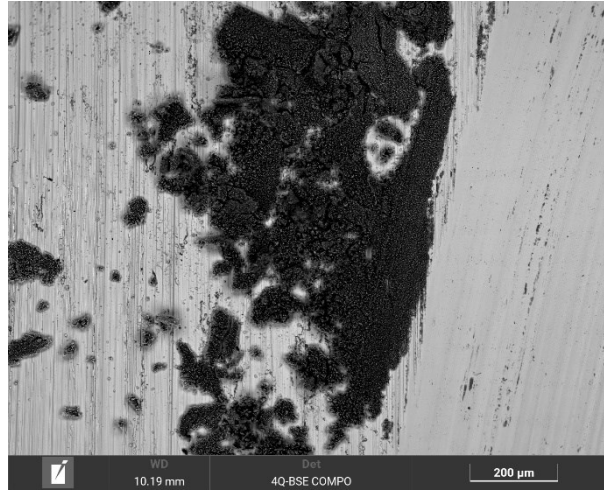


Figure 54: Crushed debris of the RT1500 wear test. The micrograph is taken in the same position as Figure 52.c one.

Additionally, the chemical composition of the debris was analysed through EDS analyses at SEM. In the RT18 test (Table 9), platelets debris did not show signs of oxidation, unlike compacted debris. The same consideration can be made for the chemical composition of the RT65 test (Table 10). In the RT1500 test, all the debris exhibited oxidation, with no significant presence of aluminium from the counter-body (Table 11). In this case, only crushed debris was analysed because no big flakes-like debris were detected after 1500 m of sliding. Some aluminium was detected but not in significant amounts.

	C	O	Al	Si	Mn	Fe	Mo
Platelets	$4,3 \pm 1,8$	$3,49 \pm 1,2$	$0,04 \pm 0,02$	$1,53 \pm 0,4$	$0,48 \pm 0,2$	$89,82 \pm 0,05$	$0,25 \pm 0,04$
Debris	$3,13 \pm 1,4$	$47,65 \pm 3,2$	$1,31 \pm 0,15$	$1,03 \pm 0,09$	$0,317 \pm 0,07$	$46,4 \pm 4,3$	$0,16 \pm 0,03$

Table 9: Atomic composition of platelets and debris from RT18.

	C	O	Al	Si	Mn	Fe	Mo
Platelets	$7,38 \pm 4,8$	$15,53 \pm 8,43$	$1,21 \pm 1,06$	$1,2 \pm 0,4$	$0,37 \pm 0,07$	$74,12 \pm 9,8$	$0,18 \pm 0,04$
Debris	$0,84 \pm 0,75$	$60,57 \pm 1,33$	$0,14 \pm 0,03$	$0,92 \pm 0,03$	$0,21 \pm 0,02$	$37,22 \pm 0,83$	$0,1 \pm 0,04$

Table 10: Atomic composition of platelets and debris, RT65.

C	O	Al	Si	Mn	Fe	Mo
$3,2 \pm 0,1$	$40,2 \pm 1,2$	$0,1 \pm 0,02$	$0,8 \pm 0,005$	$0,37 \pm 0,01$	$55,0 \pm 1,03$	$0,26 \pm 0,3$

Table 11: Atomic composition of debris, RT1500.

#### 4.2.1.5 Subsurface modifications

Observations of the subsurface of the wear track were carried out on the sample from the RT1500 test (Figure 55). Along the track is possible to notice a layer called Mechanical Mixed Layer (MML) of 1  $\mu\text{m}$  in height, formed by the crushed debris. A plastic deformed layer (PDL) of 2-3  $\mu\text{m}$  was found underneath the MML due to the deformation and curvature of the martensite laths and of the segregation lines.

After conducting the wear tests, nano-indentation analyses were carried out on the subsurface of the track. The primary objective was to identify and study any microstructural changes attributable to wear. The affected area exhibiting reduced hardness was highest (16  $\mu\text{m}$ ) in size compared to the PDL layer.

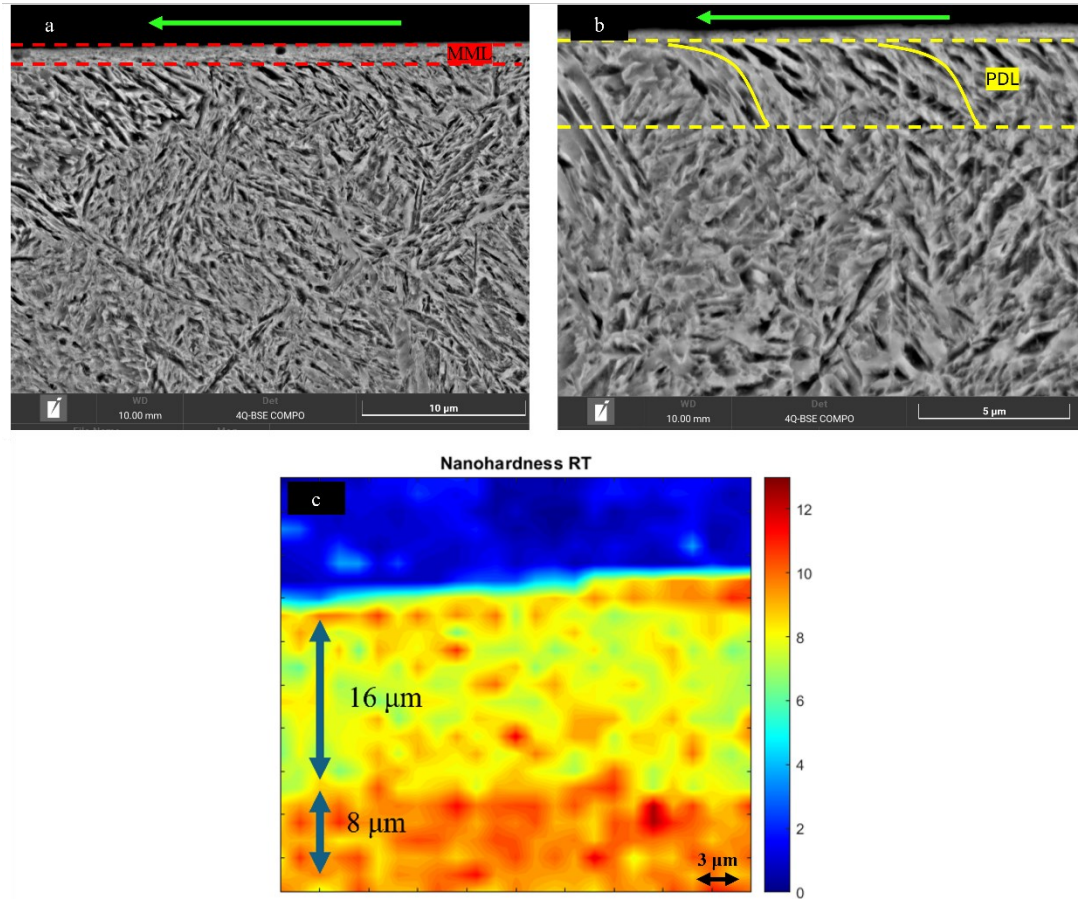


Figure 55: a) and b) subsurface micrographs of RT1500 test. The green arrows indicate the sliding direction of the wear test. Mechanical mixed layer (MML) and plastic deformed layer (PDL) are highlighted; c) nano hardness grid of subsurface sample (RT1500). The blue part is the resin (Bakelite). The reported scale is in GPa.

## 4.2.2 High Temperature

### 4.2.2.1 Pin-on-disc tests

Three tests at high temperatures were performed with the same parameters as the room temperature wear test (4.2.1). The tests were performed at 200°C (HT200), 300°C (HT300) and 400°C (HT400). The surface of the samples looked coloured after the tests due to the tempering effect, as is possible to see in Figure 56 where a picture of all the samples was taken immediately after the tests. In Figure 56.d [81], a chart displaying the colours of tempering steels is reported. Indeed, as it will be better explained (Section 5.3), the high temperature pin-on-disc tests can be considered as a tempering heat treatment due to their long time (more than 4 hours).

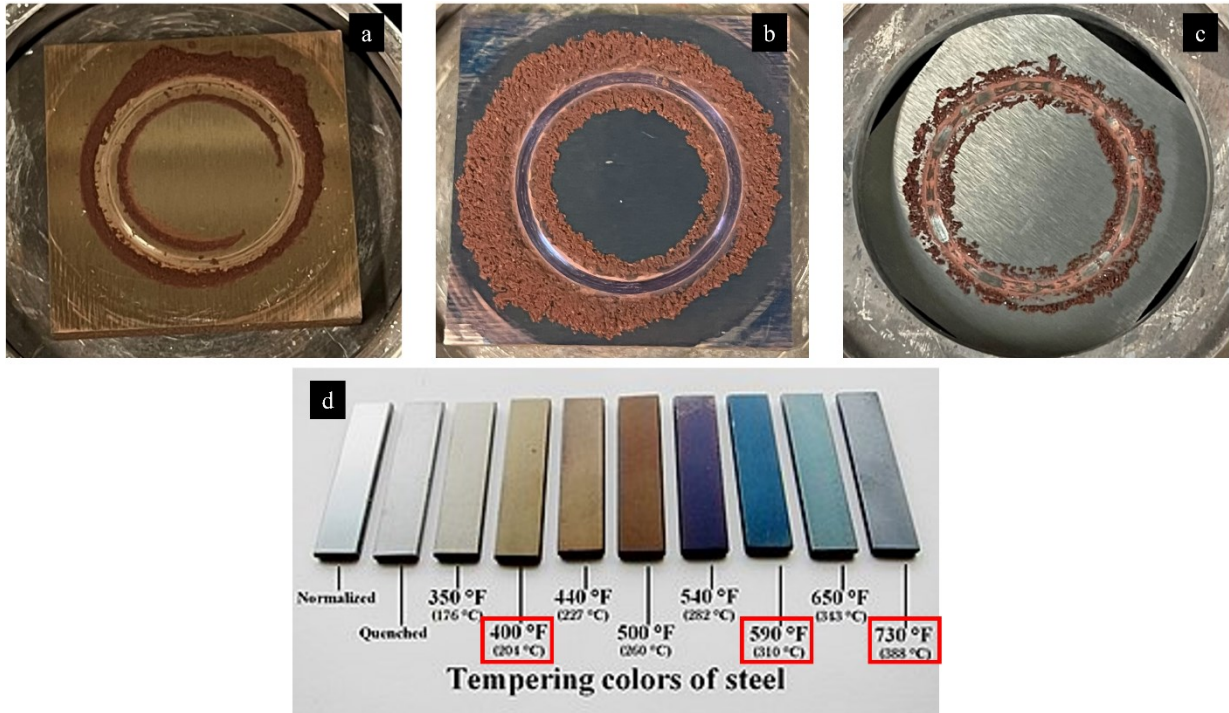


Figure 56: a) wear test at 200°C, showed yellow; b) wear test at 300°C, showed blue; c) wear test at 400°C showed grey; d) tempering steel chart is reported with a highlight on the three temperatures of the wear tests that are consistent with the results[81].

For ease of description, CoF evolution is only shown from 0 until 55 m of sliding distance (Figure 57). This evolution is a representation of the entire CoF recorded during the long test until 1500 m. The typical evolution as the one of RT is not present for the HT tests. Furthermore, the average CoF is different, with the one of HT400 having the lowest value.

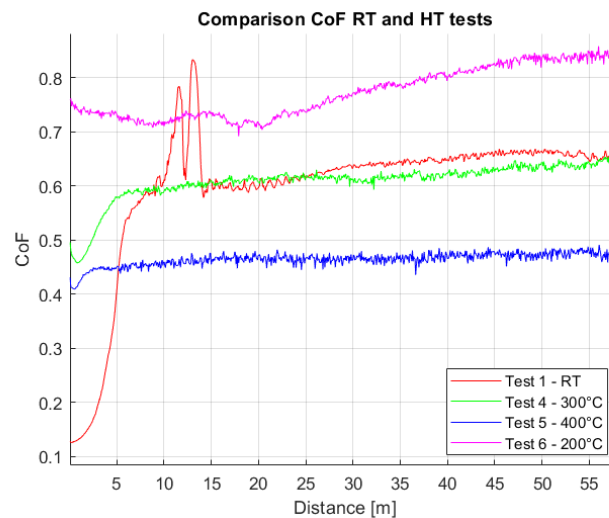


Figure 57: Comparison between Coefficient of Friction of RT and HT tests.

#### 4.2.2.2 Profilometer measurement

As in the previous section (4.2.1.2), profilometer photos taken at the same height range are reported in Figure 58. The track of the test HT300 has the highest worn volume, with an average depth of 65,7  $\mu\text{m}$ . The morphology of the worn track of both HT200 and HT300 is regular, whereas it is non-uniform for HT400. The latter worn track also exhibits a lower worn volume, as a results of a lower depth. In Table 12 detailed data about the width, the worn volume, and the wear rate of the HT tests are reported, in Figure 59 worn volume and wear rate of the HT tests are compared with those of the RT1500 test.

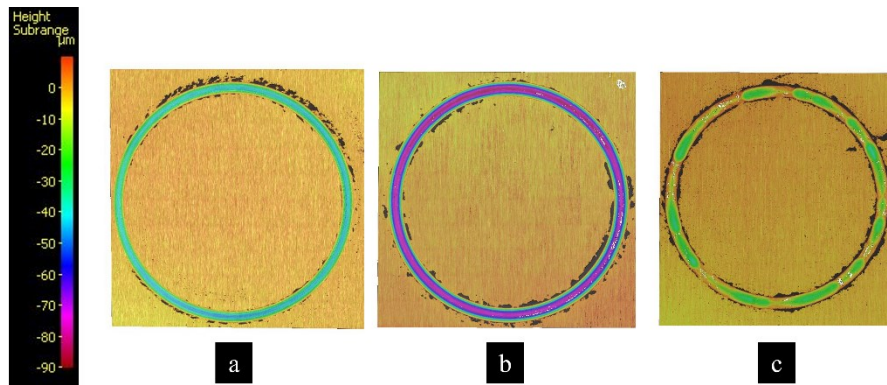


Figure 58: Profilometer photos taken at the same range, reported on the left. a) HT200 test; b) HT300 test and c) HT400 test.

	Depth [ $\mu\text{m}$ ]	Worn volume [ $\text{mm}^3$ ]	Wear rate [ $\text{mm}^3/\text{mm}$ ]	Width [ $\mu\text{m}$ ]
HT200	$32,9 \pm 2,36$	2,261	$1,488 * 10^{-3}$	974,88
HT300	$65,7 \pm 3,6$	4,726	$3,109 * 10^{-3}$	1334
HT400	$13,7 \pm 8,3$	1,212	$0,797 * 10^{-3}$	1168

Table 12: Depth, worn volume and width from profilometer analysis. Wear rate is calculated as the ratio between worn volume and total distance.

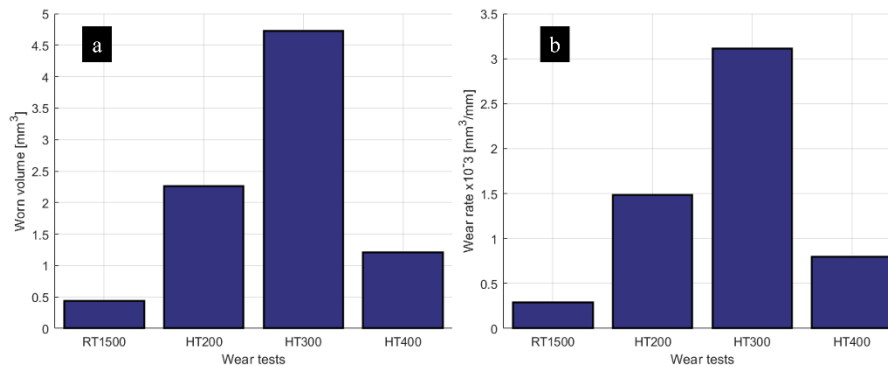


Figure 59: a) Worn volume and b) wear rate comparison of the four long tests.

The most worn counter-body was the one of the HT400 test (Figure 60), the wear height had a value between 33,4  $\mu\text{m}$  of minimum and 4,1  $\mu\text{m}$  of maximum. The others worn distance were negligible. More in general, L1 for HT test results are higher than the one at RT. L1 and L2, as previously explained in section 4.2.1.2, are respectively the wear length of the counter body perpendicular and parallel to the sliding direction.

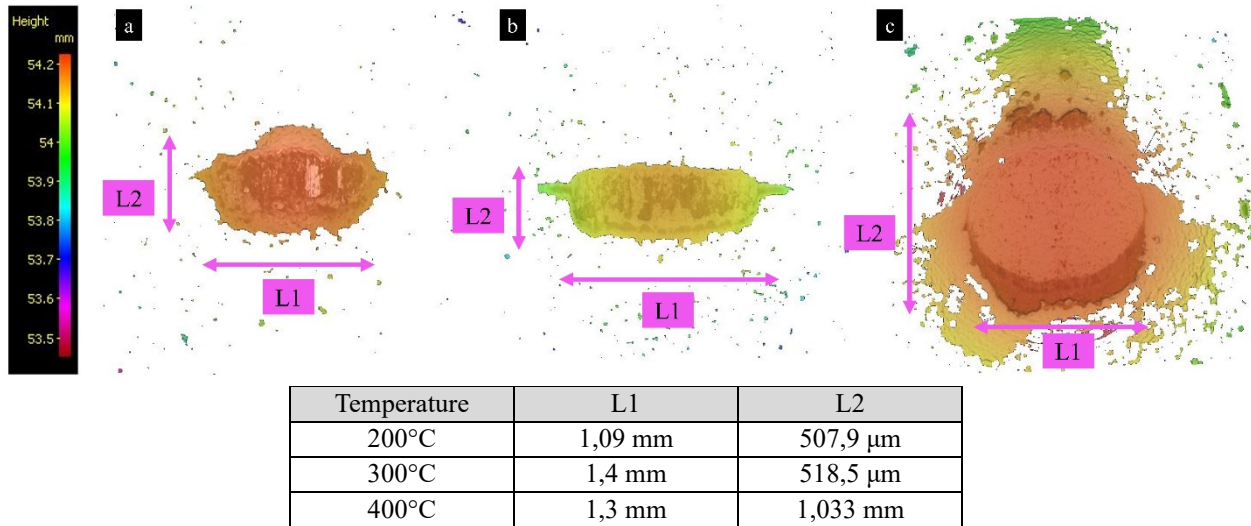


Figure 60: Profilometer photo and data of sizes of HT tests with the range on the left, the same as RT measurement. a) HT200 test; b) HT300 test and c) HT400 test.

#### 4.2.2.3 Microscope observation of Worn Track

Worn tracks were investigated both at SEM and OM after the wear test.

The HT200 test (Figure 61) showed a pale yellow-coloured surface, according to the tempering effect (Figure 56). The track displayed numerous small debris particles, primarily concentrated along the grooves and on delaminated areas (Figure 61.a, Figure 61.b and Figure 61.c). Additionally, detachment from the track was detected (Figure 61.d).



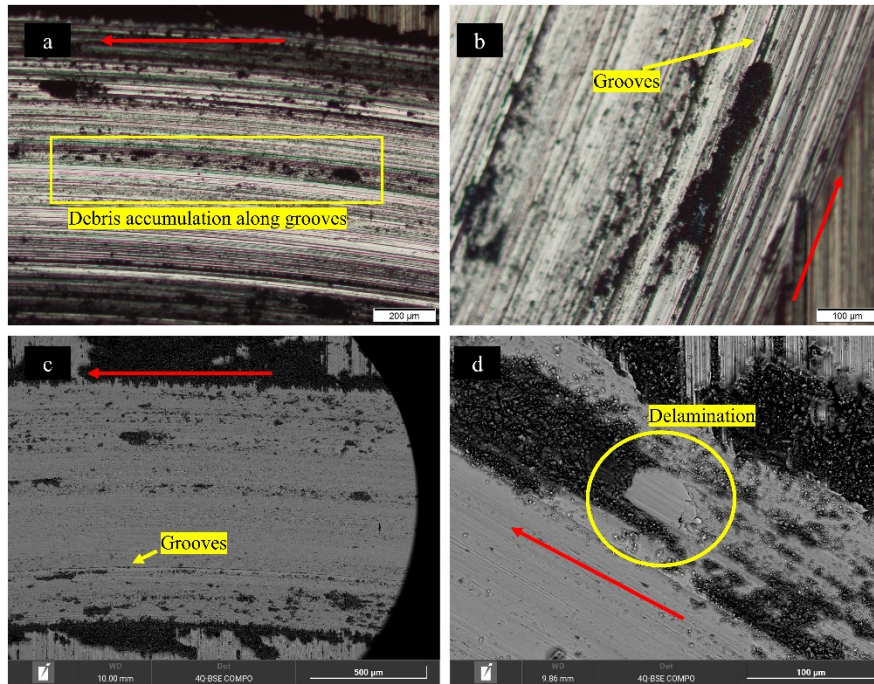


Figure 61: Micrographs wear track HT200 test. a) and b) OM micrographs show the pale yellow surface and the debris along the track; c) SEM photo taken in the same place of a) shows the surface; d) SEM zoom on the detachment along the track.

The HT300 test shows a blue-pink-purple colour of the surface (Figure 62.a), due to the tempering effect and the oxidation. The surface itself was smooth (Figure 62.c), with similar characteristics to that of the test HT200. Delamination (Figure 62.b and Figure 62.d) was detected. Debris accumulated preferentially along the grooves and on delaminated areas (Figure 62.e).

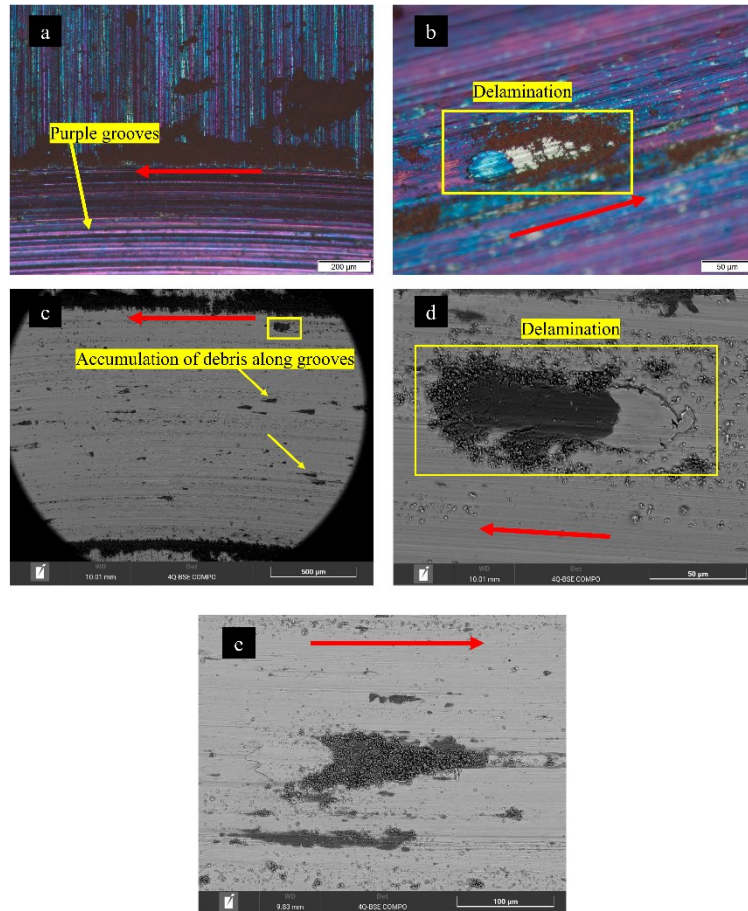


Figure 62: Micrographs of HT300 test with red arrows indicating sliding direction. a) OM micrograph shows the pink-blue-purple colour of the sample; b) OM micrograph shows platelets detachment; c) SEM micrograph shows the clean track; d) SEM micrograph of platelets detachment; e) SEM micrograph shows the accumulation of the debris at the start of groove.

The HT400 test (Figure 63) showed that the track's width was continuously changing along the circle. Some parts appear blue due to the oxidation (Figure 63.a a Figure 63.b) in correspondence of the larger part of the width. Furthermore, a compact layer of oxides was detected on the narrower part of the track with some parts that started to delaminate (Figure 63.c and Figure 63.d).

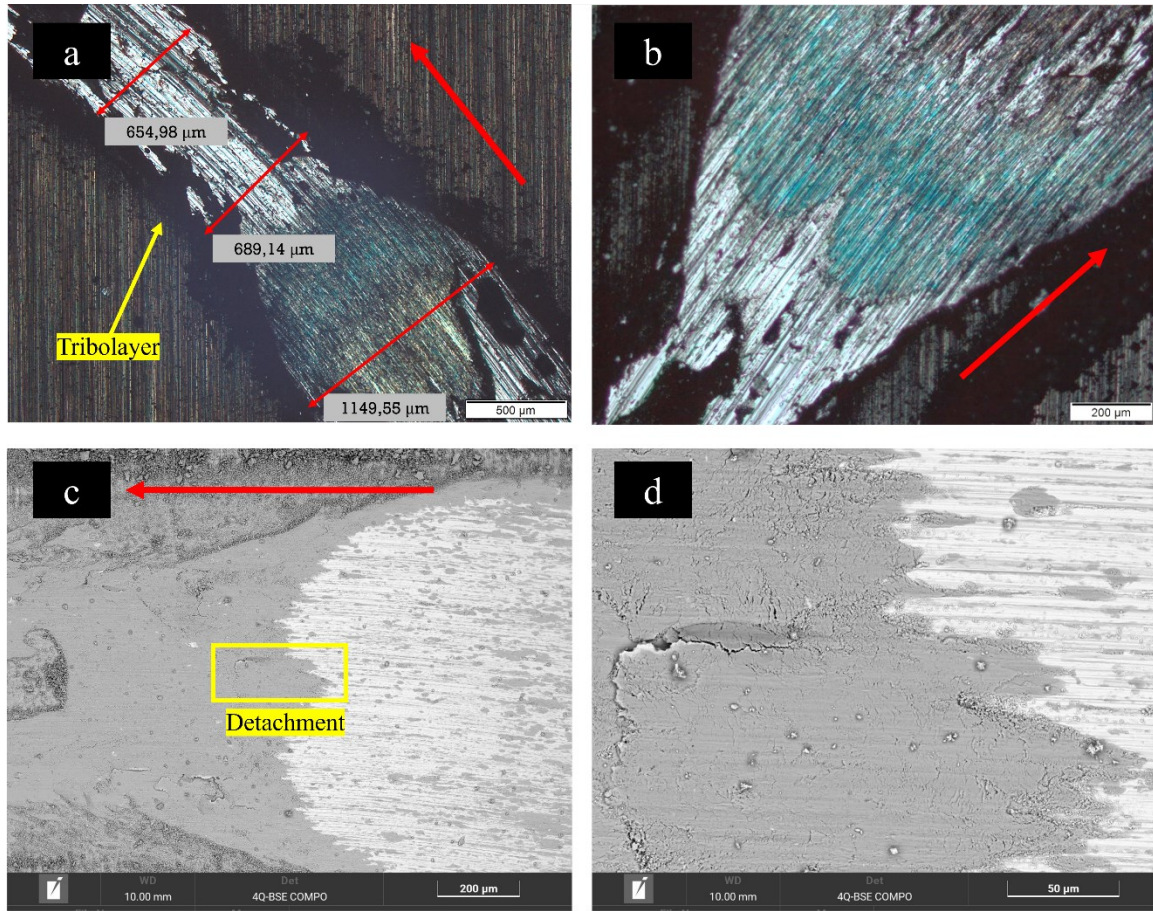


Figure 63: Micrographs HT400 test, red arrows indicate the sliding direction. a) and b) show different parts of the track where the tribolayer is present. c) SEM micrograph of tribolayer and d) zoom of c) where detachment from tribolayer is highlighted.

EDS analysis was used to investigate the atomic compositions of the debris of the three HT tests (Table 13). Aluminium was found in the debris of the HT400 test, the one with the most worn counterbody (Figure 60). Oxygen levels revealed oxidation in all HT tests.

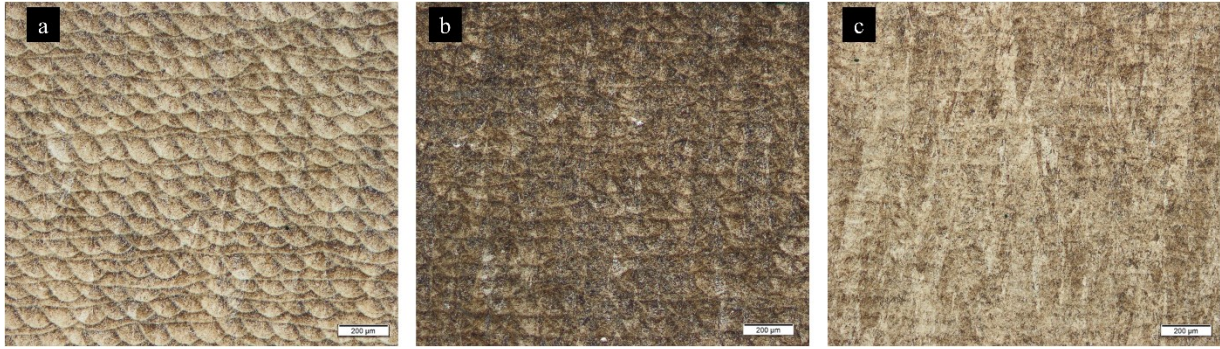
HT	C	O	Al	Si	Mn	Fe	Mo
200	2,74±0,05	61,9±1,15	-	0,76±0,02	0,14±0,01	34,33±1,12	0,12±0
300	1,75±0,44	57,72±6,28	-	0,61±0,6	0,14±0,07	39,34±5,61	0,43±0,41
400	1,32±1,03	58,67±1,96	0,77±0,19	0,82±0,05	0,14±0,03	38,2±2,6	0,09±0,002

Table 13: Atomic composition of the debris of HT wear tests.

#### 4.2.2.4 Subsurface modifications

Subsurface worn tracks were observed after the HT wear tests. OM micrographs (Figure 64) obtained from these tests exhibit different types of microstructures. In the HT200 (Figure 64.a) and HT300 (Figure 64.b), typical melt pools and layers of the LPBF structure are visible, while the HT400 test appeared different and more homogeneous (Figure 64.c).





*Figure 64: OM micrographs of the subsurface of wear tests. a) 200°C; b) 300°C; c) 400°C.*

SEM observations at high magnification were conducted on the subsurface underneath the worn track, parallel to the sliding direction. The SEM micrographs of the HT200 test (Figure 65.a and Figure 65.b) revealed that the track exhibited interrupted oxides with varying heights ranging between 2 and 3  $\mu\text{m}$ . Additionally, a PDL with a minor height of 2  $\mu\text{m}$  was present. The micrographs from the HT300 test (Figure 65.c and Figure 65.d) revealed an oxide layer of approximately 1  $\mu\text{m}$ . Additionally, the analyses have detected the existence of MML and PDL, with a maximum height of 500 nm and 2  $\mu\text{m}$  respectively. The micrographs from the HT400 test (Figure 65.e and Figure 65.f) revealed the presence of an oxide layer of about 5-6  $\mu\text{m}$  and another layer consisting of compacted debris of the oxide layer. The PDL is thicker compared to the other HT tests (5-6  $\mu\text{m}$ ).

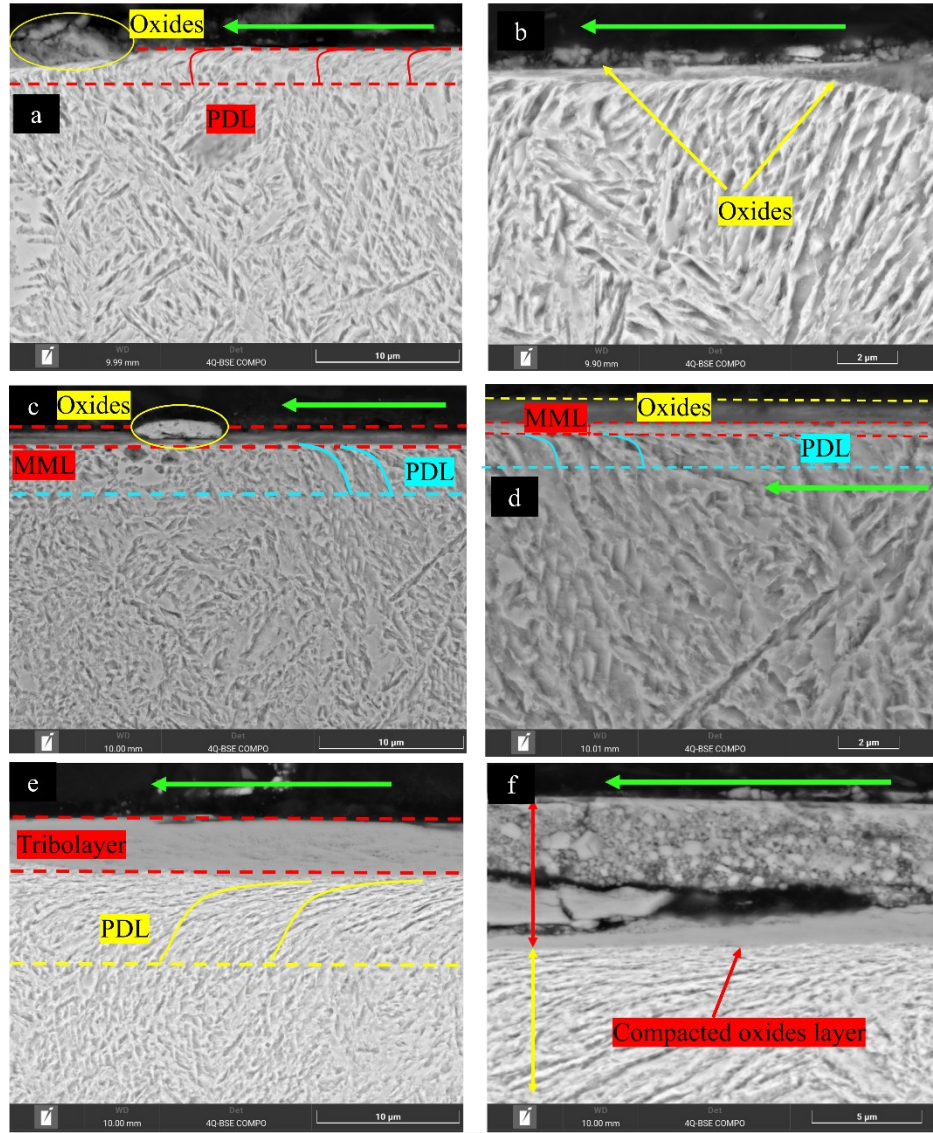


Figure 65: SEM micrograph of the subsurface of the wear track. Green arrows indicate the sliding direction of the wear tests. a) and b) HT200 test; c) and d) HT300 test; e) and f) HT400 test.

#### 4.2.2.5 Hardness

After conducting the wear tests, macro- and nano-indentation analyses were carried out on the cross-section of the sample underneath the worn track. Macro-hardness analysis was conducted to identify hardness changes due to the effect of the temperature during the wear test. The samples that underwent wear temperature tests of 200°C and 300°C exhibit a slight increase in average hardness in comparison to the as-built sample (Section 4.0). On the contrary, the sample exposed to a temperature of 400°C displays a decrease in hardness.

Temperature of test	Average hardness [HV5]
200°C	571,33 ± 7,2
300°C	568,33 ± 12,3
400°C	509,33 ± 6,9

Table 14: average macro-hardness unworn surface.

The average macro-hardness are comparable to the ones of the thermal treatment, as is possible to see in Figure 66.

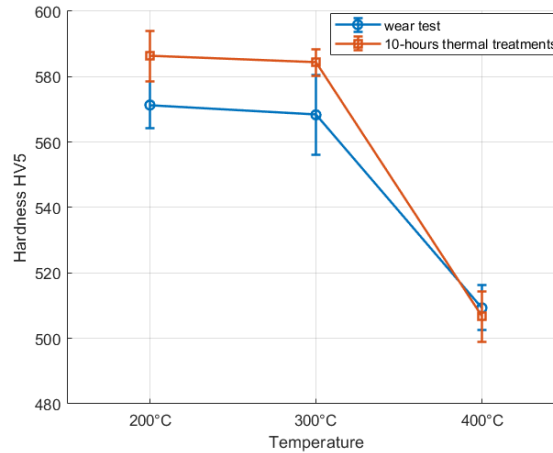


Figure 66: Macro-hardness comparison between HT wear tests and 10-hours thermal treatments.

Nano-hardness grids below the worn track were conducted to identify the hardness of the oxide layer as well as of the MML and PDL (Figure 67). The data obtained from nano-hardness testing may not be accurate, as the height of various layers (such as oxides, MML, PDL) is extremely low (section 4.2.2.4). The distance between different points in nano-indentation was set to 1.5  $\mu\text{m}$ , but some layers can be as low as 500 nm. Therefore, the results shown must be interpreted carefully. The most significant result is the high nano-hardness ( $\sim 20$  GPa) of the oxide layer formed at 400 °C.

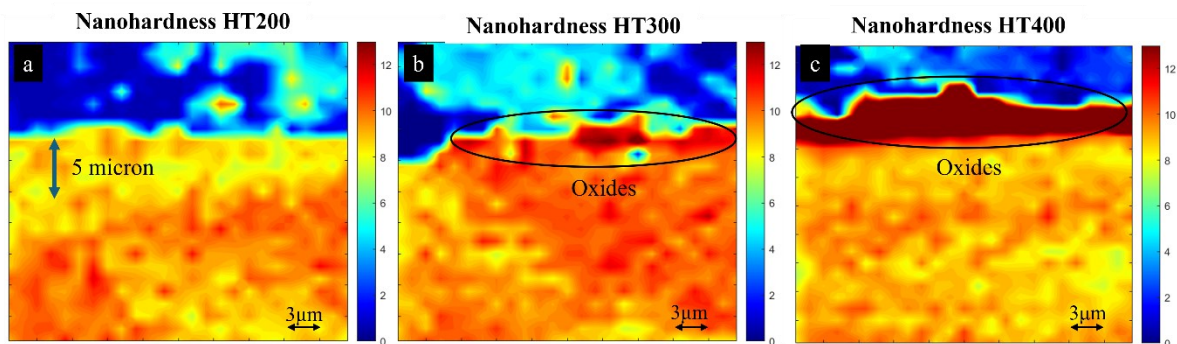


Figure 67: Nano-hardness grid from nano-indentation data. The blue part is bakelite resin. a) 200HT test; b) 300HT test; c) 400HT test

## 5. Discussion

### 5.1 Thermal stability

In this study, DSC analyses were used to investigate the thermal stability of the LPBF AISI S2 tool steel. In particular, isothermal treatments were conducted on different samples for 5 and 10 hours at temperatures of 200°C, 300°C, and 400°C. Subsequently, the samples underwent examinations for hardness and microstructure. The primary objective of these tests was to elucidate the microstructural alterations following the exposure to temperature exceeding ambient conditions. Usually, AISI S2 tool steel produced with conventional methods is employed in applications such as hummers, chisels, or screwdriver bits, thus at room temperature. The work of Gowd reported that AISI S2 exhibits low tool wear when used as a workpiece during a machining operation [82]. However, under certain conditions, an increase in the temperature of the workpiece can shorten the tool's life in view of accelerated wear phenomena due to microstructural changes. Hence, understanding its thermal stability is crucial as it helps predict changes that may occur during wear tests at high temperatures, provided that the thermal effects are well understood.

As delineated in section 4.1, microstructural analyses revealed discernible modifications after thermal treatments. Notably, samples subjected to 5- and 10- hours treatments exhibited comparable macro-hardness values (Table 7), implying that similar microstructures were obtained. The effects of the heat treatments can be divided into two groups, the first refers to samples treated at 200°C and 300°C, whereas the second group regards samples treated at 400°C.

The samples of the first group (heat treated up to 300°C) unveiled the presence of melt pools and HAZs under OM (Figure 42.b and Figure 42.d), similar to the as-built microstructure. Therefore, the microstructure after heat treatments up to 300 °C is still composed of tempered martensite and bainite. In contrast, the intercellular segregations were affected by the heat treatments. These observations can be related to the fact that melt pool “boundaries” are more thermally stable than the cellular structure [83]. In the as-built state, such segregations appear as continuous lines (Figure 38) with a certain thickness (section 4.0). After heat treatments at 200 and 300 °C, such segregations are thinner, and protrusions are visible (Figure 43.b and Figure 43.d) These protrusions may stem from diverse factors, including the growth of bainitic ferrite from the initial martensite laths after its isothermal treatment under  $M_s$ -temperature [84]. Another possible factor may be the thermally activated movements of elements previously segregated in lines or cellular walls [85] during dendrite

growths [86]. These elements may precipitate as elongated carbide [87]. In particular, dissolution can occur [28, 35, 72].

A significant effect of the heat treatments at 200 and 300 °C is the increase in macro-hardness compared to the as-built state, contrary to the conventional trend wherein hardness typically diminishes with increasing tempering temperatures [13, 14]. This anomaly at 200°C and 300°C may be attributed to a strain hardening effect attributable to low-temperature tempering (LTT) [13, 15]. Literature sources [68, 71, 72] suggest that such strain-hardening is thermally activated by the movement of dislocations, a phenomenon intrinsically linked to the high dislocation density engendered during martensitic formation [91]. Regrettably, this study did not delve into experiments about dislocation mobility since instruments with higher magnifications would have been necessary, for example, Transmission Electron Microscopy (TEM) [86]. The increase in hardness can also be attributable to a relatively high presence of silicon (1.2 wt. %). Silicon has the effect of retarding the softening of the tool steel during tempering [92], usually referred to as tempered martensite embrittlement (TME). This mechanism involves the precipitation of cementite within martensitic laths. Notably, silicon inhibits the growth of cementite (characteristic of the third stage of tempering), retarding the precipitation of epsilon carbide and its conversion [93], typically encountered during the initial tempering [94] and LTT [89].

In contrast, samples treated at 400°C exhibited a decrease in hardness compared to the as-built state, attributed to a higher sensitivity to tempering at this temperature. In the OM micrograph of the 400°C treated sample (Figure 42.c), the morphology of HAZs and melt pools appear less defined, and the microstructure is more homogenous. This homogenization may be related to the dissolution of some microstructural phases (e.g. bainite), a phenomenon that occurs following an adequate thermal treatment [14, 25, 40]. In addition, fine carbides were observed to precipitate in martensitic laths (Figure 43.f), a typical effect of tempering treatments.

In summary, samples treated at 200°C and 300°C exhibited similar characteristics, evincing enhanced average hardness relative to the as-built sample. This increase in hardness may be attributed to different factors, including the Si-effect or thermally activated dislocation movements. Macroscopically, the microstructures remained similar to the as-built sample, with heat-affected zones (HAZs) and melt pools discernible. At higher magnifications, certain protrusions of the segregation lines were evident, indicative of augmented mobility of various elements. Conversely, samples treated at 400°C were markedly different, characterized by lower hardness due to a higher

tempering effect and a more homogeneous microstructure. In conclusion, AISI S2 steel evinces thermal stability up to 300°C, while significant modifications occur at 400°C.

## 5.2 Elucidation of wear sequence at room temperature

Understanding the wear behaviour of the LPBF-printed AISI S2 material is one of the main aims of this research. Wear tests at different sliding distances were conducted, using the interrupted approach previously developed by the MMS team [25, 78]. This approach involves initially conducting an extensive test to serve as a reference. Upon completing the full test, in this case, up to 1500 meters, the variations in the CoF graph are analyzed to determine where interrupted tests should be performed. These interrupted tests are intended to better understand specific variations and investigate the underlying microscopic phenomena occurring at those points. Combining results obtained with pin-on-disc, profilometer measurements, as well as OM and SEM observations allowed to elucidate the wear sequence at room temperature.

Three principal changes of interest were identified in the CoF evolution recorded during the RT1500 test (Figure 45.a). The first change occurs during the initial laps of the wear test, corresponding to the run-in period [96] (Figure 45.c). This period was investigated with the first interrupted test (RT18). The elevated value of wear rate (Figure 45.c) obtained after this first test (RT18) is attributed to severe abrasive wear [97]. This mechanism occurs during the early stages of the wear test due to a high roughness of the surface. The plastic deformation of the surface (Figure 49.g and Figure 49.h) is induced by the pressure exerted by the counter body. This plastic flow can deform the surface to the extent that cracks may appear (Figure 49.f), from which platelets can detach from the track (Figure 53.a) through fatigue wear [98]. This detachment could be the cause of the fluctuation observed in the CoF [98]. The detachment of platelets creates a depression in a specific area of the track, leading to the formation of grooves along the entire track. This phenomenon of platelet formation has been extensively studied and is well-known as “delamination theory” [99]. A schematic sketch of the phenomenon’s steps is shown in Figure 68.



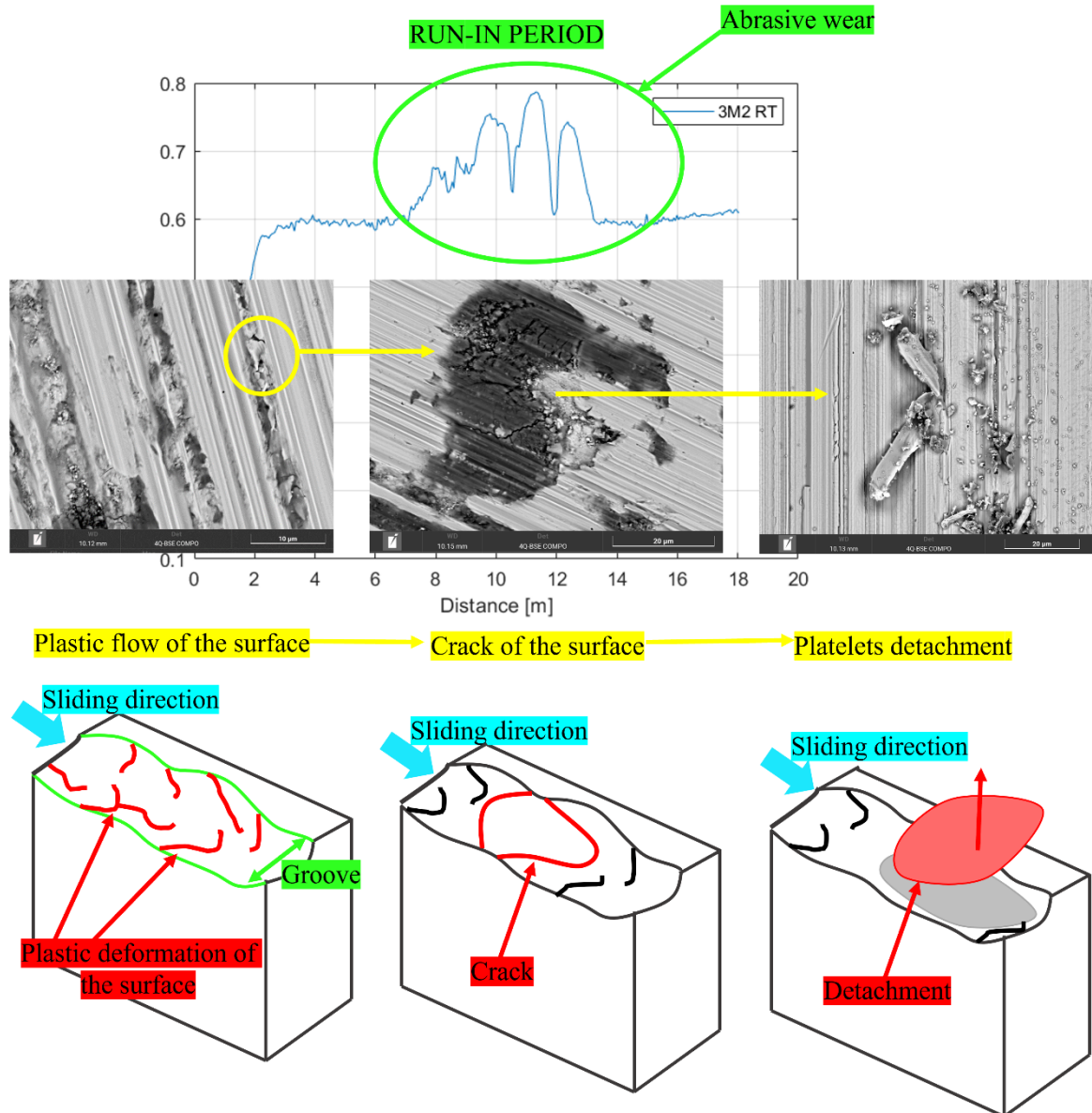


Figure 68: Sketch of the platelet formation in the run-in period.

Following the run-in period, a second stage of the wear curve emerged before the final stabilization phase. The morphology of the worn surface in this second stage was investigated after a specific interrupted wear test (RT65) test, where the CoF exhibited fluctuations and a gradual increase before stabilizing at an average value of 0,58 (Figure 45.d). However, the rise in CoF during this stage is less pronounced than during the run-in period, indicating a reduction in abrasive wear. The worn surface is smoother compared to the previous one (Figure 50.e). The fluctuation of the CoF may be attributed to the ongoing abrasive wear [98], which continues to generate detachment zones and plastically deformed surfaces on the track (Figure 49.d). If the platelets remain along the track, they will be crushed by the passage of the counter-body, leading to the accumulation zone of oxidized, powder-like debris (Figure 52.b and Figure 53.b). This debris is continually crushed and displaced throughout the wear test, resulting in a smooth final surface with minimal debris along the grooves after 1500 meters (Figure 51.d). In the final stage, called “stable periodic fluctuation” in [96], the

debris is completely oxidated (Table 11) and exhibits a red coloration (Figure 52.c). The CoF stabilizes (Figure 45.a) and the surface becomes smooth. The worn track achieved after the reference wear test (RT1500) (Figure 47.c and Table 8) revealed the greatest depth and width but the lowest wear rate. In general, the wear rate decreases with increasing distance, indicating the stabilization of the wear behaviour of the material. The wear rate for the RT1500 is more than 10 times lower than the one of RT18 (Figure 46).

The continuous passage of the counter-body impacts not only the surface but also the microstructure underneath the worn track. Two friction-induced layers are formed, a Mechanical Mixed Layer (MML, Figure 55.a) and a Plastic Deformed Layer (PDL, Figure 55.b), identified during SEM analyses. The MML has been extensively investigated in numerous studies [44, 47, 48, 50]. The thickness of the MML layer is related to the propensity for oxide formation and subsequent detachment from the surface. As illustrated in Figure 69 and previously discussed in this section, platelets detach from the track surface. These platelets can be ground during each lap, becoming powder-like debris. Then the debris can be compressed by the counter body on the track surface, forming the MML. Thus, the MML is composed of powder-like debris (red layer in Figure 69) and small platelets (green circles in Figure 69). The formation of the MML starting from powder-like debris may be facilitated by the presence of grooves [97]. The PDL, also called “sliding slipping” layer [100], is a plastic deformed zone under the track [101]. The PDL is linked to the failure of the cellular structure due to the continuous passage and shear stress of the counter body with each lap (blue structure in Figure 69). An alternative hypothesis is related to the movement of dislocations, as this is the primary mechanism for PDL formation in martensitic structures [85, 86]. In this context, dislocations tend to accumulate and migrate, thereby altering the substructure of the track. This dislocation activity is similarly driven by the passage and shear stress imposed by the counter-body on the surface.



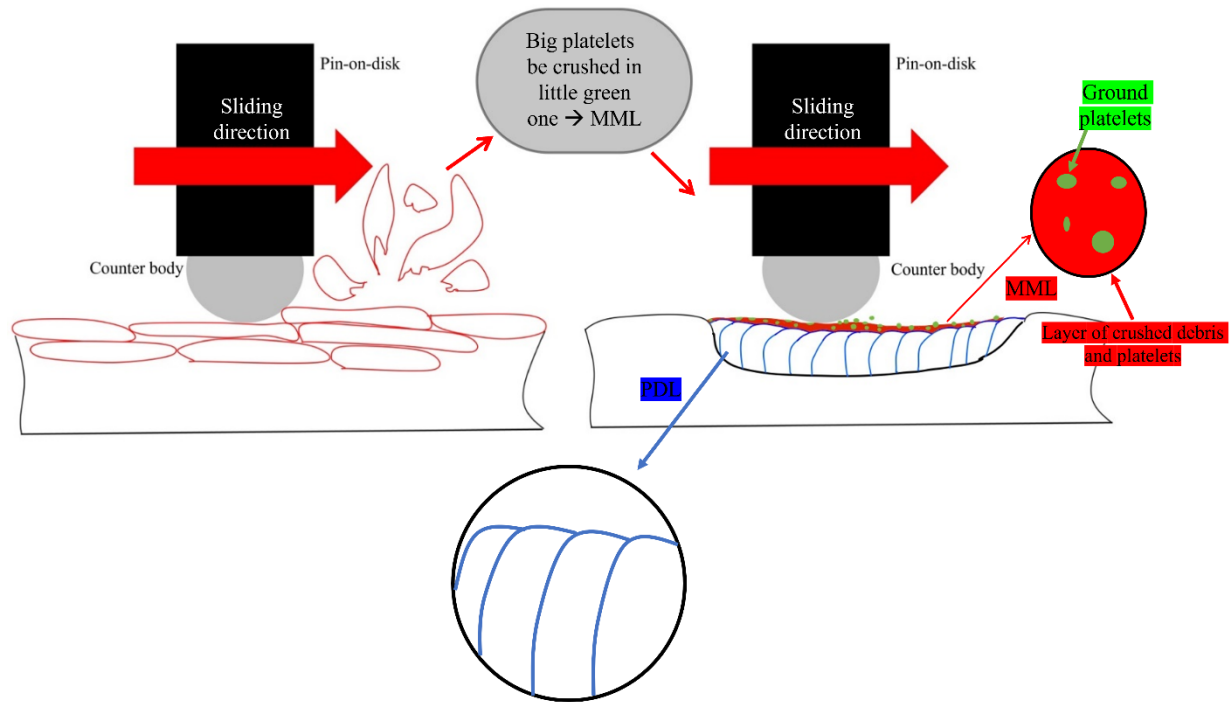


Figure 69: Sketch of MML formation. Platelets were detached, grind, and then form the MML over the PDL.

In summary (Figure 70), three main zones of interest have been investigated to elucidate the evolution of the wear mechanisms behaviour occurring with AISI S2 steel sliding against the  $\text{Al}_2\text{O}_3$  counter-body. The first zone, where abrasive wear predominates, corresponds to a run-in period. Here, the plastic flow of the track, grooves, and subsequent cracks and detachment occur. These platelets can be ground by the continuous passage of the counter body and crushed by it along the track, gradually forming the MML. Beneath the MML, a PDL also forms due to the pressure and forces exerted by the passage of the counter-body, which can lead to failure of the cellular structure or movement of dislocations, typical of the martensitic structures. In general, after the initial severe abrasive wear mechanism, the final worn surface is smooth with a total low wear rate, thus suggesting an overall good wear resistance of the material at room temperature.

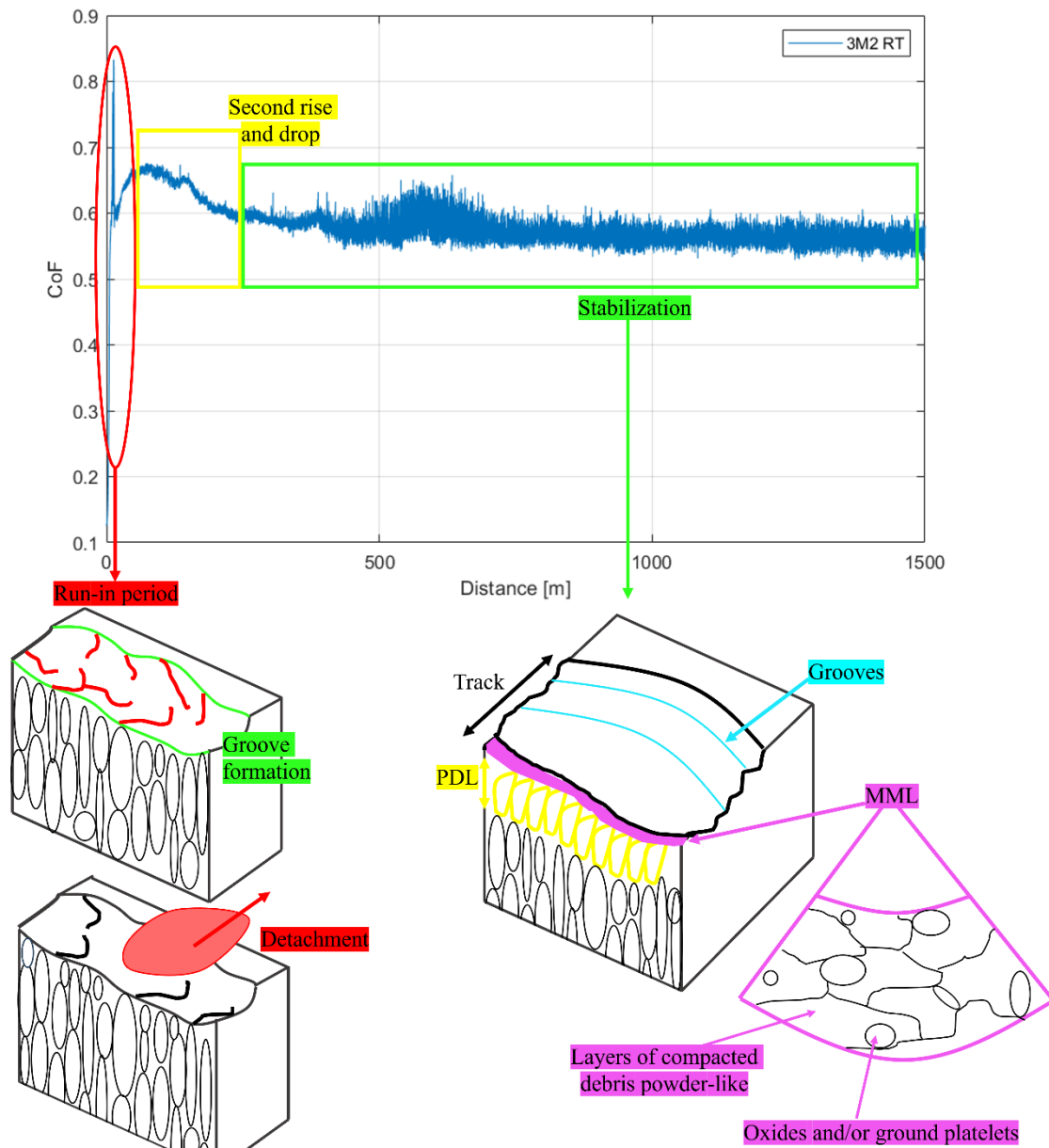


Figure 70: Sketch of the microstructure evolution during the RT test.

### 5.3 Effect of temperature on wear behaviour

After having explained the wear sequence at room temperature based on the interrupted wear tests approach, a general assessment of the wear properties at high temperatures will be given. Profilometer measurements revealed a higher worn volume of all the high-temperature tests compared to that performed at room temperature (RT1500) (Figure 47). Notably, the HT300 showed a wear rate more than 10 times higher than the RT1500 test, due to the higher depth of the worn track (Figure 58). The wear rate of HT400 decreased compared to the other HT tests (Figure 59). Profilometer analyses, OM and SEM micrographs (Figure 61 and Figure 62) of the HT200 and HT300 tests revealed a smooth and regular worn track. Only a few grooves, delaminated areas, and debris accumulated along the

grooves were observed in the HT200 and HT300 tests, similar to the RT1500 tests. In contrast, the worn track achieved after the HT400 test was irregular, with areas where higher depth and width were achieved (Figure 63). An inhomogeneous layer of oxides is present in these zones. In contrast, a homogeneous layer of oxides is present in areas where lower depth and width were achieved. This layer of oxides is the so-called tribolayer [104], which helped to prevent the track from further wear. The reasons for such differences between the different tests are linked both to oxidation phenomena and to microstructural changes occurring during the tests.

Regarding oxidation phenomena, it is important to highlight that the pin-on-disc tests can be considered as a heat treatment. Indeed, the high-temperature wear tests were extended over prolonged durations, exceeding four hours. This extended duration effectively acts as a heat treatment. In view of the exposure to air, surface oxidation occurred during the test. In particular, all the wear samples exhibited consistent tempering colours after the tests (Figure 56). This surface oxidation is responsible for the accelerated wear compared to the test room temperature, where surface oxidation did not occur. Microscope observations on the cross-section revealed the nature of the oxide formed (Figure 64 and Figure 65). A thin oxide layer was formed during the test at 200°C and 300°C, being the iron-oxide  $\alpha\text{-Fe}_2\text{O}_3$ , while the thicker oxide layer formed at 400°C (the double compared to the previous one), is associated with  $\text{Fe}_3\text{O}_4$  [105]. Among the high-temperature tests, the decrease in wear rate achieved with HT400 is associated with the formation of the thicker  $\text{Fe}_3\text{O}_4$ , also known to be more stable and protective than  $\text{Fe}_2\text{O}_3$  [62][63]. In the case of  $\alpha\text{-Fe}_2\text{O}_3$ , there is a competition between its formation and removal, which may cause less wear resistance [106]. Furthermore, the lower wear rate of the test HT400 is due to the presence of the homogeneous tribolayer of oxides, mentioned earlier. Cross-section observations revealed that such tribolayer consists of compacted debris (Figure 65). Such pieces of debris originated from delamination phenomena occurring in the original  $\text{Fe}_3\text{O}_4$  layer during the test (Figure 61.d and Figure 62.d). Moreover, unlike in the RT1500 test, the alumina counter-body shows signs of wear in the high temperature tests, especially in the HT400 (Figure 60). Thus, the debris generated actively participate in the formation of the tribolayer. Therefore, the formation of a thick oxide layer and compacted tribolayer within the surface during the HT400 test allowed to achieve lower wear rates compared to the tests HT200 and HT300. Furthermore, the effect of the presence of such protective layers allowed to achieve lower CoF during the test HT400 compared to all the other tests (Figure 57), in view of reduced friction [96].

Microstructural changes were observed within the subsurface underneath the worn track. In particular, during the test HT400, a thicker Plastic Deformation Layer (PDL) is formed compared to that of the other tests (Figure 65). This difference is linked to different microstructures. As mentioned earlier,

the high-temperature tests can be considered as a heat treatment. Table 14 lists the average hardness values of the samples after high-temperature wear tests. These hardness values are comparable (Figure 66) to those of the samples that underwent DSC heat treatment (Table 7). This comparison provides evidence that high-temperature wear tests function as a heat treatment for the samples, thus modifying the microstructure as explained in section 5.1. Therefore, the softer microstructure achieved with the test HT400 led to the formation of a thicker PDL, in view of a higher sensitivity to deformation of less hard microstructures [107].

In summary, the wear resistance of AISI S2 tool steel is better at 400°C than at 200°C and 300°C. A thick  $\text{Fe}_3\text{O}_4$  oxide layer and a tribolayer participate in the protection from wear at 400 °C. In contrast, the thin  $\alpha\text{-Fe}_2\text{O}_3$  oxide layer formed at 200 °C and 300 °C does not protect the surface. On the contrary, its formation contributes to increasing the worn volume. However, all the high temperature tests exhibited higher worn volumes than the test performed at room temperature (Figure 59).



## 6. Conclusion

In this study, several experiments have been carried out to investigate the thermal stability and wear behaviour at room and high temperatures (up to 400°C) of LPBF-printed AISI S2 tool steel. From the results, the following conclusions can be drawn:

- LPBF-printed AISI S2 demonstrates thermal stability up to 300°C, with the microstructure remaining similar to the as-built state. An increase in hardness was observed, due to the silicon effect on inhibiting carbide precipitation, thus preventing softening. At 400°C significant changes occur: the heat-affected zones (HAZs) and melt pools become indiscernible, accompanied by a decrease in hardness due to a higher sensitivity to tempering.
- At room temperature, AISI S2 shows an excellent wear behaviour up to 1500 meters of sliding distance. In the first laps, severe abrasive wear occurs with the formation of grooves and platelets detachment. At 1500 meters, all the debris was oxidized and powder-like. The subsurface of the track showed a MML and a PDL.
- At high temperatures, the wear resistance decreased compared to that at room temperature. This is attributed to oxidation of the specimens, making them more susceptible to erosion by the counter body. Particularly in the HT300 test, the wear rate was observed to be ten times higher than that at room temperature.
- The HT400 test demonstrated the best wear resistance among the high-temperature wear tests. The track of the HT400 test appeared irregular due to the presence of a protective tribolayer on its surface. This tribolayer effectively shielded the track from wear. The tribolayer of the HT400 test is formed from the debris of the thick  $\text{Fe}_3\text{O}_4$  oxide layer. In contrast, at 200°C and 300°C, an oxide  $\alpha\text{-Fe}_2\text{O}_3$  would form, being less thick and less protective than one formed at 400°C.
- Also in the HT tests, SEM analyses revealed the presence of MML (Material Transfer Layer) and PDL (Plastic Deformation Layer). Particularly in the HT400 test, the depth of the PDL was observed to be the greatest, potentially due to the softer microstructure.
- The softer microstructure achieved during the test at 400°C is due to the heat treatment effect acted by the pin-on-disc, in view of the prolonged exposure to the high temperature (more than four hours).
- The effect of such heat treatment led to the achievement of a microstructure similar to that achieved during the thermal stability investigation through DSC.



## 7. Perspectives

AISI S2 tool steel is a versatile alloy known for its exceptional toughness and high impact resistance, commonly used in the manufacturing of chisels, punches, and other hand tools subjected to heavy-duty applications. Considering those applications, further testing could be carried out: perform similar investigations to a conventional AISI S2, in order to estimate the differences between the same material obtained with LPBF; extending the temperatures for isothermal DSC analyses and correspondent high-temperature wear tests to obtain a comprehensive overview of the behaviour of the material; design a specific thermal treatment to achieve a microstructure with enhanced thermal stability and wear resistance compared to the as-built; wear tests with different counter-body could be interesting to highlight the existence of different wear mechanism; TEM analyses could be performed to understand carbide precipitation and dislocations movement that occurs during thermal treatments; evaluate the corrosion resistance and other mechanical properties (tensile and compression tests).





## 8. References

- [1] W. E. Frazier, “Metal additive manufacturing: A review,” *J. Mater. Eng. Perform.*, vol. 23, no. 6, pp. 1917–1928, 2014, doi: 10.1007/s11665-014-0958-z.
- [2] C. Cai and K. Zhou, *Metal additive manufacturing*. INC, 2022.
- [3] S. R. Narasimharaju *et al.*, “A comprehensive review on laser powder bed fusion of steels: Processing, microstructure, defects and control methods, mechanical properties, current challenges and future trends,” *J. Manuf. Process.*, vol. 75, no. January, pp. 375–414, 2022, doi: 10.1016/j.jmapro.2021.12.033.
- [4] E. Saggionetto, E. Filippi, O. Dedry, J. T. Tchuindjang, and A. Mertens, “Development and processability of AISI S2 tool steel by laser powder bed fusion,” *Mater. Res. Proc.*, vol. 28, pp. 41–48, 2023, doi: 10.21741/9781644902479-5.
- [5] E. Filippi, “Université de Liège – Università degli Studi di Padova Fabrication and characterization of low-alloyed tool steel obtained by Selective Laser Melting Elena Filippi,” 2022.
- [6] W. Abd-Elaziem *et al.*, “On the current research progress of metallic materials fabricated by laser powder bed fusion process: a review,” *J. Mater. Res. Technol.*, vol. 20, pp. 681–707, 2022, doi: 10.1016/j.jmrt.2022.07.085.
- [7] N. Guo and M. C. Leu, “Additive manufacturing: Technology, applications and research needs,” *Front. Mech. Eng.*, vol. 8, no. 3, pp. 215–243, 2013, doi: 10.1007/s11465-013-0248-8.
- [8] D. Herzog, V. Seyda, E. Wycisk, and C. Emmelmann, “Additive manufacturing of metals,” *Acta Mater.*, vol. 117, pp. 371–392, 2016, doi: 10.1016/j.actamat.2016.07.019.
- [9] I. D. Harris, “Development and implementation of metals additive manufacturing,” *Addit. Manuf. Handb. Prod. Dev. Def. Ind.*, pp. 215–224, 2017, doi: 10.1201/9781315119106.
- [10] E. Jelis, M. R. Hespos, and N. M. Ravindra, “Process Evaluation of AISI 4340 Steel Manufactured by Laser Powder Bed Fusion,” *J. Mater. Eng. Perform.*, vol. 27, no. 1, pp. 63–71, 2018, doi: 10.1007/s11665-017-2989-8.

- [11] C. Y. Yap *et al.*, “Review of selective laser melting: Materials and applications,” *Appl. Phys. Rev.*, vol. 2, no. 4, 2015, doi: 10.1063/1.4935926.
- [12] J. Schweiger, D. Edelhoff, and J. F. Güth, “3d printing in digital prosthetic dentistry: An overview of recent developments in additive manufacturing,” *J. Clin. Med.*, vol. 10, no. 9, 2021, doi: 10.3390/jcm10092010.
- [13] Y. Liu, Y. Yang, S. Mai, D. Wang, and C. Song, “Investigation into spatter behavior during selective laser melting of AISI 316L stainless steel powder,” *Mater. Des.*, vol. 87, pp. 797–806, 2015, doi: 10.1016/j.matdes.2015.08.086.
- [14] W. Hearn, P. Harlin, and E. Hryha, “Development of powder bed fusion–laser beam process for AISI 4140, 4340 and 8620 low-alloy steel,” *Powder Metall.*, vol. 66, no. 2, pp. 94–106, 2023, doi: 10.1080/00325899.2022.2134083.
- [15] B. Zhang, Y. Li, and Q. Bai, “Defect Formation Mechanisms in Selective Laser Melting: A Review,” *Chinese J. Mech. Eng. (English Ed.)*, vol. 30, no. 3, pp. 515–527, 2017, doi: 10.1007/s10033-017-0121-5.
- [16] J. Saewe, N. Carstensen, P. Kürnsteiner, E. A. Jägle, and J. H. Schleifenbaum, “Influence of increased carbon content on the processability of high-speed steel HS6-5-3-8 by laser powder bed fusion,” *Addit. Manuf.*, vol. 46, no. January, 2021, doi: 10.1016/j.addma.2021.102125.
- [17] L. E. Murr *et al.*, “Metal Fabrication by Additive Manufacturing Using Laser and Electron Beam Melting Technologies,” *J. Mater. Sci. Technol.*, vol. 28, no. 1, pp. 1–14, 2012, doi: 10.1016/S1005-0302(12)60016-4.
- [18] J. Wang, R. Zhu, Y. Liu, and L. Zhang, “Understanding melt pool characteristics in laser powder bed fusion: An overview of single- and multi-track melt pools for process optimization,” *Adv. Powder Mater.*, vol. 2, no. 4, 2023, doi: 10.1016/j.apmate.2023.100137.
- [19] S. L. Sing and W. Y. Yeong, “Laser powder bed fusion for metal additive manufacturing: perspectives on recent developments,” *Virtual Phys. Prototyp.*, vol. 15, no. 3, pp. 359–370, 2020, doi: 10.1080/17452759.2020.1779999.
- [20] X. Kang, S. Dong, H. Wang, S. Yan, X. Liu, and H. Ren, “Effect of thermal cycle on microstructure evolution and mechanical properties of selective laser melted low-alloy steel,”

*Materials (Basel)*., vol. 12, no. 21, pp. 1–15, 2019, doi: 10.3390/ma12213625.

- [21] R. Seede *et al.*, “An ultra-high strength martensitic steel fabricated using selective laser melting additive manufacturing: Densification, microstructure, and mechanical properties,” *Acta Mater.*, vol. 186, pp. 199–214, 2020, doi: 10.1016/j.actamat.2019.12.037.
- [22] E. Liverani, S. Toschi, L. Ceschini, and A. Fortunato, “Effect of selective laser melting (SLM) process parameters on microstructure and mechanical properties of 316L austenitic stainless steel,” *J. Mater. Process. Technol.*, vol. 249, no. June, pp. 255–263, 2017, doi: 10.1016/j.jmatprotec.2017.05.042.
- [23] R. Seede *et al.*, “Effect of heat treatments on the microstructure and mechanical properties of an ultra-high strength martensitic steel fabricated via laser powder bed fusion additive manufacturing,” *Addit. Manuf.*, vol. 47, no. August, p. 102255, 2021, doi: 10.1016/j.addma.2021.102255.
- [24] M. A. Ryder *et al.*, “Melt Pool and Heat Treatment Optimization for the Fabrication of High-Strength and High-Toughness Additively Manufactured 4340 Steel,” *J. Mater. Eng. Perform.*, vol. 30, no. 7, pp. 5426–5440, 2021, doi: 10.1007/s11665-021-05836-8.
- [25] T. Maurizi Enrici, A. Mertens, M. Sinnaeve, and J. T. Tchuindjang, “Elucidation of the solidification sequence of a complex graphitic HSS alloy under a combined approach of DTA and EBSD analyses,” *J. Therm. Anal. Calorim.*, vol. 141, no. 3, pp. 1075–1089, 2020, doi: 10.1007/s10973-019-09093-9.
- [26] R. Acharya, J. A. Sharon, and A. Staroselsky, “Prediction of microstructure in laser powder bed fusion process,” *Acta Mater.*, vol. 124, pp. 360–371, 2017, doi: 10.1016/j.actamat.2016.11.018.
- [27] E. Elhachmi, “Tool steels,” *Steel Heat Treat. Metall. Technol.*, pp. 651–694, 2006, doi: 10.31399/asm.tb.spsp2.t54410621.
- [28] D. D. Gu, W. Meiners, K. Wissenbach, and R. Poprawe, “Laser additive manufacturing of metallic components: Materials, processes and mechanisms,” *Int. Mater. Rev.*, vol. 57, no. 3, pp. 133–164, 2012, doi: 10.1179/1743280411Y.0000000014.
- [29] G. Huang, K. Wei, and X. Zeng, “Microstructure and mechanical properties of H13 tool steel

fabricated by high power laser powder bed fusion,” *Mater. Sci. Eng. A*, vol. 858, no. September, p. 144154, 2022, doi: 10.1016/j.msea.2022.144154.

- [30] F. S. H. B. Freeman, J. Sharp, J. Xi, and I. Todd, “Influence of solidification cell structure on the martensitic transformation in additively manufactured steels,” *Addit. Manuf.*, vol. 30, no. July, p. 100917, 2019, doi: 10.1016/j.addma.2019.100917.
- [31] J. J. S. Dilip, G. D. J. Ram, T. L. Starr, and B. Stucker, “Selective laser melting of HY100 steel: Process parameters, microstructure and mechanical properties,” *Addit. Manuf.*, vol. 13, pp. 49–60, 2017, doi: 10.1016/j.addma.2016.11.003.
- [32] F. Klocke, K. Arntz, M. Teli, K. Winands, M. Wegener, and S. Oliari, “State-of-the-art Laser Additive Manufacturing for Hot-work Tool Steels,” *Procedia CIRP*, vol. 63, pp. 58–63, 2017, doi: 10.1016/j.procir.2017.03.073.
- [33] W. Hearn, K. Lindgren, J. Persson, and E. Hryha, “In situ tempering of martensite during laser powder bed fusion of Fe-0.45C steel,” *Materialia*, vol. 23, p. 101459, 2022, doi: 10.1016/j.mtla.2022.101459.
- [34] P. Bajaj, A. Hariharan, A. Kini, P. Kürnsteiner, D. Raabe, and E. A. Jäggle, “Steels in additive manufacturing: A review of their microstructure and properties,” *Mater. Sci. Eng. A*, vol. 772, no. October 2019, 2020, doi: 10.1016/j.msea.2019.138633.
- [35] J. Krell, A. Röttger, K. Geenen, and W. Theisen, “General investigations on processing tool steel X40CrMoV5-1 with selective laser melting,” *J. Mater. Process. Technol.*, vol. 255, no. December 2017, pp. 679–688, 2018, doi: 10.1016/j.jmatprotec.2018.01.012.
- [36] M. Zanni, F. Berto, P. E. Vullum, L. Tonelli, A. Morri, and L. Ceschini, “Effect of heat treatment and defects on the tensile behavior of a hot work tool steel manufactured by laser powder bed fusion,” *Fatigue Fract. Eng. Mater. Struct.*, vol. 46, no. 7, pp. 2681–2696, 2023, doi: 10.1111/ffe.14025.
- [37] M. Rosso, D. Ugues, and M. Actis Grande, “The challenge of PM tool steels for the innovation,” *J. Achiev. Mater. Manuf. Eng.*, vol. 18, no. 1–2, pp. 175–178, 2006.
- [38] J. Heinrichs, M. Olsson, and S. Jacobson, “Influence of tool steel microstructure on initial material transfer in metal forming-In situ studies in the SEM,” *Wear*, vol. 302, no. 1–2, pp.

1249–1256, 2013, doi: 10.1016/j.wear.2013.01.114.

- [39] M. Asif, M. A. Ahad, M. F. H. Iqbal, and S. Reyaz, “Experimental investigation of thermal properties of tool steel and mild steel with heat treatment,” *Mater. Today Proc.*, vol. 45, pp. 5511–5517, 2021, doi: 10.1016/j.matpr.2021.02.272.
- [40] J. Wilzer, S. Weber, C. Escher, and W. Theisen, “On the relationship of heat treatment , microstructure , mechanical properties , and thermal conductivity of tool steels,” *9th Int. Tool. Conference*, no. September 2012, pp. 143–152, 2012.
- [41] K. Kato, *Classification of Wear Mechanisms / Modes*. .
- [42] Y. Sun *et al.*, “Thermal and mechanical properties of selective laser melted and heat treated H13 hot work tool steel,” *Mater. Des.*, vol. 224, p. 111295, 2022, doi: 10.1016/j.matdes.2022.111295.
- [43] T. Balaško, M. Vončina, J. Burja, B. Š. Batič, and J. Medved, “High-temperature oxidation behaviour of aisi h11 tool steel,” *Metals (Basel)*., vol. 11, no. 5, 2021, doi: 10.3390/met11050758.
- [44] F. Deirmina *et al.*, “General investigations on the heat treatment and thermal fatigue behavior of an experimental hot work tool steel tailored for laser powder bed fusion,” *Mater. Sci. Eng. A*, vol. 901, no. March, 2024, doi: 10.1016/j.msea.2024.146554.
- [45] S. Bergmueller *et al.*, “Crack-free in situ heat-treated high-alloy tool steel processed via laser powder bed fusion: microstructure and mechanical properties,” *Heliyon*, vol. 8, no. 8, p. e10171, 2022, doi: 10.1016/j.heliyon.2022.e10171.
- [46] K. Benarji, Y. Ravi Kumar, A. N. Jinoop, C. P. Paul, and K. S. Bindra, “Effect of Heat-Treatment on the Microstructure, Mechanical Properties and Corrosion Behaviour of SS 316 Structures Built by Laser Directed Energy Deposition Based Additive Manufacturing,” *Met. Mater. Int.*, vol. 27, no. 3, pp. 488–499, 2021, doi: 10.1007/s12540-020-00838-y.
- [47] P. Krakhmalev, I. Yadroitsava, G. Fredriksson, and I. Yadroitsev, “In situ heat treatment in selective laser melted martensitic AISI 420 stainless steels,” *Mater. Des.*, vol. 87, pp. 380–385, 2015, doi: 10.1016/j.matdes.2015.08.045.



- [48] M. Wang *et al.*, “High-Temperature Properties and Microstructural Stability of the AISI H13 Hot-Work Tool Steel Processed by Selective Laser Melting,” *Metall. Mater. Trans. B Process Metall. Mater. Process. Sci.*, vol. 50, no. 1, pp. 531–542, 2019, doi: 10.1007/s11663-018-1442-1.
- [49] H. Yin, M. Song, P. Deng, L. Li, B. C. Prorok, and X. Lou, “Thermal stability and microstructural evolution of additively manufactured 316L stainless steel by laser powder bed fusion at 500–800 °C,” *Addit. Manuf.*, vol. 41, no. September 2020, p. 101981, 2021, doi: 10.1016/j.addma.2021.101981.
- [50] J. Krell, A. Röttger, K. Geenen, and W. Theisen, “General investigations on processing tool steel X40CrMoV5-1 with selective laser melting,” *J. Mater. Process. Technol.*, vol. 255, no. December 2017, pp. 679–688, 2018, doi: 10.1016/j.jmatprotec.2018.01.012.
- [51] G. Krauss, “Tempering of Lath Martensite in Low and Medium Carbon Steels: Assessment and Challenges,” *Steel Res. Int.*, vol. 88, no. 10, pp. 1–18, 2017, doi: 10.1002/srin.201700038.
- [52] Y. W. Luo, H. J. Guo, X. L. Sun, J. Guo, and F. Wang, “Influence of Tempering Time on the Microstructure and Mechanical Properties of AISI M42 High-Speed Steel,” *Metall. Mater. Trans. A Phys. Metall. Mater. Sci.*, vol. 49, no. 12, pp. 5976–5986, 2018, doi: 10.1007/s11661-018-4924-5.
- [53] P. Niederhofer, K. Eger, P. Schwingenschlögl, and M. Merklein, “Properties of Tool Steels for Application in Hot Stamping,” *Steel Res. Int.*, vol. 91, no. 5, pp. 1–9, 2020, doi: 10.1002/srin.201900422.
- [54] F. Deirmina, N. Peghini, B. AlMangour, D. Grzesiak, and M. Pellizzari, “Heat treatment and properties of a hot work tool steel fabricated by additive manufacturing,” *Mater. Sci. Eng. A*, vol. 753, no. January, pp. 109–121, 2019, doi: 10.1016/j.msea.2019.03.027.
- [55] Gwidon W Stachowiak, *Wear - Materials, Mechanism and Practice*. wiley, 2005.
- [56] Gwidon W. Stachowiak and Andrew W. Batchelor, “Abrasive, Erosive and Cavitation Wear,” *Eng. Tribol.*, pp. 525–576, 2014, doi: 10.1016/b978-0-12-397047-3.00011-4.
- [57] G. W. S. and A. W. Batchelor, “Adhesion and Adhesive Wear,” *Eng. Tribol.*, pp. 577–596, 2014, doi: 10.1016/b978-0-12-397047-3.00012-6.

- [58] G. W. S. and A. W. Batchelor, "Corrosive and Oxidative Wear," *Eng. Tribol.*, pp. 597–620, 2014, doi: 10.1016/b978-0-12-397047-3.00013-8.
- [59] M. Vardavoulas, "The role of hard second phases in the mild oxidative wear mechanism of high-speed steel-based materials," *Wear*, vol. 173, no. 1–2, pp. 105–114, 1994, doi: 10.1016/0043-1648(94)90262-3.
- [60] M. Inigo Serrano, "STUDY OF THE WEAR BEHAVIOR OF SS316L + WC COMPOSITES: ROLE OF THE COUNTER MATERIAL," no. August. 2020.
- [61] G. W. S. and A. W. Batchelor, "Fatigue Wear," *Eng. Tribol.*, pp. 621–645, 2014, doi: 10.1016/b978-0-12-397047-3.00014-x.
- [62] M. Gągol, A. Przyjazny, and G. Boczkaj, "Wastewater treatment by means of advanced oxidation processes based on cavitation – A review," *Chem. Eng. J.*, vol. 338, pp. 599–627, 2018, doi: 10.1016/j.cej.2018.01.049.
- [63] P. J. Blau and K. G. Budinski, "Development and use of ASTM standards for wear testing," *Wear*, vol. 225–229, no. PART II, pp. 1159–1170, 1999, doi: 10.1016/S0043-1648(99)00045-9.
- [64] B. Y. Peng, X. Nie, and Y. Chen, "Effects of surface coating preparation and sliding modes on titanium oxide coated titanium alloy for aerospace applications," *Int. J. Aerosp. Eng.*, vol. 2014, 2014, doi: 10.1155/2014/640364.
- [65] T. Peev, V. Taseva, I. Mitov, B. Kunev, D. Paneva, and B. Bonev, "Some data on the dynamics of corrosion processes in water circulation cooling systems," *Monatshefte fur Chemie*, vol. 132, no. 10, pp. 1181–1188, 2001, doi: 10.1007/s007060170033.
- [66] T. Miyajima *et al.*, "Friction and wear properties of lead-free aluminum alloy bearing material with molybdenum disulfide layer by a reciprocating test," *Tribol. Int.*, vol. 59, pp. 17–22, 2013, doi: 10.1016/j.triboint.2012.07.017.
- [67] F. Alam, A. Kumar, A. K. Patel, R. K. Sharma, and K. Balani, "Processing, Characterization and Fretting Wear of Zinc Oxide and Silver Nanoparticles Reinforced Ultra High Molecular Weight Polyethylene Biopolymer Nanocomposite," *Jom*, vol. 67, no. 4, pp. 688–701, 2015, doi: 10.1007/s11837-015-1358-z.

- [68] B. Podgornik, M. Šinko, and M. Godec, “Dependence of the wear resistance of additive-manufactured maraging steel on the build direction and heat treatment,” *Addit. Manuf.*, vol. 46, no. May, 2021, doi: 10.1016/j.addma.2021.102123.
- [69] K. Kosiba *et al.*, “Achieving exceptional wear resistance in a crack-free high-carbon tool steel fabricated by laser powder bed fusion without pre-heating,” *J. Mater. Sci. Technol.*, vol. 156, pp. 1–19, 2023, doi: 10.1016/j.jmst.2023.02.012.
- [70] R. K. Upadhyay and A. Kumar, “Scratch and wear resistance of additive manufactured 316L stainless steel sample fabricated by laser powder bed fusion technique,” *Wear*, vol. 458–459, no. October 2019, p. 203437, 2020, doi: 10.1016/j.wear.2020.203437.
- [71] D. K. Maodzeka, E. O. Olakanmi, M. Mosalagae, D. Hagedorn-Hansen, and S. L. Pityana, “Hybrid optimisation studies on the microstructural properties and wear resistance of maraging steel 1.2709 parts produced by laser powder bed fusion,” *Opt. Laser Technol.*, vol. 159, no. December 2022, p. 108914, 2023, doi: 10.1016/j.optlastec.2022.108914.
- [72] “aconity-midi @ aconity3d.com.” <https://aconity3d.com/products/aconity-midi/>.
- [73] “dsc-404-f1-pegasus @ analyzing-testing.netzsch.com.” <https://analyzing-testing.netzsch.com/en/products/differential-scanning-calorimeter-dsc-differential-thermal-analyzer-dta/dsc-404-f1-pegasus>.
- [74] “BX series @ www.olympus-lifescience.com.” [https://www.olympus-lifescience.com/en/technology/museum/micro/1993\\_02/](https://www.olympus-lifescience.com/en/technology/museum/micro/1993_02/).
- [75] “Tescan Clara UHR SEM @ www.tescan.com.” <https://www.tescan.com/new-tescan-clara-ultra-high-resolution-scanning-electron-microscope-brings-simplified-user-experience-to-materials-science-and-battery-research-2/>.
- [76] T. Maurizi Enrici, D. Mario, O. Dedry, S. Castagne, A. Mertens, and J. T. Tchuindjang, “Unveiling the complex wear sequence of a directed energy deposited 316L+WC hierarchical composite against alumina,” *J. Mater. Res. Technol.*, vol. 26, pp. 621–638, 2023, doi: 10.1016/j.jmrt.2023.07.172.
- [77] “tribometer index @ smtnet.com.” [https://smtnet.com/company/index.cfm?fuseaction=product\\_catalog&company\\_id=53901](https://smtnet.com/company/index.cfm?fuseaction=product_catalog&company_id=53901).

- [78] “infinitefocus @ [www.alicon.com](http://www.alicon.com).” <https://www.alicon.com/en/products/infinitefocus>.
- [79] “macrohardness @ [www.emcotest.com](http://www.emcotest.com).” <https://www.emcotest.com/en/products-services/hardness-testing-machines/>.
- [80] “nanoindenter-ti-950-triboindenter @ [www.biomat.uliege.be](http://www.biomat.uliege.be).” [https://www.biomat.uliege.be/cms/c\\_7122420/en/nanoindenter-ti-950-triboindenter?id=c\\_7122420](https://www.biomat.uliege.be/cms/c_7122420/en/nanoindenter-ti-950-triboindenter?id=c_7122420).
- [81] “Tempering\_(metallurgy) @ [en.wikipedia.org](http://en.wikipedia.org).” [https://en.wikipedia.org/wiki/Tempering\\_%28metallurgy%29](https://en.wikipedia.org/wiki/Tempering_%28metallurgy%29).
- [82] G. H. Gowd, S. S. Vali, V. Ajay, and G. G. Mahesh, “Experimental Investigations & Effects of Cutting Variables on MRR and Tool Wear for AISI S2 Tool Steel,” *Procedia Mater. Sci.*, vol. 5, pp. 1398–1407, 2014, doi: 10.1016/j.mspro.2014.07.458.
- [83] C. V. Funch, F. B. Grumsen, A. B. da Silva Fanta, T. L. Christiansen, and M. A. J. Somers, “Thermal stability of hierarchical microstructural features in additively manufactured stainless steel,” *Heliyon*, vol. 9, no. 6, p. e16555, 2023, doi: 10.1016/j.heliyon.2023.e16555.
- [84] A. Navarro-López, J. Hidalgo, J. Sietsma, and M. J. Santofimia, “Characterization of bainitic/martensitic structures formed in isothermal treatments below the Ms temperature,” *Mater. Charact.*, vol. 128, no. March, pp. 248–256, 2017, doi: 10.1016/j.matchar.2017.04.007.
- [85] T. Voisin *et al.*, “New insights on cellular structures strengthening mechanisms and thermal stability of an austenitic stainless steel fabricated by laser powder-bed-fusion,” *Acta Mater.*, vol. 203, 2021, doi: 10.1016/j.actamat.2020.11.018.
- [86] S. Wei *et al.*, “Effect of heat treatment on the microstructure and mechanical properties of 2.4 GPa grade maraging steel fabricated by laser powder bed fusion,” *Addit. Manuf.*, vol. 59, no. PB, p. 103190, 2022, doi: 10.1016/j.addma.2022.103190.
- [87] G. KAFADAR, A. KALKANLI, A. T. ÖZDEMİR, and B. ÖGEL, “Effect of isothermal transformation treatment and tempering on the microstructure and hardness of a medium c and high si steels,” *ISIJ Int.*, vol. 61, no. 5, pp. 1679–1687, 2021, doi: 10.2355/ISIJINTERNATIONAL.ISIJINT-2020-419.

- [88] N. Zhou *et al.*, “Effect of heat treatment on the hydrogen embrittlement susceptibility of selective laser melted 18Ni-300 maraging steel,” *Mater. Sci. Eng. A*, vol. 885, no. August, p. 145622, 2023, doi: 10.1016/j.msea.2023.145622.
- [89] G. Krauss, “Heat Treated Martensitic Steels: Microstructural Systems for Advanced Manufacture,” *ISIJ Int.*, vol. 35, no. 4, pp. 349–359, 1995, doi: 10.2355/isijinternational.35.349.
- [90] T. Wen, F. Yang, J. Wang, H. Yang, J. Fu, and S. Ji, “Ultrastrong and ductile synergy of additively manufactured H13 steel by tuning cellular structure and nano-carbides through tempering treatment,” *J. Mater. Res. Technol.*, vol. 22, pp. 157–168, 2023, doi: 10.1016/j.jmrt.2022.11.105.
- [91] Y. Xiao, W. Li, H. S. Zhao, X. W. Lu, and X. J. Jin, “Investigation of carbon segregation during low temperature tempering in a medium carbon steel,” *Mater. Charact.*, vol. 117, pp. 84–90, 2016, doi: 10.1016/j.matchar.2016.04.021.
- [92] C. Zhu, X. Y. Xiong, A. Cerezo, R. Hardwicke, G. Krauss, and G. D. W. Smith, “Three-dimensional atom probe characterization of alloy element partitioning in cementite during tempering of alloy steel,” *Ultramicroscopy*, vol. 107, no. 9, pp. 808–812, 2007, doi: 10.1016/j.ultramic.2007.02.033.
- [93] B. Kim, C. Celada, D. San Martín, T. Sourmail, and P. E. J. Rivera-Díaz-Del-Castillo, “The effect of silicon on the nanoprecipitation of cementite,” *Acta Mater.*, vol. 61, no. 18, pp. 6983–6992, 2013, doi: 10.1016/j.actamat.2013.08.012.
- [94] Y. Ohmori and I. Tamura, “Epsilon carbide precipitation during tempering of plain carbon martensite,” *Metall. Trans. A*, vol. 23, no. 10, pp. 2737–2751, 1992, doi: 10.1007/BF02651753.
- [95] A. Saggionetto, Enrico; Enrici, Tommaso Maurizi; Dedry, Olivier; Boschini, Frédéric; Tchuindjang, Jerome Tchoufang; Mertens, “On the role of the hierarchical structures in the friction- induced phenomena of directed energy deposited 316L+WC sliding against different counter-bodies,” *Prep.*, 2024.
- [96] X. Liang, Z. Liu, and B. Wang, “Physic-chemical analysis for high-temperature tribology of WC-6Co against Ti–6Al–4V by pin-on-disc method,” *Tribol. Int.*, vol. 146, no. November

2019, p. 106242, 2020, doi: 10.1016/j.triboint.2020.106242.

- [97] A. Pauschitz, M. Roy, and F. Franek, “Mechanisms of sliding wear of metals and alloys at elevated temperatures,” *Tribol. Int.*, vol. 41, no. 7, pp. 584–602, 2008, doi: 10.1016/j.triboint.2007.10.003.
- [98] M. Faccoli, C. Petrogalli, and A. Ghidini, “A Pin-on-Disc Study on the Wear Behaviour of Two High-Performance Railway Wheel Steels,” *Tribol. Lett.*, vol. 65, no. 4, pp. 1–7, 2017, doi: 10.1007/s11249-017-0936-3.
- [99] N. P. Suh, “An overview of the delamination theory of wear,” *Wear*, vol. 44, no. 1, pp. 1–16, 1977, doi: 10.1016/0043-1648(77)90081-3.
- [100] Y. Yang, Y. Zhu, M. M. Khonsari, and H. Yang, “Wear anisotropy of selective laser melted 316L stainless steel,” *Wear*, vol. 428–429, no. April, pp. 376–386, 2019, doi: 10.1016/j.wear.2019.04.001.
- [101] B. Venkataraman and G. Sundararajan, “THE SLIDING WEAR BEHAVIOUR OF Al-SiC OF SUBSURFACE DEFORMATION I -,” *Acta Mater.*, vol. 44, no. 2, 1996.
- [102] S. Y. Tarasov and A. V. Kolubaev, “Effect of friction on subsurface layer microstructure in austenitic and martensitic steels,” *Wear*, vol. 231, no. 2, pp. 228–234, 1999, doi: 10.1016/S0043-1648(99)00107-6.
- [103] J. Li *et al.*, “Tribological behavior of TiC particles reinforced 316Lss composite fabricated using selective laser melting,” *Materials (Basel)*, vol. 12, no. 6, 2019, doi: 10.3390/ma12060950.
- [104] H. Li, M. Ramezani, M. Li, C. Ma, and J. Wang, “Tribological performance of selective laser melted 316L stainless steel,” *Tribol. Int.*, vol. 128, no. July, pp. 121–129, 2018, doi: 10.1016/j.triboint.2018.07.021.
- [105] J. L. Sullivan and S. S. Athwal, “Mild wear of a low alloy steel at temperatures up to 500°C,” *Tribol. Int.*, vol. 16, no. 3, pp. 123–131, 1983, doi: 10.1016/0301-679X(83)90053-1.
- [106] M. M. De Oliveira, H. L. Costa, W. M. Silva, and J. D. B. De Mello, “Effect of iron oxide debris on the reciprocating sliding wear of tool steels,” *Wear*, vol. 426–427, no. December

2018, pp. 1065–1075, 2019, doi: 10.1016/j.wear.2018.12.047.

- [107] A. Lanzutti *et al.*, “High temperature study of the evolution of the tribolayer in additively manufactured AISI 316L steel,” *Addit. Manuf.*, vol. 34, no. March, p. 101258, 2020, doi: 10.1016/j.addma.2020.101258.



## 9. Annex



**SANDVIK OSPREY LTD.,**

RED JACKET WORKS,  
MILLAND ROAD,  
NEATH SA11 1NJ,  
UNITED KINGDOM

Telephone: 01639.634121  
Fax: 01639.630100  
E-Mail: powders.osprey@sandvik.com

S2 (X S2M)



### CERTIFICATE OF ANALYSIS: 32344

Revision: 1

Customer:	LIEGE UNIVERSITE
Customer Order:	ULG20/1935072/R
Customer Alloy Name:	S2
Osprey Order Number:	201127/02 CALL:01
Osprey Alloy Name:	S2
Dispatch Number:	21D0265
Weight:	50.10Kg (110lb)
Powder Size:	-45micron +10micron
Atomise Gas:	Nitrogen

Physical Test Data				Particle Size Data				Chemical Analysis(wt %)			
	Minimum	Actual	Maximum	Sieve Analysis				El	Minimum	Actual	Maximum
Tap Density, g/cc		5.00		+45µm	1.80%			Si	0.9	1.2 %	1.2
Hall Flow, s/50g		18.0	25.0	-45µm +10µm	98.20%			Mn	0.3	0.6 %	0.5
				-10µm	0.00%			Mo	0.3	0.6 %	0.6
								C	0.40	0.49 %	0.55
				Laser Diffraction Analysis				Ni	0.0	0.0	0.3
				Malvern 2000 Instrument				V	0.0	0.0	0.5
								Fe	BALANCE		
				d10 µm	20.6						
				d50 µm	31.0						
				d90 µm	47.5						
				-10.0 µm =	%						